DESIGN OF A SPACE RADIATION MONITOR FOR A SPACECRAFT IN LEO AND RESULTS FROM A PROTOTYPE ON THE FIRST TURKISH SOUNDING ROCKET

A THESIS SUBMITTED TO
THE GRADUATE SCHOOL OF NATURAL AND APPLIED SCIENCES
OF
MIDDLE EAST TECHNICAL UNIVERSITY

BY

ABDULRAHMAN ALBARODI

IN PARTIAL FULFILLMENT OF THE REQUIREMENTS
FOR
THE DEGREE OF MASTER OF SCIENCE
IN
PHYSICS

FEBRUARY 2021

Approval of the thesis:

DESIGN OF A SPACE RADIATION MONITOR FOR A SPACECRAFT IN LEO AND RESULTS FROM A PROTOTYPE ON THE FIRST TURKISH SOUNDING ROCKET

submitted by **ABDULRAHMAN ALBARODI** in partial fulfillment of the requirements for the degree of **Master of Science** i**n Physics, Middle East Technical University** by,

Prof. Dr. Halil Kalıpçılar
Dean, Graduate School of **Natural and Applied Sciences** _____

Prof. Dr. Altuğ Özpineci
Head of the Department, **Physics, METU** _____

Prof. Dr. M. Bilge Demirköz
Supervisor, **Physics, METU** _____

Examining Committee Members:

Prof. Dr. Mehmet Tevfik Zeyrek
Head of the Committee, Physics, METU _____

Prof. Dr. M. Bilge Demirköz
Supervisor, Physics, METU _____

Prof. Dr. Ahmet Oral
Physics, METU _____

Prof. Dr. Feza Arıkan
Electrical and Electronics Engineering,
Hacettepe University _____

Assoc. Prof. Emre Yüce
Physics, METU _____

Date: 03.02.2021

I hereby declare that all information in this document has been obtained and presented in accordance with academic rules and ethical conduct. I also declare that, as required by these rules and conduct, I have fully cited and referenced all material and results that are not original to this work.

Name Surname : Abdulrahman Albarodi

Signature:

ABSTRACT

DESIGN OF A SPACE RADIATION MONITOR FOR A SPACECRAFT IN LEO AND RESULTS FROM A PROTOTYPE ON THE FIRST TURKISH SOUNDING ROCKET

Albarodi, Abdulrahman
M.S. Physics
Supervisor: Prof. Dr. M. Bilge Demirköz
February 2021, 136 pages

Radiation damage to spacecraft is a major reason for malfunctions in electronic components. Monitoring real-time radiation that the spacecraft is exposed to is of utmost importance for subsequent investigation of faults and their correlation to radiation doses. Components which have completed mission lifetime successfully in space and therefore have gained heritage can be certified to a certain level of radiation tolerance for future missions. The design and optimization of a space radiation monitor was carried out as part of the IMECE project. The monitor consists of a proton radiation detector with heavy ion measurement capabilities, in a kinetic energy range of 2 MeV to 200 MeV, in addition to an electron radiation monitor with a kinetic energy range from 100 keV to 7 MeV. Both are optimized to record hits in 8 energy bins and the electron one to record fluxes higher than those of protons by a factor of 10^3 for LEO flights. Utilization of degraders and silicon detectors in sandwich form is essential for the working principal of the designed proton detector. Suitable readout electronics for these fluxes and flight qualification tests were chosen. This multipurpose radiation monitor will be manufactured and tested at the METU-DBL facility upon its completion. A prototype for this radiation monitor was produced and flown to an altitude of 136 km twice on top the SR0.1 rocket launched by ROKETSAN on the 26th -29th of October 2020. Dose rates were measured at the Pfotzer-Regener maximum as well as all through the flight path and are presented in this thesis.

Keywords: LEO Radiation Environment, Proton/Heavy-Ion Telescope, Electron Telescope, Sounding Rocket.

ÖZ

Albarodi, Abdulrahman
Tez Yöneticisi: Prof. Dr. M. Bilge Demirköz

Şubat 2021, 136 sayfa

Uydularda karşılaşılan arızaların ana sebebi, aracın bileşenlerinin radyasyona maruz kalmasıdır. Uzay aracının maruz kaldığı radyasyon miktarı üzerine veri toplamak, gelecekte radyasyon kaynaklı hasar ile maruz kalınan radyasyon dozu arasında bir korelasyon kurabilmek için çok büyük önem taşımaktadır. Uzayda görevini tamamlamış ve tarihçelenmiş bileşenlerin belli bir doza kadar dayanımı doğrulanabilir. Bu çalışmada, İMECE projesi kapsamında bir uzay radyasyon monitörünün tasarımı ve optimizasyonu gerçekleştirilmiştir. Monitör, 100 keV ve 7 MeV kinetik enerji aralığında ölçüm yapabilen bir elektron radyasyon dedektörünün yanında, 2 MeV ve 200 MeV kinetik enerji aralığında Ağır İyon ölçüm kapasitesine sahip bir Proton radyasyon dedektöründen oluşmaktadır. İki dedektör de 8 enerji sepetli algoritma kullanarak veri kaydı yapmaları için optimize edilmiştir. Elektron Dedektörü, LEO uçuşları için proton akısının 10^3 katını ölçebilir. Kalkanlar ve silikon detektörlerinin sandviç formunda kullanılması, tasarlanan proton dedektörünün çalışma prensibi için esastır. Akı koşulları ve çevre testler için uygun okuma elektronikleri seçilmiştir. Bu çok amaçlı radyasyon monitörünün tasarımı tamamlandıktan sonra üretilecek ve ODTÜ-SDH tesisinde test edilecektir. Bu radyasyon monitörü için bir protip üretilmiştir ve 26-29 Ekim 2020 tarihlerinde ROKETSAN tarafından fırlatılan SR0.1 roketinin üzerinde 136 km yüksekliğe kadar iki kere uçmuştur. Uçuş yolu boyunca ve Pfotzer-Regener maksimumunda doz hızı ölçülmüştür ve bu tezde sunulmaktadır.

Anahtar Kelimeler: LEO`da Radyasyon Ortamı, Proton/Ağır-İon Teleskobu, Elektron Teleskobu, Sonda Roketi.

CUNCTA STRICTE DISCUSSRUS !

ACKNOWLEDGMENTS

First and foremost, I would like to express my sincere gratitude and appreciation to my advisor Prof. Dr. M. Bilge Demirköz for the continuous support of my master's study and research, for her patience, motivation, enthusiasm and immense knowledge. Her guidance helped me in all the time of research and writing of this thesis. I could not have imagined having a better advisor and mentor for my master's study. Besides my advisor, I would like to thank the rest of my thesis committee: Prof. Dr. Ahmet Oral, Prof. Dr. Feza Arıkan, Prof. Dr. Mehmet Tevfik Zeyrek and Assoc. Prof. Emre Yüce for their agreement to participate in this thesis's defense.

My sincere thanks also go to Dr. Aziz Ulvi Çalışkan and the rest of TÜBITAK BİLGEM UEKAE YİTAL for their continuous help and support. Also, I am thankful to Dr. Sartuk Karasoy, Dr. Mehmet Ali Ak. Mr. Muhittin Aktaş, Mr. Tuva Cihangir Atasever and the rest of the SR0.1 rocket team from ROKETSAN and to Dr. Yüksel Subaşı and his team from GCLab. In addition, I would like to thank the Presidency of Defense Industries and the Presidency of Strategy and Budget for support as well as TENMAK PHT and CERN for their collaboration. Furthermore, big thanks to General Directorate of Mapping for providing essential RINEX data for this study and to IONOLAB for their high-quality TEC analysis.

I thank my fellow labmates in METU-IVMER: Uğur Kılıç, Ahmet Baran Can, Deniz Orhun Boztemur, Cem Zorlu, Arda Kayaalp, Pelin Uslu Kiçeci, Egecan Karadöller, Raheem Hashmani, Cenk Tüysüz, Selen Akçelik and Erinç Kılıç. Without this wonderful team, this thesis would never have been possible.

I am grateful to my family for their continued support. And I am grateful to my friends who stayed by my side at all times. I would also extend my gratitude to Prof. Davut Kavranoğlu for his immense support.

TABLE OF CONTENTS

ABSTRACT v

ÖZ vi

ACKNOWLEDGMENTS viii

TABLE OF CONTENTS ix

LIST OF TABLES xii

LIST OF FIGURES xiv

LIST OF ABBREVIATIONS xx

LIST OF SYMBOLS xxi

CHAPTERS

1 INTRODUCTION 1

1.1 Space Radiation Environment 2

1.1.1 Trapped Radiation 3

1.1.2 Solar Particle Events (SPE) 7

1.1.3 Galactic Cosmic Rays (GCR) 8

1.1.4 Cosmic Ray Showers in the Atmosphere 10

1.2 Radiation Detectors in Space 16

1.2.1 The Van Allen Probes 16

1.2.2 SEMS and RAD 18

1.2.3 EPT 18

1.2.4 MuREM/RM 19

1.2.5 SATRAM 19

1.2.6 MFS & BERM 20
1.2.7 Common Features 21
1.3 Interactions of Charged Particles with Materials 23
1.4 Radiation Damage to Spacecraft Components 27
1.4.1 Total Ionizing Dose (TID) 29
1.4.2 Single Event Effects 29
1.4.3 Displacement Damage 30
1.5 Geant4 Simulations 32
1.5.1 Geofactor Calculations 32
1.5.2 Simulation Physics 35
1.5.3 Implementing CAD Geometries into GEANT4 38
1.5.4 Geant4 Incident Spectrum 40
2 YRM PROTON TELESCOPE DESIGN 43
2.1 General Description of YRM 43
2.2 Proton Telescope Working Principle 44
2.3 Proton Telescope Design Procedure 45
2.3.1 Initial Design 45
2.3.2 Threshold Calculations 50
2.3.3 Shielding and Collimation 53
2.3.4 Design Alternatives 54
2.3.5 Telescope Acceptance Calculations 56
2.3.6 Background Rejection 60
2.3.7 Bin-to-Bin Migration and Spectrum Reconstruction 62
2.3.8 Effect of Incidence Angles 65

2.3.9 Simulation Results 68
3 YRM Readout Electronics and Detector Characterization with Data From Space Flight 83
3.1 I-V Characteristics 83
3.2 Temperature Dependence of the Leakage Current 86
3.3 C-V Characteristics 90
3.4 Prototype Radiation Monitor (SB) and Readout Electronics 92
3.5 Calibration of the Prototype Radiation Monitor (SB) 97
3.6 FPGA Logic for SB 101
3.7 Detector Testing in METU-DBL Facility 110
3.8 SB Flight and Data Analysis 112
3.9 Future Work 122
4 CONCLUSION 123
5 REFERENCES 124

LIST OF TABLES

Table 1.1 Typical altitudes of Earth orbits and doses received by satellite components behind 2.5 mm aluminum shielding [1]. 2
Table 1.2 Orbital parameters describing a typical circular heliosynchronous orbit for an Earth observation satellite [10]. 5
Table 1.3 Summary of properties of different categories of the space radiation environment al LEO. 10
Table 1.4 Instruments abroad the van Allen probes and their functions [26]. 17
Table 1.5 Comparison between MFS and BERM design parameters [32]. 21
Table 1.6 Sample dE/dx values for protons and electrons [31]. 27
Table 1.7 Types of Single Event Effects caused by radiation that might occur during mission time. 30

Table 2.1 Design Parameters of the YRM proton and electron telescopes. 44
Table 2.2 Layers of the proton telescope's initial design and their thicknesses and diameters. 46
Table 2.3 Possible outcomes of the recording algorithm in different scenarios. 50
Table 2.4 The high energy thresholds for the proton telescope. 52
Table 2.5 The Design Parameters of the Different Proton Telescope Geometries. 56
Table 2.6 Summary of simulation results of the single sized design. 75
Table 2.7 Summary of simulation results of the conical geometry design. 80
Table 2.8 Comparison between the design alternatives and their performance in the simulations at LEO environment 81
Table 2.9 Comparison between the radiation environments in LEO and GEO 81
Table 2.10 Comparison between the design alternatives and their performance in the simulations at GEO environment. 82

Table 3.1 A and B Fit Parameters from Equation (3.3) Calculated for TDA for Different Temperatures 88

Table 3.2 Activation Energies for different Reverse Bias Voltages as Calculated by Fitting of the Data in Figure 3.4 to Equation (3.4). 89
Table 3.3 Energy depositions of common cosmic ray MIPs in the detector from Geant4 and the calculated corresponding equivalent pulse height 100
Table 3.4 Data format of the packet sent by SB. 106
Table 3.5 Geiger counter count rates for using different sources and different SB modules. 109
Table 3.6 DDA3 LT and HT count rates for using different sources and different modules. 109
Table 3.7 Summary and comparison of the energy deposition values obtained via Geant4 and the measured signal width in METU-DBL..... 111
Table 3.9 Summary of flight data for first and second flights 118

LIST OF FIGURES

Figure 1.1 The Van Allen belts' location around the Earth in terms of Earth radii unit distances. [7]....4
Figure 1.2 Differential trapped protons (A) and electrons (B) spectra at LEO obtained from a SPENVIS simulation using AP8 and AE8 models respectively....6
Figure 1.3 The distribution of the proton flux seen by IMECE in 20 orbits projected onto the Earth in orbital coordinates from a SPENVIS simulation....6
Figure 1.4 Differential solar proton, He ions, C ions and O ions peak flux for a satellite in LEO....8
Figure 1.5 Heavy-Ion fluxes at 1 MeV extracted from the CREME96 database [16]. 9
Figure 1.6 Illustration of the cosmic ray shower components....11
Figure 1.7 Calculated flux of different particles at different altitude using CARI7-A software with the ISO-2004 model for altitudes above (N'42, E'35). 12
Figure 1.8 The count rate vs. altitude in the atmosphere. at the northern polar latitudes....13
Figure 1.9 Cosmic particle count-rate data obtained from sounding rocket flight using a NE-110 plastic scintillator detector [23].. 14
Figure 1.10 Variations of the absorbed dose rate, flux and specific dose for an altitude range from 0.1 to 250,000 km [18]....15
Figure 1.11 View of the cross section of EPT spectrometer [29]. 19
Figure 1.12 Photograph of the SATRAM unit placement onboard the Proba-V satellite....20
Figure 1.13 Exploded view of BERM internals, Silicon detectors [32]....21
Figure 1.14 General schematic of the working principle of the silicon PIN diode for charged particle detection....22
Figure 1.15 Bragg peaks normalized to relative dose, drawn for protons, alpha particles, carbon ions, oxygen ions [38]....25

Figure 1.16 The differential energy loss as a function of βγ showing the minimum energy transfer point for different particles [39]. 26
Figure 1.17 Illustration of damage caused to crystal structure after a displacement damage event. 31
Figure 1.18 Placement of a typical telescope in a Monte-Carlo simulation to calculate the Geofactor. 34
Figure 1.19 Physics models that can be used by Geant4 simulations and their validity energy region [51]. 36
Figure 1.20 Energy deopsiton in sample silicon detector at different cutoff values in Geant4 (A). The used sample detector setup in the simulation (B) [51]. 37
Figure 1.21 Energy deposition disribution in silicon detectors as a function of proton kinetic energy using edited physics and using default physics. 38
Figure 1.22 User interface of the program to import CAD files into Geant4. 40
Figure 1.23 Primary proton spectrum generated by the Geant4 simulation using pointwise definition and exponential interpolation 41
Figure 1.24 Primary proton spectrum generated by the Geant4 simulation using histogram definition. 42

Figure 2.1 Proton telescope's initial geometry shown inside a Geant4 simulation. 46
Figure 2.2 Energy deposition of protons in the silicon layers of the proton telescope as a function of primary kinetic energy 47
Figure 2.3 Energy deposition of O^{+8}, He^{+2} ions and protons inside the first and second silicon layer. 48
Figure 2.4 Energy deposition distribution of protons in consecutive silicon detectors. 51
Figure 2.5 Energy deposition distribution of particles in pairs of consecutive detectors. 52
Figure 2.6 The general design and working principle of the proton telescope. Arrows represent incoming protons. 53

Figure 2.7 Ideal acceptance curve of the proton telescope for protons in a Geant4 simulation. 57
Figure 2.8 Undesired acceptance of the proton telescope hits from the side penetrating hits in a Geant4 simulation. 58
Figure 2.9 The Acceptance curve of the conical design of the proton telescope in a Geant4 simulation. 59
Figure 2.10 The Acceptance curve of the single sized design of the proton telescope in a Geant4 simulation. 59
Figure 2.11 Acceptance curve of the proton telescope heavy-ion channels to alpha particle irradiation in Geant4 simulation. 60
Figure 2.12 Acceptance of the proton telescope to primary electron radiation in Geant4 simulation. 61
Figure 2.13 Helium background contribuition to the proton telescope acceptance for proton channels in Geant4 simulations. 62
Figure 2.14 Acceptance curve of the proton telescope single sized design, divided into 8 energy regions for calculation of reconstruction algorithm parameters. 63
Figure 2.15 Normal operation scenario for a high incidence angle particle incoming at the proton telescope. 65
Figure 2.16 The first scenario by which particles with high incidence angles can cause faulty measurements 66
Figure 2.17 The first scenario by which particles with high incidence angles can cause faulty measurements 67
Figure 2.18 Scenario by which misidentification in Heavy-Ion channels occur. 67
Figure 2.19 Primary protons energy spectrum in Geant4, normalized SPENVIS trapped proton energy spectrum 69
Figure 2.20 The resulting counts in the energy bins of the proton telescope single sized design compared with the primary particle counts in the Geant4 simulation. 70
Figure 2.21 The sensitivity of proton telescope energy bins compared to the incident primary proton energy spectrum in Geant4 simulation. 71

Figure 2.22 The sensitivity of the energy channels to primary solar protons and the counts in the telescope energy channels compared to the primary solar proton spectrum. 72
Figure 2.23 The sensitivity of detector proton channels (left) and Heavy Ion channels (right) against GCR alpha particles. 73
Figure 2.24 The sensitivity of detector proton channels (left) and Heavy Ion channels (right) against GCR protons. 74
Figure 2.25 The measured and normalized counts of the proton telescope inside the Geant4 simulation compared to the incident primary proton energy spectrum. 76
Figure 2.26 The sensitivity of proton telescope energy bins compared to the incident primary proton energy spectrum in Geant4 simulation. 77
Figure 2.27 The sensitivity of proton telescope energy bins compared to the incident primary solar proton energy spectrum in Geant4 simulation. 78
Figure 2.28 The sensitivity of proton telescopes proton channels and heavy ion channels against GCR alphas. 79
Figure 2.29 The sensitivity of proton telescopes proton channels and heavy ion channels against GCR protons. 80

Figure 3.1 The I-V Characteristics of DDA3 Detector Quadrants. 84
Figure 3.2 I-V Characteristics of a TDA Detector. 85
Figure 3.3 The dependence of the I-V characteristics of the TDA detector on temperature. Solid lines correspond to the fit functions. 87
Figure 3.4 Linear fits to the logarithm of leakage current against 1/kT for activation energy calculation of the TDA detector. 89
Figure 3.5 C-V and $1/C^2$-V plots for a single quadrant in a DDA3 detector and C-V and $1/C^2$-V plots for the TDA detector. 91
Figure 3.6 The doping concentration in the DDA3 and TDA detectors obtained as a function of the depletion width. 92

Figure 3.7 The CAD design of the prototype Radiation Monitor “SB” and a picture of the flight module with a pencil for scale. 93
Figure 3.8 Circuit diagram for the prototype Radiation Monitor, version 1. 94
Figure 3.9 Pulse height histogram showing the preamplifier (U2) output in response to alpha hits from an Am-241 source. Blue curve is under the orange one. 95
Figure 3.10 Final version (v11) of the circuit for the prototype radiation monitor for a single quadrant of the DDA3 detector. 96
Figure 3.11 Comparison of the pulse generated by an alpha particle from an Am241 source for 0.2pF, 0.1pF and no capacitance for the feedback on the U1 op-amp. .. 97
Figure 3.12 Measured Pulse Height of Am-241 alpha particles with different distances between the source and the detector. 98
Figure 3.13 The similar behavior of Geant4 simulation results of alpha energy deposited in the detector and Am-241 alpha pulse heights 99
Figure 3.14 Threshold scan performed using Am-241 source at distance 1.7±0.1 cm from the detector. 101
Figure 3.15 Comparison between low energy or noise hitand a high energy or stopping particle signal shapes at the comparator output (U3). 102
Figure 3.16 Particle signal in the showing ringing in the output of the comparator (U3) as recorded by a Lecroy WaveRunner8254 oscilloscope. 103
Figure 3.17 A snippet from the data dump generated by the FPGA for the readout by the DDA3 tested with alphas from an Am241 source. 103
Figure 3.18 Cycle threshold scan of signal width for the FPGA algorithm for different deadtimes. 104
Figure 3.19 Comparison of count rates for HT and LT channels versus distance using an Am-241 alpha source. 105
Figure 3.20 An example 64-byte long data packet from SB 107
Figure 3.21 Test run of the YRM prototype in the IVMER lab showing data acquisition for 2 hours. 108
Figure 3.22 Histogram of signal width for the top DDA3 detector irradiated with 15 and 30 MeV protons at METU-DBL. 111

Figure 3.24 Background radiation monitoring using the bottom DDA3 from SB.002 box, during a 30MeV irradiation test in METU-DBL. 112
Figure 3.25 Picture of the SR 0.1 rocket vertical on the launch pad in Sinop [80]. 113
Figure 3.26 Picture of the fairing separation of the SR 0.1 rocket during flight [81]. 114
Figure 3.27 Data Collected from the first flight of SB.003 on the 26th during ascent. 115
Figure 3.28 Data Collected from the first flight of SB.003 on the 26th during descent. 116
Figure 3.29 Geiger Counter measurement during the ascent and descent of the SR0.1 flight on the 29th of October. 117
Figure 3.30 DDA3 measurement during the SR 0.1 flight on the 29th of October. 118
Figure 3.31 IONOLAB-TEC data provided by IONOLAB using the RINEX data provided by General Directorate of Mapping [83]. 119
Figure 3.32 Picture from SOHO white light chronographs C2 (1.5 to 6 solar radii, Left) and C3 (3.7 to 30 solar radii, Right) [82]. 121
Figure 3.33 10.7cm radiometry data on the dates of the flights showing the CME on the 28th of October plotted with data obtained from [92]. 121
Figure 3.34 Neutron monitor data during the dates of the flight plotted using data from the Oulu neutron monitor [93]. 122

LIST OF ABBREVIATIONS

ABBREVIATIONS

YRM	: Yerli Radyasyon Monitörü, Homegrown Radiation Monitor
LEO	: Low Earth Orbit
GEO	: Geostationary Earth Orbit
MEO	: Middle Earth Orbit
ISS	: International Space Station
GEANT4	: Geometry and Tracking 4
SPENVIS	: Space Environment Information System
ESA	: European Space Agency
FPGA	: Field Programmable Gate Array
IVME-R	: The Research and Application Center for Space and Accelerator Technologies
SPE	: Solar Particle Event
GCR	: Galactic Cosmic Rays
CME	: Coronal Mass Ejection
TID	: Total Ionizing Dose
CAD	: Computer Aided Design
METU-DBL	: METU Defocusing Beamline
SB	: YRM Prototype

LIST OF SYMBOLS

SYMBOLS

q	: Charge of Electron
C	: Capacitance
V	: Voltage
V_R	: Reverse Bias Voltage
I	: Current
k	: Boltzmann's Constant
T	: Temperature
N_A	: Doping Concentration
N_a	: Avogadro's Number
$\frac{dE}{dx}$	: Energy Loss by Particle per unit distance traversed
m_e	: Mass of the Electron
r_e	: Radius of the Electron
ρ	: Density
c	: Speed of Light in Vacuum
Z	: Atomic Number
z	: Charge
A	: Area

CHAPTER 1

INTRODUCTION

Radiation in space is a major cause for spacecraft malfunctions and crew health risks. Many models have been developed to predict the space radiation environment at different orbits and many detectors have been designed and flown to measure and improve these models. Design and optimization of such a detector is a task best performed by Monte-Carlo particle physics simulations. Understanding the physical interactions of the most prominent particles in orbit is of utmost importance to perform these simulations as well as the geometrical acceptance and detector efficiency of the setup.

The damage mechanisms caused by radiation to electronic components in spaceraft depend on the particle type and energy as well as its interaction with target materials. Thus, a radiation monitor in orbit must be sensitive to these particles and energies that cause the most damage. Geant4 software package is a great tool for simulating the behaviour of such a detector. Optimizing this software package by creating auxilary tools and adjusting the internal physics modeling is crucial in designing an efficient radiation monitor for Earth orbit.

This chapter will detail the different models used to predict the radiation environment in Earth orbits and different measurement devices deployed in space throughout the years. Then it will discuss the interactions of particles in materials and the Geant4 software package as well as the contributions made to it.

1.1 Space Radiation Environment

Understanding the space radiation environment in Earth orbit is fundamental to the safety of crew members and the reliability of spacecraft's components. Orbits of Earth are often classified into three categories: low Earth orbit (LEO), medium Earth orbit (MEO) and geostationary Earth orbit (GEO). Different orbit altitudes and inclinations result in different doses received by the spacecraft as well as the energy spectra and particles it is exposed to. Typical orbits, altitudes and corresponding absorbed radiation doses are classified in Table 1.1 [1].

Table 1.1 Typical altitudes of Earth orbits and doses received by satellite components behind 2.5 mm aluminum shielding [1].

Orbit Type	**Altitude Ranges**	**Dose (order of magnitude)**
Low Earth Orbit (LEO)	160 km - 2000 km	0.1 krad/year
Medium Earth Orbit (MEO)	2000 km - 35786 km	100 krad/year
Geostationary Earth Orbit (GEO)	About 35786 km	10 krad/year

The energy spectrum ranges and the further details on the space environment in LEO is investigated in the sections [1.1.1-1.1.3]. Earth observation satellites like IMECE and Göktürk are often positioned in LEO with high inclinations in heliosynchronous orbits. This has the added benefit of being able to observe different parts of the Earth in the course of several orbits [2]. However, satellites in such orbits spend a significant amount of their flight path in the polar region, thus exposing it to high amounts of radiation in each orbit pass.

Charged space radiation in Earth orbit consists of protons, electrons and heavy ions and are often classified into three categories including Galactic Cosmic rays (GCR), trapped radiation such as the Van Allen Belts and Solar Particle Events (SPE) [3, 4, 5]. In LEO, the Earth's magnetic field's deflection of incoming particles based on

their momentum and direction results in a cutoff in the particle spectrum coming from space. This limit on a particle momentum based on its direction is known as the geomagnetic cutoff, as is given by the Störmer approximation in terms of rigidity as shown below [6]:

$$R_C = \frac{Mcos^4\lambda}{r^2\left(1 \pm \sqrt{1 - sin\epsilon \cdot sin\xi \cdot cos^3\lambda}\right)^2} \tag{1.1}$$

where M is the magnitude of the dipole moment, λ is the latitude from the magnetic equator, ϵ is the zenith angle of the incoming particle, ξ is the azimuthal angle to the North magnetic pole and r is the distance from the dipole center. Low energy particles are usually deflected, except for near the poles, where the magnetic field lines converge and point towards the surface of the Earth thus collinear incoming particles can enter through the geomagnetic environment. The magnetic field of the Earth also traps a lot of these particles creating the Van Allen belts [7]. Cosmic galactic particles that have high enough energies (beyond the geomagnetic cutoff) can make it to LEO and can also cause particle showers in the upper atmosphere [8]. These radiation modes will be investigated further in the following sections.

1.1.1 Trapped Radiation

Discovered as early as 1958 [9], the van Allen belts are among the most surveyed modes of radiation in LEO. Charged particles originating elsewhere in space get trapped and mirrored in the magnetic field of the Earth. The particles move back and forth between mirror points in the Northern and Southern Hemispheres while revolving around the Earth's field lines in cyclotron motion as well as drifting East or West depending to their charge [10]. It consists of two main belts of radiation that surround the Earth emerging from pole to pole as shown in Figure 1.1. The inner belt is dominated by protons due to their larger mass and thus smaller synchrotron radius. The outer belt is dominated by trapped electrons. Positively charged particles drift West and negatively charged particles drift East. The fluxes of these belts vary

greatly with solar cycles. Trapped protons have energies below 400 MeV and the trapped electrons have energies below 7 MeV for the inner belt, and 10 MeV for the outer belt [11]. There exists a region in LEO called the South Atlantic Anomaly (SAA) where the magnetic field strength drops significantly allowing the belts to descend to a lower altitude [12]. Passes through this region will result in increased dose to the spacecraft from all radiation sources.

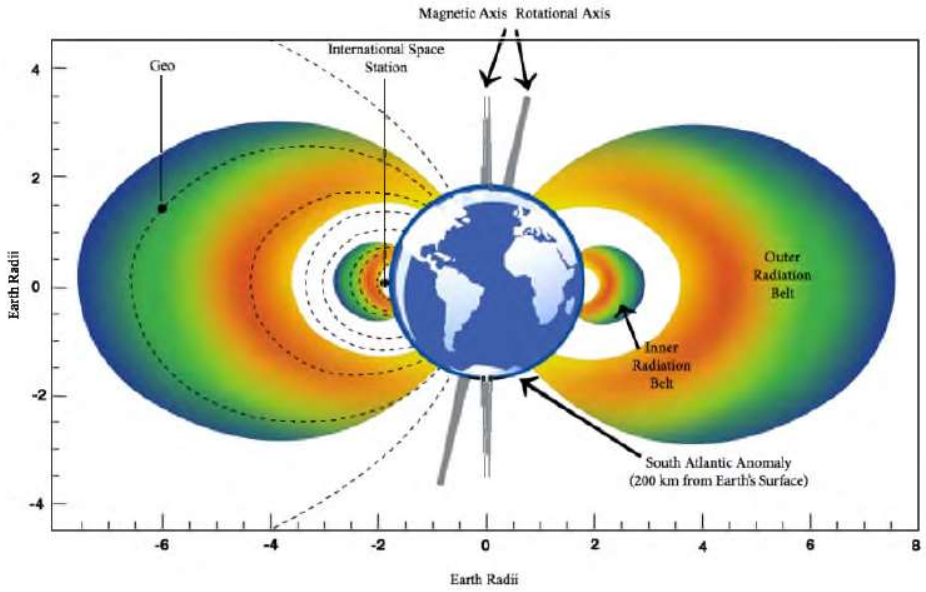


Figure 1.1 The Van Allen belts' location around the Earth in terms of Earth radii unit distances. Location of the SAA and the height of the International Space Station (ISS) are also indicated on the graph [10]. Color scale is qualitative.

Models for predicting the flux of different trapped particles and their energy distribution were developed based on the data collected by several experiments. Such models include AP8 and AE8 models from the 1980s by NASA for protons and electrons respectively, which are now being replaced by AP9 and AE9 [13, 14]. These models incorporate the solar cycle effect, with the solar max and min options. These models and others are implemented in the space environment information system (SPENVIS) from the European Space Agency (ESA). This system allows for

the best prediction of the space radiation environment from all sources using a plethora of different models.

An example for use of these models is shown using a typical Earth observation satellite orbital parameter as listed in Table 1.2. These parameters correspond to the Turkish Earth observation satellite IMECE, foreseen to be launched in 2022, on which YRM (Yerli Radyasyon Monitörü or Homegrown Radiation monitor) is planned to be installed. Observing the particle spectra with high enough statistics to distinguish SPEs from trapped particle fluxes in this orbit is the goal target during the design of YRM.

Table 1.2 Orbital parameters describing a typical circular heliosynchronous orbit for an Earth observation satellite [15].

Orbital Parameter	**Value**
Apogee	680 km
Perigee	680 km
Inclination	98 Degrees
Period	1.64 Hours

The resulting trapped particle fluxes are plotted in Figure 1.2, for protons (A) and electrons (B). The fluxes at the low energies are several orders of magnitude higher than at higher energies for both and the electron flux of is at least 2 orders of magnitude larger than protons up to few MeV after which it falls sharper. A design for an efficient radiation detector sensitive to both electrons and protons separately should factor this difference in its optimization process. Any proton detector sensitive to energies below 5 MeV will suffer from a large electron background. It is also important to note that most of the trapped proton flux is below a few hundred MeV.

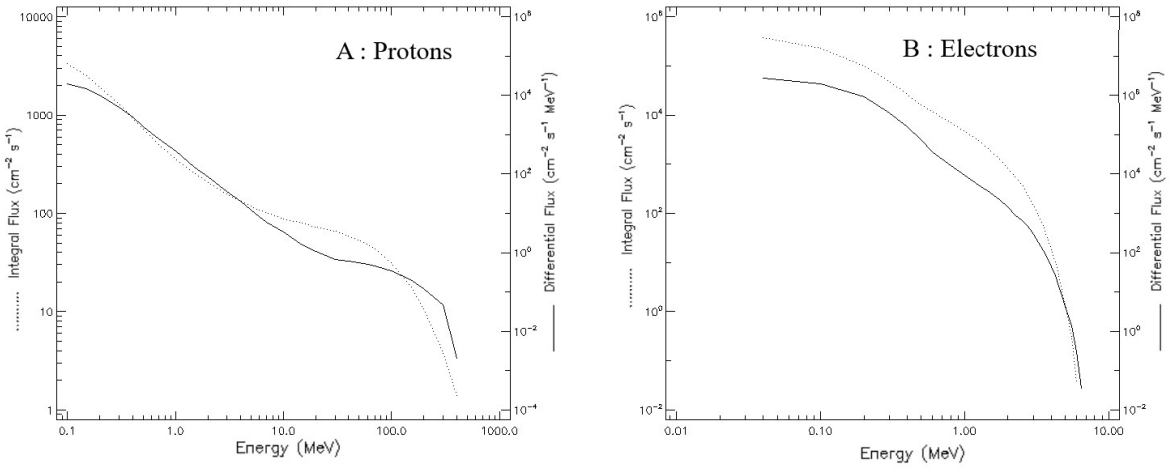


Figure 1.2 Differential trapped protons (A) and electrons (B) spectra at LEO obtained from a SPENVIS simulation using AP8 and AE8 models respectively.

The distribution of the proton flux in orbital coordinates calculated for January 2010 for 20 orbits over 1.36 days can be seen in Figure 1.3. Most of the flux is seen in the polar region and near the SAA. The highly elliptical orbit of IMECE spans a large area of the Earth's surface within a few orbits due to the Earth's rotation.

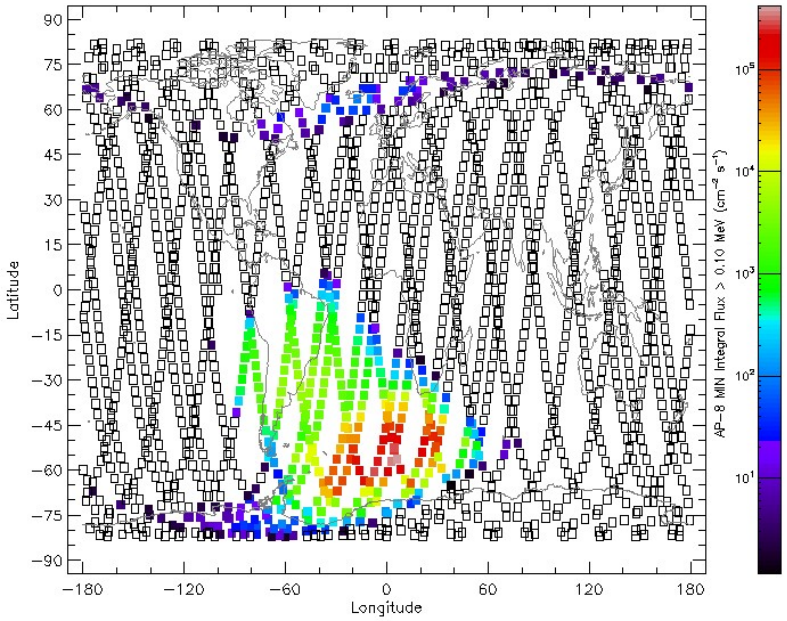


Figure 1.3 The distribution of the proton flux seen by IMECE in 20 orbits projected onto the Earth in orbital coordinates from a SPENVIS simulation.

1.1.2 Solar Particle Events (SPE)

Energetic nuclear reactions inside the Sun followed by magneto-hydrodynamic processes on its surface yield a very high flux of particles known as the Solar wind. Solar events such as sunspots and flares create ions that are ejected from the Sun at high energies (>100 MeV). The poles of the Sun swap every 11 years, also known as the Solar cycle, causing disturbances in the Sun's magnetic field, releasing a massive amount of radiation. During a cycle, there are 7 years when the solar activity is high, followed by 4 years of solar minimum when the solar activity is low [16]. The Carrington event in September 1859 is generally considered as the heuristic for the upper limit on particle fluences produced by SPEs at 1.88×10^{10} particle/cm^2 during a period of 2-3 days [17]. Heavy ions such as alpha particles and oxygen ions are also ejected by SPEs. Depending on the solar cycle, the absorbed dose per year by a satellite will vary drastically. However, in the process of designing a radiation monitor such as YRM, using the solar maximum as the design requirement to calculate the maximum particle rate on a sensor will result in a robust design that will not be oversaturated by foreseeable SPEs of high magnitudes. For the orbital parameters given in Table 1.2, an interval at the peak of the solar cycle (01/01/2010 to 01/01/2011) was used to calculate the peak particle fluxes of protons and the most prominent heavy ions (Helium followed by Carbon and Oxygen) in SPENVIS as shown in Figure 1.4 A, B, C and D respectively. At the solar maximum, the flux of SPEs exceeds that of trapped particles by several orders of magnitude for a short period of time (~6 months). The design of YRM must be able to observe such increases in the particle fluxes without getting oversaturated. Solar particles and heavy ions also become very prominent in the polar regions of LEO since the magnetic field strength diminishes.

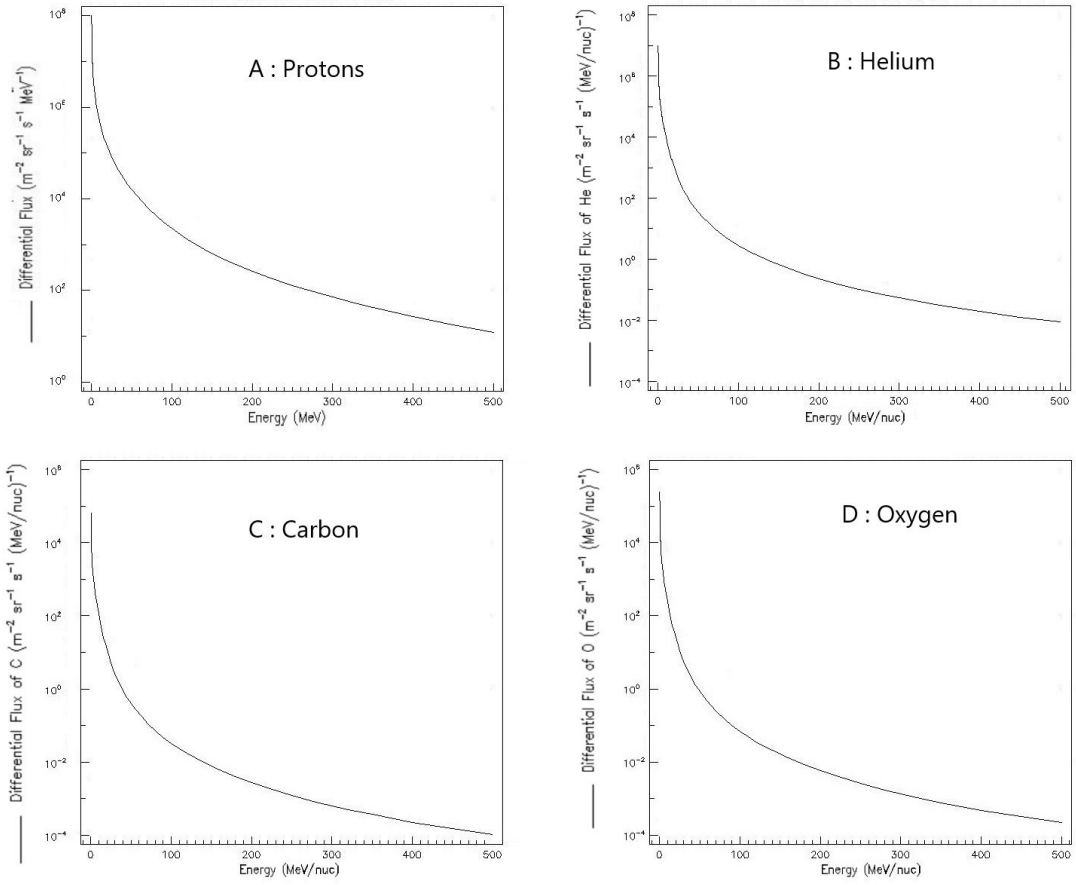


Figure 1.4 Differential solar proton (A), He ions (B), C ions (C) and O ions (D) peak flux for a satellite in LEO obtained from a SPENVIS simulation using CRÈME-96 model at solar maximum (A). Spectrums for heavy ions are plotted with respect to kinetic energy per nucleon.

1.1.3 Galactic Cosmic Rays (GCR)

The exact mechanism of creation of galactic cosmic rays is still unknown [18]. However, supernovae and their remnants are known to create an immense flux of particles at very high energies (~1 TeV) and accelerate surrounding particles as well. The GCRs are observed to be isotropic in nature. The composition of GCRs have been extensively analyzed by various experiments such as AMS-02 [19]. Heavy ion constituents of the GCRs are also high in energy and contribute significantly to the

absorbed dose of a spacecraft in LEO. The fluxes of heavy ions generally decrease with increasing Z (atomic number) as shown in Figure 1.5, which were obtained using the CREME96 database available in SPENVIS. The energy distribution of GCRs can reach $\geq 10^{11}$ GeV [20]. Low-energy GCRs below the geomagnetic cutoff follow the Earth's magnetic field lines to the poles, resulting in higher flux in LEO, whereas the GCR flux is reduced at the equator.

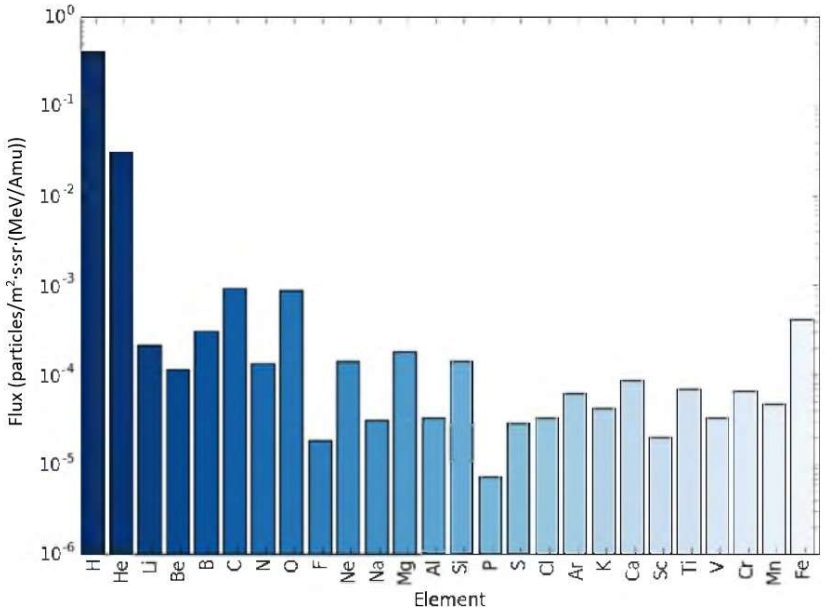


Figure 1.5 Heavy-Ion fluxes at 1 MeV extracted from the CREME96 database [21].

Table 1.3 Summary of properties of different categories of the space radiation environment al LEO.

Property	Van Allen Belts	Solar Particle Events	Galactic Cosmic Rays
Composition	Electrons < 7 MeV - Protons <400 MeV	Low Energy Protons and Electrons Heavy Ions	87% Protons 12% Alpha Particles 1% Heavy Ions 2% Electrons Positrons
Effect of magnetic field	Geomagnetic cutoff in LEO depends on latitude	Existence of SAA	Geomagnetic cutoff in LEO with depends on latitude
Prediction models	AE8 AP8 AE9 AP9	ESP-PSYCHIC NOAAA CREME96	CREME96

1.1.4 Cosmic Ray Showers in the Atmosphere

When cosmic rays enter the Earth's atmosphere, they interact with the air to produce particle showers [22, 23]. GCR primaries that are above the geomagnetic cutoff will proceed towards the surface of the Earth generating secondary particles. These secondaries will then collide with air as they traverse through higher and higher densities of air. The resulting particle shower consist neutrons, electrons, muons, kaons, pions and neutrinos as illustrated in Figure 1.6. Especially charged muons can traverse long distances through the atmosphere and reach the Earth's surface without decaying or getting absorbed, which allows for muon detection on the Earth's surface [24].

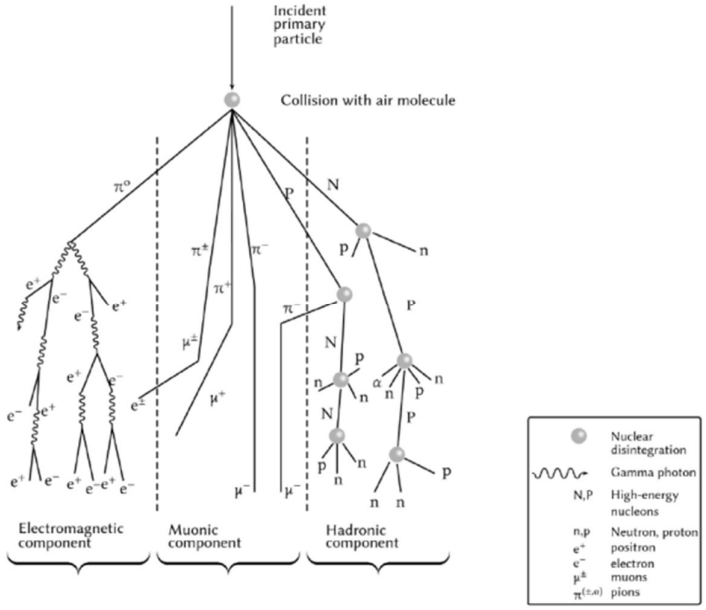


Figure 1.6 Illustration of the cosmic ray shower components. Particles resulting from electromagnetic, hadronic and muonic interactions and shown in different sections [25].

Theoretical models and Monte-Carlo simulations predict a maximum flux of secondary particles (muons, electrons and pions) at an altitude of ~20 km called the Regener-Pfotzer maximum as shown in Figure 1.7. The primary flux of protons decreases exponentially as the altitude decreases, while the flux of secondary electrons, positrons, neutrons, muons and pions reach a maximum around an altitude of 20 km and then decrease rapidly as they approach the Earth's surface. These fluxes are calculated using the newly developed CARI7-A simulation software. CARI7-A is developed by the Federal Aviation Administration's Civil Aerospace Medical Institute. Based on MCNPX2.7.0, it simulates the atmospheric response to a primary GCR spectrum and generates secondary particles accordingly. The particle fluxes in Figure 1.7 were generated using the ISO 2004 model for the primary GCR flux and using the coordinates N'42 and E'35 on October of 2020 [26].

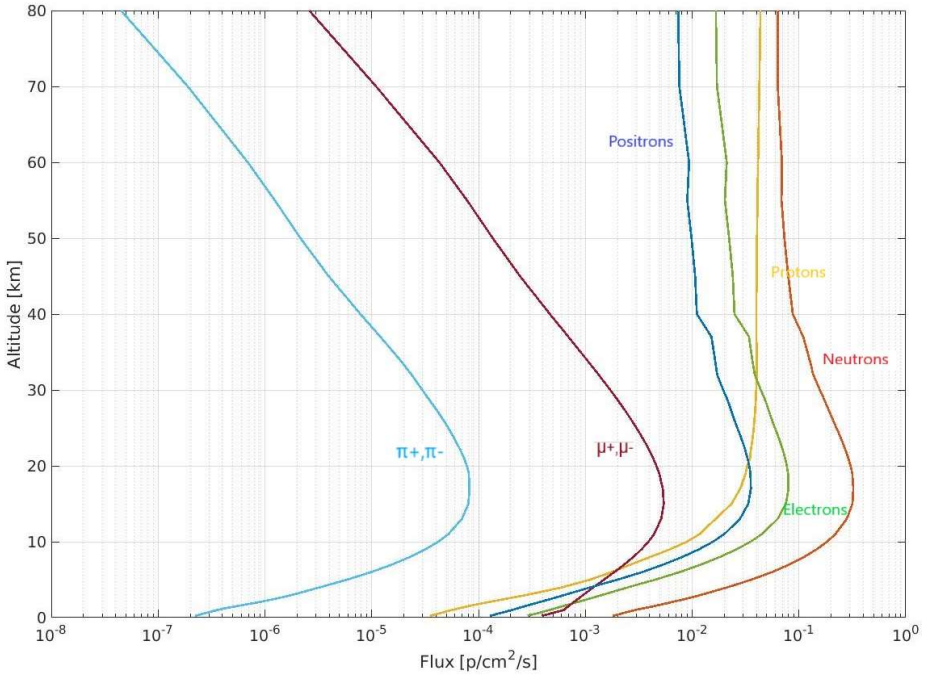


Figure 1.7 Calculated flux of different particles at different altitude using CARI7-A software with the ISO-2004 model for altitudes above (N'42, E'35).

Measurements of the radiation dose in the atmosphere were being performed since the 1950s. Balloons and aircraft were used extensively to measure the profile in different altitudes below 35 km. The accumulated results also show a peak in the dose rate at an altitude of 20 km [27, 24, 28]. Figure 1.8 shows data accumulated from over 70,000 balloon flights over the past 50 years in the USSR [20]. Regener-Pfotzer maximum can be clearly discerned in the figure for the flights above Moscow while being more subtle in more northern regions with cutoff rigidities lower than 1 GV [27].

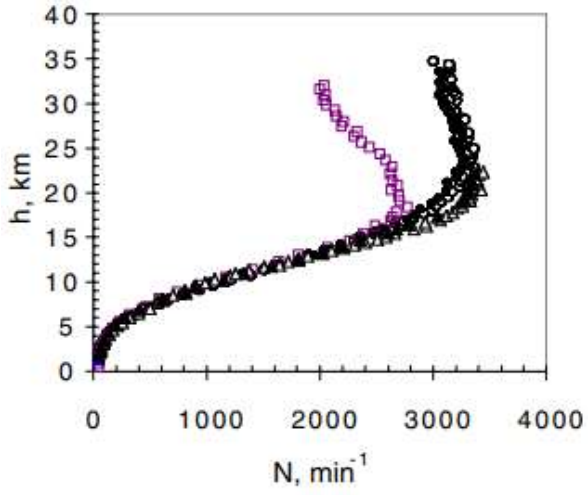


Figure 1.8 The count rate vs. altitude in the atmosphere. at the northern polar latitude, Murmansk region, Rc=0.6 GV (the radiosonde flights on 2 and 4 September 1997 - open circles and black points, accordingly); at Mirny in the Antarctic, Rc=0.04 GV (the flights on 3 and 8 September - open and black triangles, accordingly); at the middle latitude, Moscow region, Rc=2.4 GV (the flight on 3 September - open purple squares) [27].

Recently, in March of 2019, a REXUS sounding rocket was flown from Esrange Space Center in northern Sweden with 3 cameras and a scintillator detector to measure particle flux data in the upper atmosphere up to 80 km and recovered [29]. The measurement from the scintillator sown in Figure 1.9 does not have a Regener-Pfotzer maximum because the measurement was performed at a high latitude (N'68). The measurement from the cameras did not survive the flight and the data got corrupted.

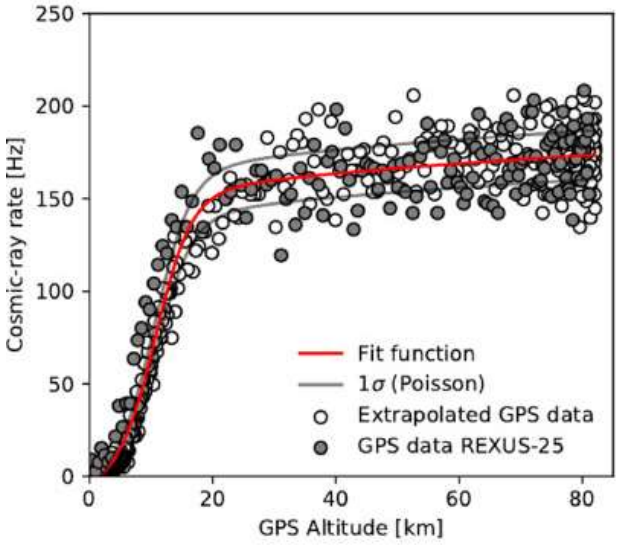
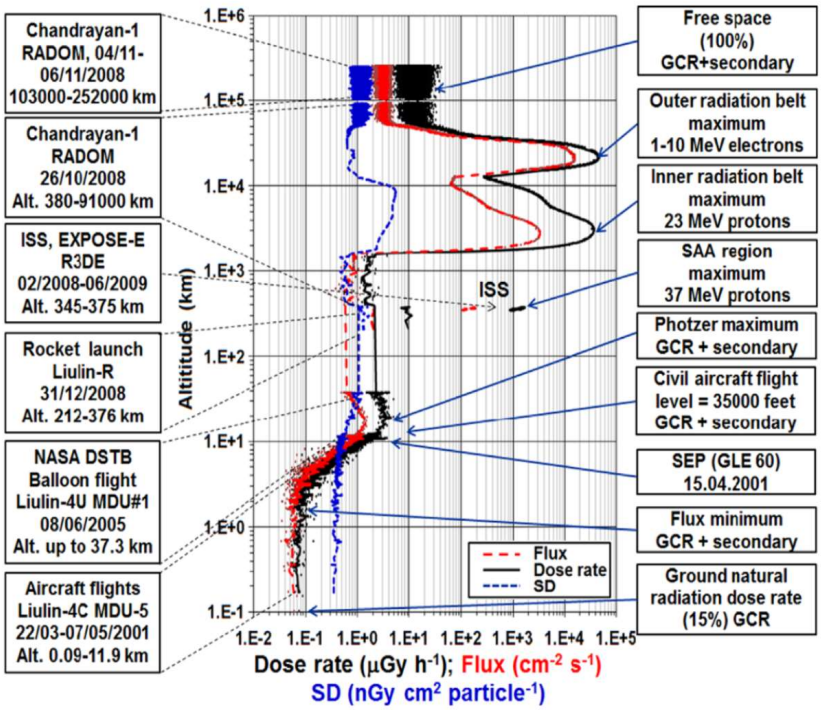


Figure 1.9 Cosmic particle count-rate data obtained from sounding rocket flight using a NE-110 plastic scintillator detector [29]. Measurement does not show a Regener-Pfotzer maximum due to very high latitude of the launch location.

A summary of the available radiation measurement data is provided by [24] and is shown in Figure 1.10. Both dose rate and flux show a clear increase in particle count at around 20 km as well as in the inner (1600 km to 13000 km) and outer (19000 km to 40000 km) van Allen belts. Also, the flux in the SAA is two orders of magnitudes higher as measured by the ISS. The specific dose (SD) is a measure of the average energy per particle and changes slightly with altitude as the dominant particle in the GCR spectrum change with altitude. Between 35 and 220 km, there is no available data because it can only be covered by rockets which only spend a limited time there.

This thesis presents a measurement of the dose rate and particle counts in the atmosphere and space up to 136 km to fill this void.



Point description, number of the measurements used, time [dd/mm/yyyy]	Averaged altitude, and range [km]	Averaged geographic coordinates [long, lat]	Averaged dose rate and range [μGy h^{-1}]	Averaged flux and range [cm^{-2} s^{-1}]	Averaged SD and range [nGy cm^{-2} $particle^{-1}$]
Ground, 2431, 22/03-07/05/2001	~0.1	48°N, 2°W	0.073 0.026–0.212	0.059 0.0028–0.111	0.346 0.213–1.15
Flux minimum, 10, 22/03-04/05/2001	1.6 1.56–1.7	45°N, 51°W	0.073 0.049–0.114	0.052 0.04–0.072	0.386 0.325–0.645
***SEP on 15 April 2001 (Maximum exposure),* 1, 13:42 15/04/2001**	Fixed at 10.67	53°N, 26°W	3.66	1.46	0.696
Civil aircraft flight level between 34,000 and 36,000 ft (10.67 km), 559 points, 22/03/2001-05/05/2001	10.55 10.36–10.67	52°N, 31°W	1.62 0.85–2.33	0.921 0.534–1.068	0.49 0.40–0.64
Photzer maximum (Flux maximum), 1, 08/06/2005	14.7	44°N, 107°W	2.9	1.46	0.55
Photzer maximum (Dose rate maximum), 4, 08/06/2005	18.65 18.3–19.01	44°N, 107°W	4.38 2.66–5.94	1.36 1.28–1.48	0.89 0.87–1.22
HotPay2 rocket trajectory, 14 31/12/2008	312 211–376–204	70.7°N, 14°E	8.99 4.8–11.8	1.9 1.68–2.15	1.3 0.79–1.89
South-Atlantic Anomaly maximum (Ascending node orbits), 116 22/02/2008-23/06/2009	360 347–371	31°S, 51°W	948 626–1195	113 76–140	2.33 (38 MeV) 2.04–2.53
South-Atlantic Anomaly maximum (Descending node orbits), 122 22/02/2008-04/06/2009	361 349–371	31°S, 51°W	1310 882–1640	154 104–192	2.37 (37 MeV) 2.24–2.51
Inner radiation belt maximum, (Flux maximum), 2, 26/10/2008	2730 2707–2753	15.3°S, 165°E	35,489 34,811–36,167	3279 3274–3284	3.0 (26 MeV) 2.95–3.06
Inner radiation belt maximum, (Dose rate max.), 2, 26/10/2008	3007 2984–3030	15.3°S, 165°E	37,279 37,254–37,305	3127 3099–3156	3.28 (24 MeV)
Outer radiation belt maximum, (Flux maximum), 7, 26/10/2008	20,300 20,180–20,436	15.8°S, 149°W	44,200 43,745–44,642	16,021 15,976–16,053	0.766 0.757–0.773
Outer radiation belt maximum, (Dose rate max.), 8, 26/10/2008	21,260 21,111–21,409	15.8°S, 149°W	46,090 42,462–47,132	14,978 13,460–15,539	0.86 0.823–0.883
Free space, 8710, 06/11/2008	230,000 200,000–252,000		12.87 4.6–41.3	3.16 1.71–4.71	1.13 (169 MeV) 0.51–3.25

Figure 1.10 Variations of the absorbed dose rate, flux and specific dose for an altitude range from 0.1 to 250,000 km with tabulated data concerning points of interest [24].

1.2 Radiation Detectors in Space

In the past 50 years, several detectors were designed for the purpose of measuring the Earth's radiation environment. Radiation detectors vary greatly depending on their mission goals and design limitations. Large detectors (≥ 1 ton) were deployed in space for extensive scientific studies of energetic particles such as AMS-02 [20] and PAMELA [30] and Fermi gamma ray space telescope [31]. These detectors measure cosmic rays in a wide energy range (100 MeV to TeV) with very high accuracy and statistics to study dark matter, primordial antimatter and galactic gamma ray sources. While other smaller detectors have a smaller profile and a narrower range (<500 MeV/nuc) for a variety of purposes ranging from scientific research to ion thruster exhaust characterization. In this section, the major small sized active radiation detectors in space are investigated.

1.2.1 The Van Allen Probes

Launched in 2013, van Allen probes are twin satellites designed to carry identical detectors into the van Earth's radiation belts in opposing orbits. The highly specialized instruments carried by the probes are summarized in Table 1.4 [32].

Table 1.4 Instruments abroad the van Allen probes and their functions [32].

Instrument	Aim
RBSPICE: Radiation Belt Storm Probes Ion Composition Experiment	Investigation of storm-time ring current
Energetic Particle, Composition, and Thermal Plasma Suite (ECT)	Investigation of electron, proton and heavy ion fluxes at low energies
Electric and Magnetic Field Instrument Suite and Integrated Science (EMFISIS)	Measurement of electric and magnetic field effects on particle acceleration in Earth orbit
Electric Field and Waves Suite (EFW)	Investigation of how the electric fields energize radiation particles and modify the structure of the inner magnetosphere
Relativistic Proton Spectrometer (RPS)	Measurement of high energy protons (up to 2 GeV)

Detectors onboard the van Allen probes are currently taking data to help verify the AP9/AE9 models of the radiation belts, as well as understand the flux of high energy particles which are thought to be underestimated by previous models [33]. The particle radiation monitors on the ECT mainly use magnetic spectrometry to measure the energy of the particles in relation to the Z/m ratio. Separate silicon detectors for electrons, protons and heavy ions makes charge discrimination and particle identification possible. Measurements of the ECT are being compared with the other detectors and previous models to improve the understanding of the radiation belts [32].

1.2.2 SEMS and RAD

Space Environments Monitoring Suite [34] is an instrument designed by NASA to measure the radiation environment of its host satellite in LEO or GEO. This device which is intended to fly abroad the Solar Electric Propulsion- Technology Demonstration Mission (SEP-TDM) includes several modules, of which the RAD module is in charge of measuring proton and heavy ions ($Z< 26$). It consists of a silicon telescope with 3 solid-state detectors to measure protons with kinetic energies from 50 keV to 100 MeV. The detector is designed in part to fulfil NOAA's needs for monitoring of solar winds for weather forecasting. The RAD unit is compact with a mass of 2 kg and a volume of 1 L. It is also designed to minimize power consumption at 4 W.

1.2.3 EPT

The Energetic Particle Telescope (EPT) [35] was designed by Université Catholique de Louvain / Center for Space Radiations (Belgium) in cooperation with ESA to achieve a good resolution of energy spectrums of radiation particles in Earth orbit, while also maintaining compactness and low power consumption. It was launched in 2013 onboard the Proba-V satellite. It fits into a volume of $127.5 \times 162.0 \times 211.5$ mm^3 and has a mass of 4.6 kg, which is slightly larger than the RAD unit made by NASA. However, it exceeds the performance of the RAD unit by being able to measure electron fluxes in the energy range 0.5–20 MeV, proton fluxes in the energy range 9.5–300 MeV and He-ion fluxes between 38 and 1200 MeV. To achieve this, EPT uses 23 Passivated Implanted Planar Silicon (PIPS) detectors for particle identification and energy measurement, packed into doublets in a modular array as shown in red in the cross section in Figure 1.11 [35]. The doublets can be added or removed according to mission criteria and serve primarily for energy measurement of the incoming particle, while the three singlet detectors at the

entrance (S1, S2, S3) serve the purpose of measuring the total flux as well as the field of view of the telescope.

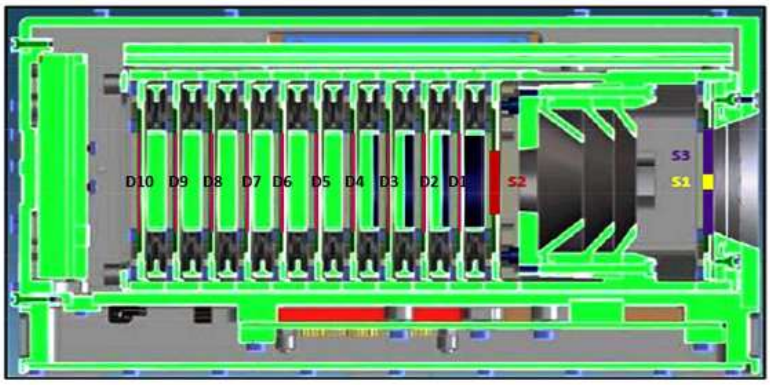


Figure 1.11 View of the cross section of EPT spectrometer, doublets (D) modules are shown in red while singlet (S) modules comprise of single detectors for field of view definition [35].

1.2.4 MuREM/RM

MuREM is designed by the UK Space Agency as a commercial radiation monitor for spacecraft. It launched for the first time on 2014 abroad the TechDemoSat-1 mission [36]. It houses two silicon PIN diodes for proton (>30 MeV) and heavy ion detection. The compactness of this device comes at the cost of the quality of the data it can collect. With a mass of 0.5 kg and a power consumption of 0.5 W it has a very good profile to suite most spacecraft. The reduced measurement ranges for protons and the lack of electron radiation measurement highlight its shortcomings. The design also includes multiple RADFETs for passive TID measurement.

1.2.5 SATRAM

The Space Application of Timepix Radiation Monitor (SATRAM) incorporates the Timepix silicon pixel detector (300 μm thick silicon sensor, pixel pitch 55 μm, 256×256 pixels) [37]. Designed and flown by the ESA abroad the Proba-V satellite in 2013, it can measure protons and electrons in the ranges 0.5-7 MeV and 10-400

MeV respectively. The added spatial resolution from using pixel detector helps identify particles with high accuracy albeit at a high power consumption for its weight. SATRAM uses 2.5 W of power while weighing only 380 g. The data collected from the pixel detectors is very helpful in understanding and characterizing the anisotropy in the radiation belts around the earth. A photograph of the unit attached to Proba-V is shown in Figure 1.12. While Proba-V already carries a capable radiation detector, the directional measurement capabilities of the Timepix detector along with the placement of the SATRAM unit onboard the satellite is able to measure the directional (East-West) drifting of trapped particles.

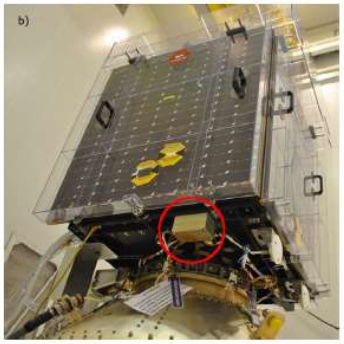


Figure 1.12 Photograph of the SATRAM unit placement onboard the Proba-V satellite.

1.2.6 MFS & BERM

Made by the Portuguese EFACEC company, MFS and BERM are both layered silicon detector radiation monitors contracted by the ESA [38]. Both contain a stack of 11 silicon detectors as shown in Figure 1.13. The stack of detectors is placed in a telescope arrangement to allow for energy spectrometry of the incoming charged particles with energy degraders in between. The two designs have minor differences between them to suit different mission profiles and satellite dimensions. Identification of particles is performed based on pulse height discrimination in the silicon detectors' signal. A comparison between the two designs is shown in Table 1.5.

Table 1.5 Comparison between MFS and BERM design parameters [38].

Parameter	MFS	BERM
Power Consumption	4 W	5 W
Weight	2.914 kg	2.143 kg
Envelope	257.3x120.0x108.0 mm^3	174.8x120.0x107.0 mm^3
Electron sensitivity	0.45 to 7 (7 bins) MeV	0.3 to 10 (5 bins) MeV
Proton sensitivity	1 to 120 (10 bins) MeV	1 to 200 (8 bins) MeV
Alpha sensitivity	5 to 400 (10 bins) MeV	------
Heavy Ion sensitivity	1 to 50 (10 bins) MeV	1 to 50 (5 bins) MeV

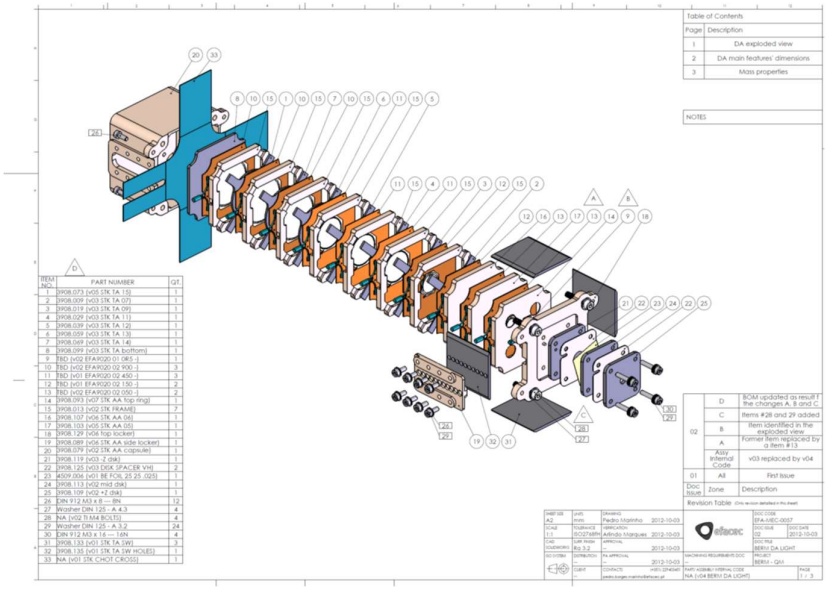


Figure 1.13 Exploded view of BERM internals, Silicon detectors are shown [38].

1.2.7 Common Features

In sections [1.2.1-1.2.6], the design of different existing radiation monitor devices was investigated. The similarities between these devices include the limitation imposed by deployment in space, namely the power consumption, mass and volume limitations. Other common factors include the consistent use of silicon detectors for their proportional response to the deposited energy by traversing ionizing particles. These detectors are placed in telescope arrangements to achieve a wide energy measurement range and to allow for coincidence detection. Collimators are also used

to limit the flux of the incoming particles and to define a field of view for the telescope setup. Pulse height discrimination is also consistently used for particle identification as well as energy measurement.

Silicon PIN diodes are widely used in space and radiation applications due to their high-speed response, relatively low price and small size [39, 40]. Silicon has a low band gap energy of 1.11 eV at 300 K [41]. They are made of 3 layers of silicon, a pure intrinsic (I) silicon region sandwiched between a p-doped region (P) and an n-doped region (N). As the general schematic shown in Figure 1.14 illustrates, a high reverse voltage (10 - 1000 V) is applied to the diode to deplete the intrinsic region [42]. A passing ionizing particle can create electron-hole pairs in the depleted region by depositing its energy. The charge carriers then travel to the cathodes where the current is collected and directed to the readout circuit for amplification and digitization.

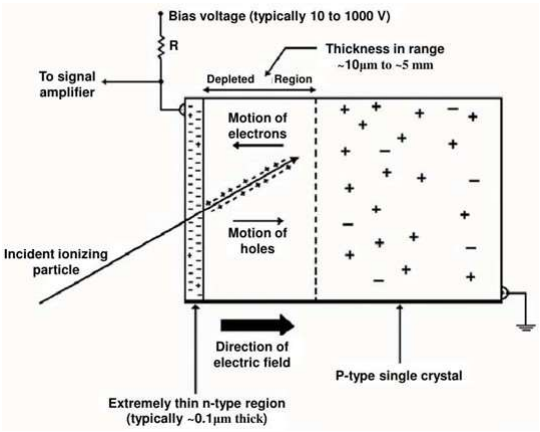


Figure 1.14 General schematic of the working principle of the silicon PIN diode for charged particle detection.

To summarize, the factors common to most of the previous designs are listed below:

- Employment of silicon detectors

  The low band gap of silicon allows for the creation of a high number of electron hole pairs for sensitive measurements.

- Proportional energy deposition and amplification
  The signal output is directly proportional to the energy deposited inside the silicon detectors.
- Telescope arrangement
  Parallel layers of silicon are sandwiched between moderators. The particle penetrates through the telescope and stops at a certain layer, which with coincidence logic allows for the identification of the particle energy.
- Collimators for the field of view definition
  Collimators shield a lot of particles from the detector signal by obstructing their flight path, sacrificing statistics to allow for a better accuracy in energy measurement.
- Pulse height discrimination for charge identification
  Using the proportionality of the deposited energy to the square of the charge, the height of the pulse can be used to distinguish particles and energies using thresholds.

1.3 Interactions of Charged Particles with Materials

When an energetic particle enters a medium, certain physical processes will occur with different probabilities. Different types of particles will interact in different ways. In this thesis, the focus will be towards the interactions of electrons and protons and heavy ions travelling through matter. These will interact electromagnetically with the electrons and the nuclei of the materials they traverse through multiple processes, which include elastic and inelastic scattering, ionization, bremsstrahlung radiation and various other nuclear and atomic interactions [43].

The amount of energy lost by a charged particle and deposited in the medium depends on the type of particle, its mass, charge, initial energy, the medium and the interaction that took place. All interactions occur with a certain probability called the cross section that depends on many factors such as the energy of the particle and what it is interacting with [43].

The scope of this thesis revolves around protons of energies between 1 MeV to 1 GeV, heavy ions of energies less than 10 GeV as well as electrons of energies between 100 keV and 10 MeV which will be described later. This limits the number of interactions to be considered since the cross sections of many high energy physics processes are negligible.

A good method of estimating the energy loss per unit length of a proton or ion in this energy region is described by the Bethe-Bloch formula given below [44]:

$$-\frac{dE}{dx} = 2\pi N_a r_e^2 m_e c^2 \rho \frac{Z}{A}\frac{z^2}{\beta^2}\left[\ln\left(\frac{2m_e\gamma^2 v^2 W_{max}}{I^2}\right) - 2\beta^2 - \delta - \frac{2C}{Z}\right] \qquad (1.2)$$

Here, the classical electron radius is denoted by r_e, the electron mass by m_e, Avogadro's number by N_a, the mean excitation potential by I, the atomic number of the medium's material by Z, the atomic weight of the medium's material by A, the density of absorbing material by ρ, the charge of incident particle in units of e by z, β is the Jackson number (βv/c; particle speed divided by speed of light) of the incident particle, γ is the Lorenz factor ($\gamma = 1/\sqrt{1-\beta^2}$), δ is the density correction, C is the shell correction and W_{max} is the maximum energy transfer in a single collision.

The density correction is important for high energies of incident ions, while the shell correction is important for low energies. This formula predicts the energy loss of high energy particles is much less than that of slower particles. This behavior of particles results in the Bragg peak, which is the prediction that as the particle loses more and more of its energy inside a material, the rate with which the energy is lost increases. When the particle has deposited almost all of its energy in the material, i.e. it has almost reached its "range", the graph of dE/dx versus the particle's penetration depth exhibits a peak as seen in Figure 1.15. The heavier the ion, the sharper the peak gets independent of its initial kinetic energy.

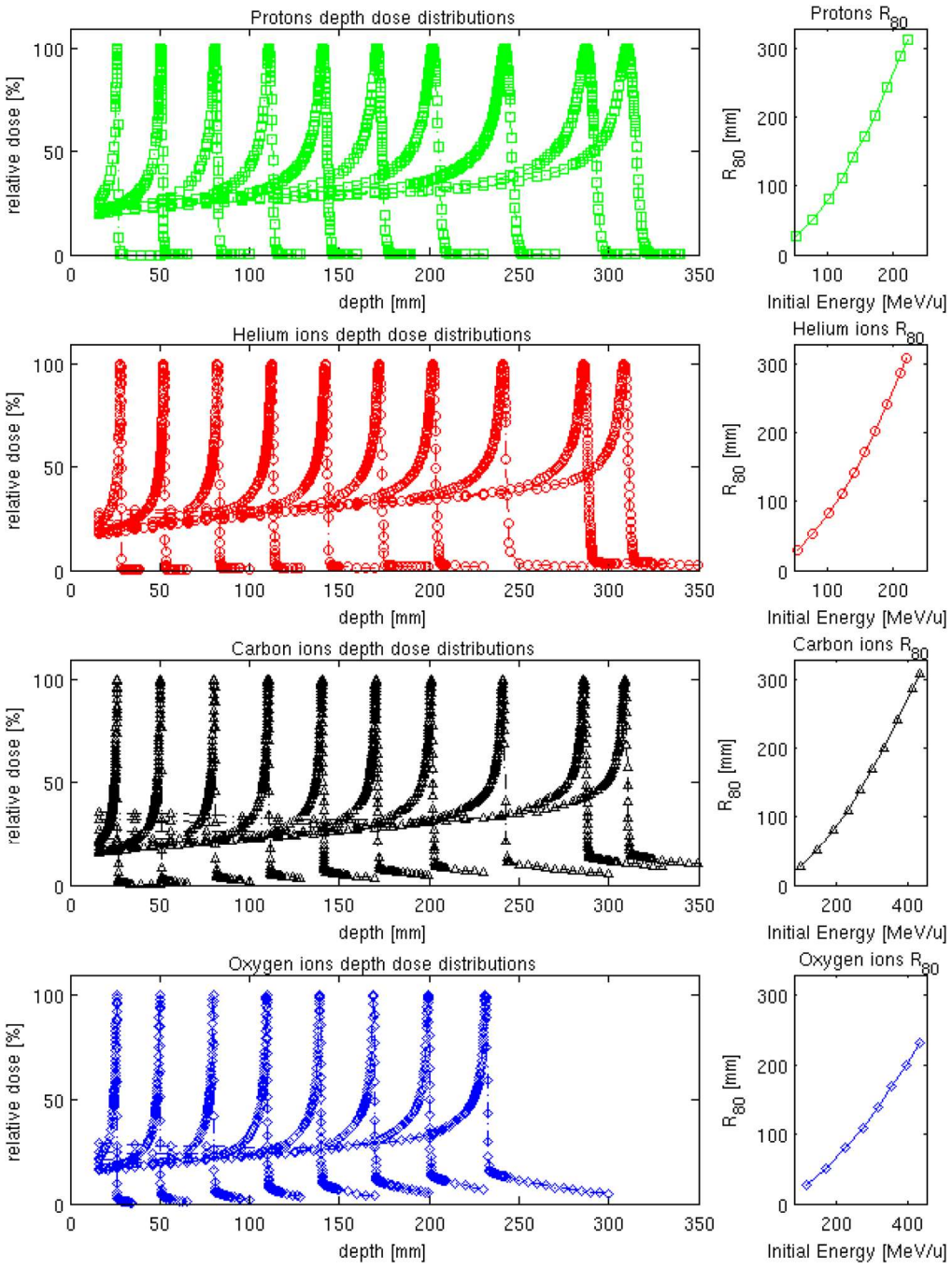


Figure 1.15 Bragg peaks normalized to relative dose, drawn for protons, alpha particles, carbon ions, oxygen ions(left) and the range at which 80% of energy is deposited per nucleon (right) for different initial kinetic energies. [45].

The range of a particle inside a material depends directly on the material's density. Thus, heavier shielding materials can stop more particles per unit depth. An investigation of the relationship between a particles momentum and its energy deposition yields the result that there exists a point of minimum energy loss for all particles at $\beta\gamma \approx 3$ as can be seen from Figure 1.16. Particles at this value are regarded as minimum ionizing particles (MIP).

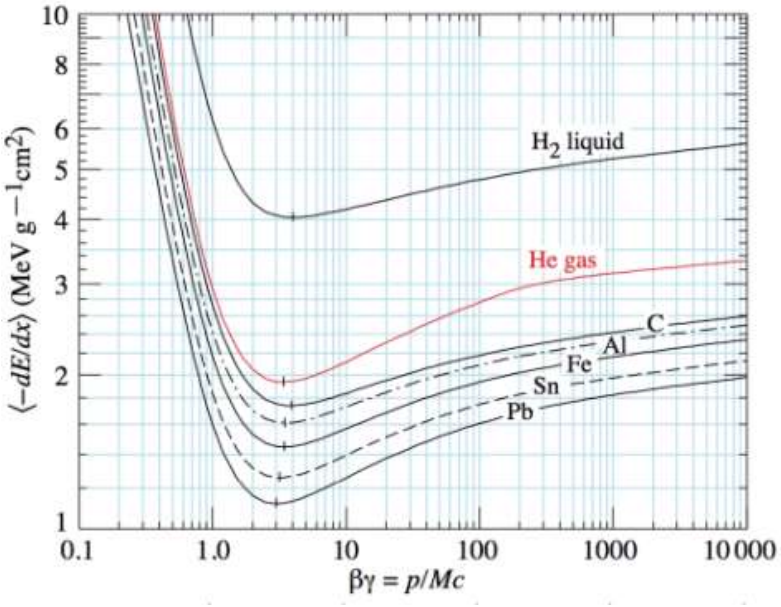


Figure 1.16 The differential energy loss as a function of $\beta\gamma$ showing the minimum energy transfer point for different particles [46].

Electrons exhibit a different pattern in the relationship between kinetic energy and penetration depth. That is because the mass of the electron and its leptonic nature subjects it to different physical interactions than protons or other heavy ions. The threshold of pair-production process of the electron is about 1 MeV and so the range calculations of electrons have to be different before and after this threshold. Electrons produce showers of secondaries when they enter a material through inelastic scattering, pair production and annihilation [44]. The energy of the electron is the determining factor in the distribution of these showers in terms of their

daughter particles, depth and width. It is hard to predict with high accuracy the results of these showers, so usually Monte-Carlo simulations are employed to calculate the results of such interactions averaged over a high number of trials.

A comparison between the dE/dx values for different energies of electrons and protons in silicon is shown in Table 1.7. The electrons deposit much less energy per unit length in materials at these energies than protons and thus detecting electrons efficiently requires a thicker silicon detector. Electron dE/dx values also are similar across YRM's measurement range, making pulse height discrimination for determining electron energies at this range unfeasible.

Table 1.6 Sample dE/dx values for protons and electrons.

Energy [MeV]	Proton dE/dx [keV/μm]	Electron dE/dx [keV/μm]
0.1	118	0.79
0.5	60.5	0.39
1.0	41.3	0.35
5.0	13.5	0.40
10	8.0	0.48
50	2.1	0.90
200	0.83	2.4
500	0.52	5.7

1.4 Radiation Damage to Spacecraft Components

Reasons for satellite mission failure vary from case to case. Statistically up to 21% of all missions fail due to space radiation damage and up to 53% of all satellite failures have unknown causes, which could possibly stem from radiation related causes, since unlike temperature problems or mechanical problems, radiation

damage is hard to diagnose [47], unless there is a live radiation monitor, with which the failures can be correlated.

Failure and malfunctioning of electronic components in space due to radiation is caused mainly by single event effects (SEEs) [1, 48]. Such events may reduce the lifetime of the component or cause immediate failure. Understanding the radiation environment that the spacecraft was exposed to before failure is thus of utmost importance. A spacecraft that can survive its radiation environment will result for a longer mission time as well as allowing its components to be certified for heritage. This is important also for future missions where the use of components tested for specific radiation environments is favorable, since the damage received by electronic components and materials of satellites depend on the particle type such as protons and electrons and flux it was exposed to.

Protecting the spacecraft against radiation involves the design of shielding materials and radiation hard electronics to make the spacecraft serve for the longest reasonable time without failure [1, 49]. Knowing the radiation environment that the spacecraft will be exposed to will greatly influence the design process of these preventative measures.

Satellite and spacecraft have an outside enclosure for mechanical integrity, which also serves as a radiation and micro-meteorite shield. This shield is often 4-6 mm thick aluminum covered in MLI [50] which stop electrons with energies less than 5 MeV, which is where the flux of electrons is highest. For components inside the satellite the radiation damage from electrons can be neglected while for solar cells and antennas electrons remain the dominant damage mechanism. Three examples of mechanisms by which radiation damages the spacecraft components are further discussed.

1.4.1 Total Ionizing Dose (TID)

The accumulation of dose over a long period of time is one of the most common failure modes due to radiation damage [51]. Components of the spacecraft that lie outside the shielding receive significantly more amounts of accumulated dose compared to components shielded inside. That is largely due to the fact the large fluxes of low energy particles that cannot penetrate the shielding of the spacecraft can still cause TID damage to exposed-parts. Thus, measuring low energy fluxes of ionizing particles can be helpful for prediction and prevention of such faults.

1.4.2 Single Event Effects

Single Event Effects result in a change in performance of an electronic component when a single particle penetrates it. A number of different errors can occur in digital electronics when such an event occurs as summarized in Table 1.1 [52]. Errors are often classified into two categories, soft errors and hard errors. Soft errors are faults in the device's logic such as changing the value of a bit or a memory address. Error correcting memory can fix such issues by checking for bitflips and rewriting the lost information [53]. Hard errors on the other hand are malfunctions in the elements of a circuit that prevents them from working as they were intended to. This makes them much harder to fix and need some power cycle, hardware correction or even replacement of components or devices [53, 54]. SEEs are dependent on the linear energy transfer of the particles causing them.

Table 1.7 Types of Single Event Effects caused by radiation that might occur during mission time.

Abbreviation	Error Type	Explanation
SEU	Upset	Change in state of microprocessor or memory (Soft)
SET	Transient	Transient voltage pulse produced in node (Soft)
SEL	Latchup	Unusual high current state (Hard)
SES	Snapback	High-current state (Soft)
SEB	Burnout	High-current state that causes calamitous failure (Hard)
SEGR	Gate Rupture	Damage of the ability of gate to manage current flow (Hard)
SEFI	Functional Interrupt	Device pauses normal operations (Soft)

Since heavier ions have lower range and have sharper Bragg peaks in materials than protons, they tend to deposit a lot of energy in sensitive parts of semiconductors and other sensitive electronic components. Thus, they are considered to be more dangerous for spacecraft electronics. Their lower flux in earth orbit however balances this effect [55].

1.4.3 Displacement Damage

Charged particles and non-charged particles alike can deposit energy in materials via nuclear interactions independent of ionizing energy loss. Elastic scattering off the nuclei in materials can cause them to be displaced from their position in the lattice causing deformities [56]. The displaced nucleus will position itself in the lattice matrix as an interstitial deformity, while its empty lattice position will remain as a

vacancy as shown in Figure 1.17. The number of vacancies resulting in crystal structures due to radiation damage is dependent directly on the non-ionizing energy loss (NIEL) of the particle penetrating the crystal. Heavier ions penetrating the sensitive components have a higher elastic and non-elastic scattering cross section. Thus, increasing their NIEL and making them more dangerous in this regard to protons and electrons.

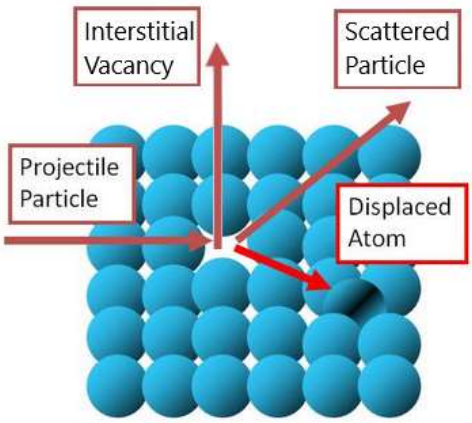


Figure 1.17 Illustration of damage caused to crystal structure after a displacement damage event.

As the incident hadron energy increases, the cross section for scattering increases exponentially. In the case of silicon, which is the base material for many sensitive components, protons with energies below 6 MeV have a large enough de Broglie wavelength that they do not interact with the nucleus and interact electromagnetically. At larger energies, silicon atoms will start to get displaced by the scattering processes. Protons with energies higher than 20 MeV will generate cascades of recoiled nuclei which in turn scatter other nuclei, significantly increasing the rate of deterioration to the silicon crystal [57].

YRM's measurement of electrons, protons and heavy nuclei will allow for correlation of the sustained damage to the satellite to the different modes of radiation damage (TID, ionizing, displacement). Its sensitivity cannot be determined analytically but only through detailed Monte-Carlo simulations.

1.5 Geant4 Simulations

Geometry and Tracking 4 (Geant4) is a Monte-Carlo simulation software toolkit for High Energy Physics developed by CERN [58]. The toolkit consists of libraries written in C++ for use by physicists all around the world. It is constantly under improvement with versions coming out yearly or semi-yearly. Throughout the period of writing this thesis, the most up-to-date version of Geant4 was used (10.6). The physics implemented within the simulations includes a wide variety of particles and processes, alongside the ability of the user to add any process, particle or mechanism as they desire. The methodology with which Geant4 libraries are used in this thesis is discussed in the following sections.

1.5.1 Geofactor Calculations

The geometric factor also known as the Geofactor, is an essential measure for the response of any particle telescope or cylindrical detector. It is defined by [59] :

$$C = \frac{1}{T}\int_{t_0}^{t_0+T} dt \int_S d\vec{\sigma}\cdot\hat{r}\int_\Omega d\omega \int_0^\infty dE \times \sum_\alpha \varepsilon_\alpha(E,\vec{\sigma},\omega,t) J_\alpha(E,\vec{x},\omega,t) \qquad (1.3)$$

where C is the counting rate [s^{-1}], J_α is the differential flux of the α_{th} kind of particle [$s^{-1}cm^{-2}sr^{-1}E^{-1}$], ε_α is the detection efficiency for the α_{th} particle species, t_0 is the time at the start of the observation, T is the total time of the observation, $d\vec{\sigma}$ is an element of the surface area of the detector, $d\omega = d\varphi d(cos\theta)$ is an element of the solid angle with an azimuthal angle φ and polar angle θ, $\vec{x}$ is the spatial position of the detector, $\hat{r}$ is the unit vector in the direction ω, S is the total area of the detector and Ω is the domain of ω. If the general expression is simplified such that ε_α is only a function of energy and J_α is only a function of energy and the solid angle, the simplified form below is obtained:

$$C = \int_{E_l}^{E_u} \underbrace{\left[\int_{\Omega} d\omega \int_{S} d\vec{\sigma} \cdot \hat{r} F(\omega) \right]}_{Geofactor} dE J_0(E) \tag{1.4}$$

where the expression inside the square brackets is called the Geofactor. $F(\omega)$ represents the angular dependency of the intensity of radiation with F=1 corresponding to isotropic flux. The Geofactor can also be called a response function, since it encodes the response of the detectors towards a certain energy of particles coming from a certain solid angle. In a loose meaning, it contains information of the probability of measuring a particle with a certain energy and angle of incidence on the detector.

Usually, the Geofactor accounts for limited energy particles arriving to the telescope from the directions allowed by the solid acceptance angle because of its collimator. But in the case of higher energy particles, penetration through the shields and the collimators is also possible, giving rise to further energy dependence of the Geofactor. This makes obtaining the energy dependence of the Geofactor a crucial step towards quantifying the telescope's performance.

In a series of Monte-Carlo simulations, the Geofactor can be measured by sending beams of mono-energetic particles of a certain energy to the telescope and measuring the telescope's response for each. The particles have to be sent from a 4π solid angle to measure the total range of the response. The Geofactor for a certain energy then simply becomes [60]:

$$Geofactor = \frac{n}{J} \tag{1.5}$$

where J is the flux generated inside the simulation and n is the number of events that cause an event in the aperture of the telescope. To simplify calculation, the telescope in the simulation is sent particles from a spherical surface of radius R in an isotropic manner as shown in Figure 1.18. The Geofactor then becomes:

$$Geofactor = \frac{n}{N} 4\pi^2 R^2 \quad (1.6)$$

where N is the number of primaries generated randomly and uniformly on the spherical surface. Positioning of the telescope in the sphere is inconsequential as the simulated radiation is isotropic and homogeneous [60].

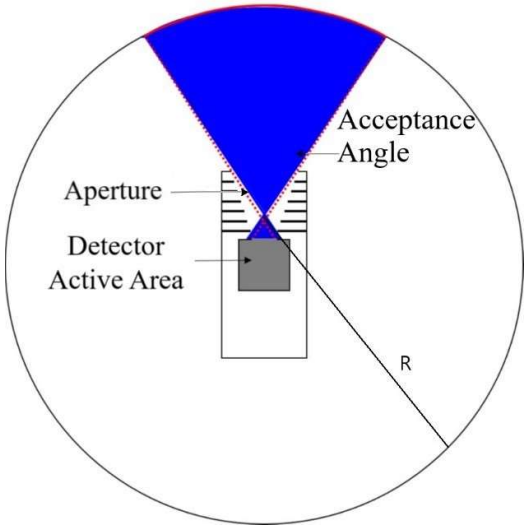


Figure 1.18 Placement of a typical telescope in a Monte-Carlo simulation to calculate the Geofactor.

In layered setups with multiple shields and energy moderators, such as the satellite that the telescope is attached to, the positioning of the detectors becomes more important as dependence on directionality increases. A simple work around is to set R to be much larger than the telescope's dimension L such that all detectors are effectively placed in the center of the sphere. This means that the lower hemisphere of the surface generating primaries will have no contribution to the value of n. Thus, it can be removed from the simulation safely with the transformation $N \rightarrow 2N$. However, this will cause a significant increase in the number of primaries needed by the simulation to reach significant statistics on the response of the telescope, which will in return increase the required simulation time. A tradeoff between the computation time and the accuracy necessary for a detailed design is made.

1.5.2 Simulation Physics

Geant4 simulations can incorporate a very wide range of nuclear and optical physics models. Generally, the physics models used by most Geant4 application developers are valid in high energy physics experiments, where the energy scale exceeds a few GeV. This creates many oversights in calculations in the low energy region, especially for electromagnetic interactions and neutron interactions. The physics in Geant4 works in a modular way, in which one can define new physics processes or a new class of particles (Leptons, Hadrons, neutrons …). These processes can obtain their cross-section data from either known mathematical models or directly from experimental datasets. Different available models for different particles can be seen in Figure 1.19. Default high energy physics lists (Firtoff string + Bertini Cascade) are generally used to save time on writing a more specific physics list and to cut the CPU time needed for the detailed calculations in the low energy regime.

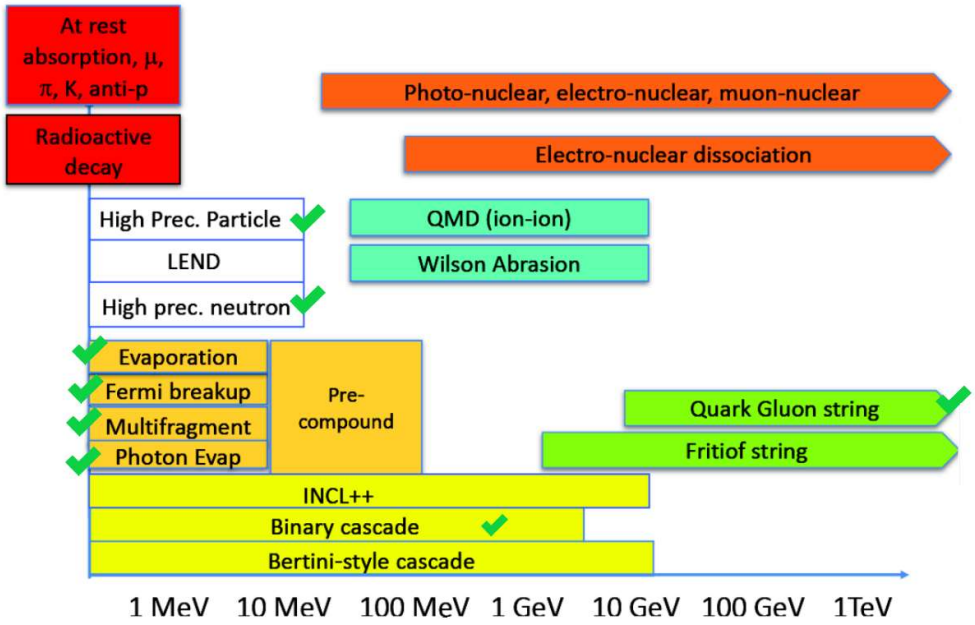


Figure 1.19 Physics models that can be used by Geant4 simulations and their validity energy region [61].

In the low energy regime (1 MeV → 500 MeV), which is the energy region that primarily concerns YRM for proton and electron detection in LEO, the models based on experimental databases have to be used for reliability and precision. The user must write their own physics lists using provided high precision modules for hadrons and ions and also incorporate low energy electromagnetic physics which are significant for the case of electron detectors. The complete physics list used in this work, upon the recommendation given in [39], is with a green tick mark shown in Figure 1.19. These models are more suitable for relatively low energy pace radiation environment rather than the high energy physics simulations Geant4 is set to do by default. Namely:

1- High precision heavy ion
2- Low energy electromagnetic physics
3- Low energy database for hadronic elastic scattering
4- Binary cascade model for inelastic scattering

The calculation of each physical process in Geant4 occurs in steps constituting the flight path of a particle. Each step has a process occurring at the start, along the way and the end. The minimum step length is determined by calculating the lifetime of daughter particles that are created in the step. If the daughters' lifetime times velocity corresponds to a distance less than the minimum step length, then the particle is deleted in that step and its energy is deposited in the volume defined by the step. Thus, the minimum step length is essential for calculating the energy deposition in a defined volume. In an example simulation, 45 MeV electrons were sent to a silicon detector with a thickness of 5 μm with different minimum step values (here called "production cuts in range"), the resulting energy deposition values are shown in Figure 1.20. Setting the minimum step length to a value higher than the thickness of the detector will result in the overestimation of the energy deposited in simulation volumes.

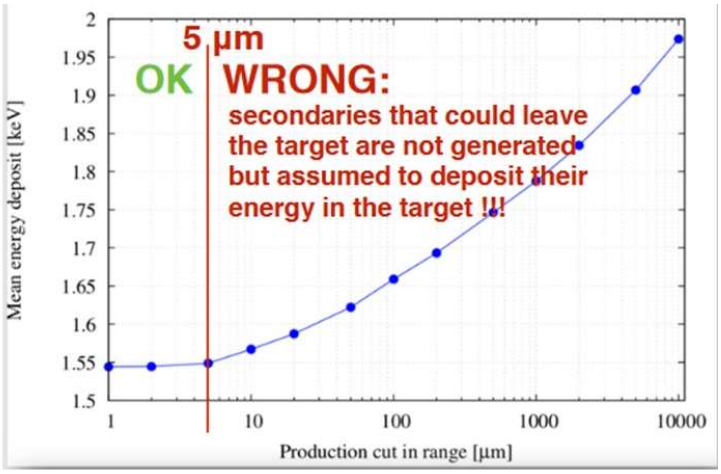


Figure 1.20 Energy deposition in sample silicon detector at different cutoff values in Geant4 (A). The used sample detector setup in the simulation (B) [61].

The maximum value for the cutoff to be chosen should be equal half the detector's thickness to be simulated [41]. Decreasing the cutoff value further will result in the

simulation consuming CPU resources without a benefit to accuracy. A comparison between the default physics lists in Geant4 and the more accurate physics list and the step size of 100 µm tailored for YRM can be seen in Figure 1.21. The default physics model overestimates the energy deposition in the silicon detectors as opposed to the edited physics list, which yields a much more defined distribution of the energy deposition measurement in different silicon layers of the proton telescope. These new and improved simulation physics lists will play an important role in all the calculations in this thesis especially in section 2.3.1. These changes in simulation physics models are therefore incorporated in all following Geant4 simulations in this thesis.

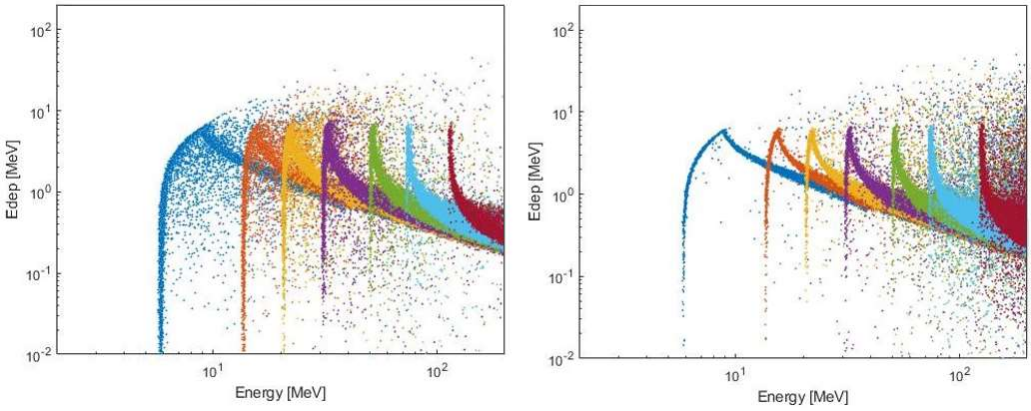


Figure 1.21 Energy deposition disribution in silicon detectors as a function of proton kinetic energy using edited physics (left) and using default physics (right) .

1.5.3 Implementing CAD Geometries into GEANT4

Designing geometries for Geant4 simulations is a tedious task. Each component must be broken into basic shapes and coded individually in C++. To circumvent this issue, the help of a GDML parser class is employed in the Geant4 source code [62], which allows for the import of GDML type files into the simulation. GDML files incorporate shapes as tessellated volumes of thousands of triangles and assigns a position, rotation and a material to each volume. To import the CAD geometry of

the telescope into Geant4 simulations, a conversion software is needed to transform the CAD files into tessellated shapes and assign materials to them.

There exists a plethora of such software on the internet, most of which require an expensive license for complicated shapes or simply are not stable enough for robust use. Thus, a custom designed conversion software was developed. Using FreeCAD libraries to do the tessellation process proved to be convenient, since the required functions are readily available and FreeCAD's libraries are open source. The code also utilizes parts of the code discussed in [63], namely the user interface and the writing to GDML functions. Other parts of the code were modified heavily to suit the needs of YRM. First, the code was ported from Python 2 to Python 3. Also, extra functionality for importing nested volumes was added, along with a new way to assign materials to the volumes in the GDML files.

The program receives a STEP file and reads its contents as shown in Figure 1.22. The individual parts are then shown in a "Volume List" on the user interface. From there, the user can choose the material of the volume from the G4NIST database. The user can also set the maximum tolerance for the volumes in the geometry. Once the options are chosen, the code will output one mother GDML file detailing the volumes and their position in the simulation world, in addition to a folder containing the data of each individual volume. The general structure of such a code was ported primarily from [63]. The output geometry files can then be imported into the user detector construction class of Geant4.

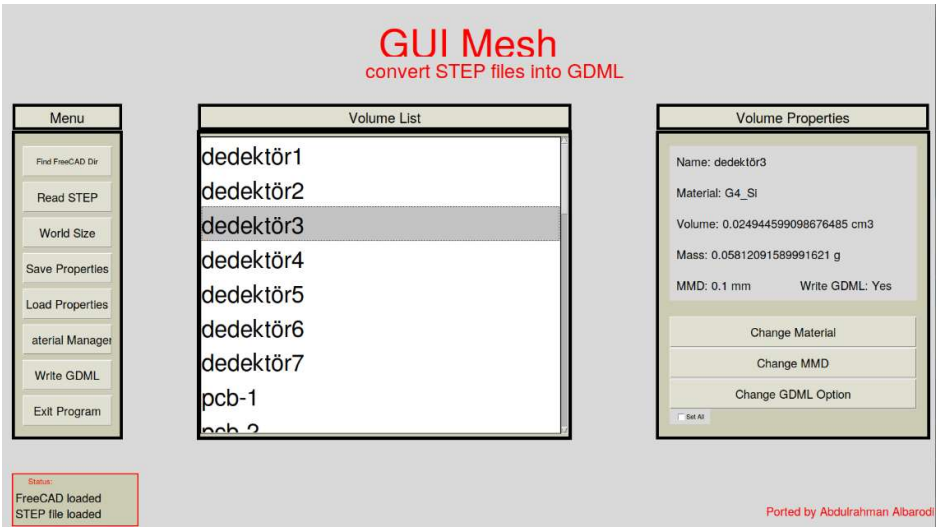


Figure 1.22 User interface of the program to import CAD files into Geant4.

1.5.4 Geant4 Incident Spectrum

Another issue in the Geant4 software became clear when simulating the proton spectrum incident on the detector in orbit. There are multiple ways to define energy spectrum of particle guns in Geant4 [64], many of which utilize some interpolation algorithm to feed randomized energy values between given points in the spectrum to the proton gun. However, when the given points are very far apart, interpolation algorithms readily available in Geant4 (linear, exponential, logarithmic) do not reproduce the input spectrum. For example, the differential proton spectrum from Figure 1.1 was input to Geant4 pointwise with exponential interpolation and the resulting spectrum using this method is given in Figure 1.23 for comparison. The interpolation output underestimates the decrease in the proton flux as the energy increases.

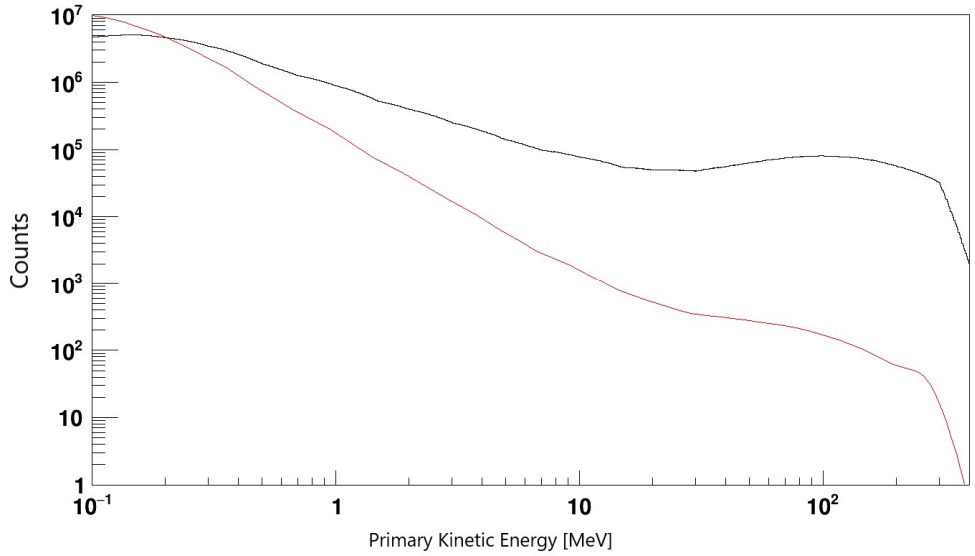


Figure 1.23 Primary proton spectrum generated by the Geant4 simulation using pointwise definition and exponential interpolation (Black), normalized SPENVIS trapped proton energy spectrum (Red).

Using a histogram input with no interpolation results in the spectrum seen in Figure 1.24, which agrees within an order of magnitude to the original input. However, it has the issue that higher end of each bin has an increased probability of generation. This lowers the precision of how well the simulation models the particle flux and was reported to the developers of Geant4 [42] without resolution as of writing this thesis.

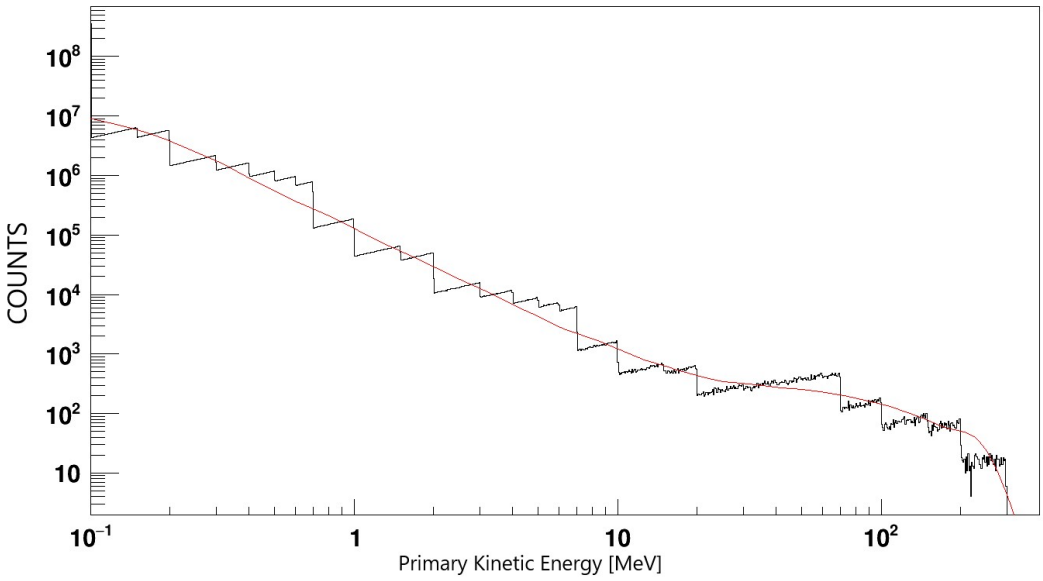


Figure 1.24 Primary proton spectrum generated by the Geant4 simulation using histogram definition (Black), normalized SPENVIS trapped proton energy spectrum (Red).

CHAPTER 2

YRM PROTON TELESCOPE DESIGN

2.1 General Description of YRM

Yerli Radyasyon Monitörü (Homegrown Radiation Monitor or YRM) is a radiation monitor project commissioned by the Presidency of Defense Industries of Turkey to be a part of its future satellite missions to LEO. The Space and Accelerator Technologies Research Center (IVME-R) is responsible for the design, prototyping and testing of YRM's components. The general aim of YRM is to measure the radiation environment in high inclination Low Earth Orbits. Thus, YRM incorporates two telescopes, a Proton/Heavy Ion telescope and an Electron Telescope. For the detector to capture the most significant and the widest possible range of the radiation spectrum, the proton measurement range is set to be between 2-200 MeV and the electron measurement range is between 100 keV – 7 MeV. The total weight of the device is limited at 1 kg and the volume at 1 L, to allow for ease of deployment on satellites. The power consumption goal is also set at 1 W.

With these limitations, the most effective contender for the detection of the particles is silicon detectors. The small size prohibits the use of calorimeters, time of flight detectors and magnets. PIN diodes are light and do not consume much power, they can resolve the energy of the incident particle efficiently. With no magnetic field, it is difficult to determine the charge of the ionizing radiation and the mass of the incident particle. High power ADCs cannot be employed due to the 1 W power consumption limit and the detector is unable to distinguish between different ions. However, the proton telescope will have the ability to differentiate between proton and heavy ion hits due to two different threshold settings. The general design parameters of the YRM proton and electron telescopes are summarized in Table 2.1.

Table 2.1 Design Parameters of the YRM proton and electron telescopes.

Parameter	Proton Telescope	Electron Telescope
Minimum Energy	2 MeV	100 keV
Maximum Energy	200 MeV	7 MeV
Number of bins	8	8
Maximum flux	10^7 particles/cm^2/s	10^8 particles/cm^2/s

The readout of the silicon detectors inside the telescopes is designed using a dedicated circuit for each detector. The design of the circuit must provide sufficient amplification and shaping of the signal so that it may be processed correctly. The signal, if it passes a high or a low threshold, is then fed to an FPGA (Field Programmable Gate Array) that is responsible for further coincidence and counting logic for the proton and electron telescopes. The FPGA is programmed with the necessary algorithms to provide accurate measurements of the radiation environment during the YRM mission lifetime.

2.2 Proton Telescope Working Principle

To satisfy the design requirements, the silicon detectors of the proton telescope must be able to resolve energies in the region between 2-200 MeV. This is implemented by setting two fixed thresholds on the signals after amplification and assigning particle hits into several bins depending the thresholds passed. The low threshold should have a high SNR (signal to noise ratio) to allow recording MIPs, while the high threshold should discriminate against the MIPs and record Bragg peak energy depositions. The coincidence logic combined with the thickness of the energy degraders between the PIN diode sandwiches will determine the energy from the range of protons inside the diode and degrader sandwiches.

2.3 Proton Telescope Design Procedure

2.3.1 Initial Design

The design criteria dictate 8 logarithmically equal energy bins for the proton telescope. After the calculation of the ranges of protons inside different candidates of degrader materials, the initial design can be summarized in Table 2.2. The telescope houses a total of 7 silicon detectors of thickness 0.52 mm. This thickness was chosen after consideration of the available silicon detectors in the Turkish market. A collaboration agreement with TÜBİTAK BİLGEM UEKAE YİTAL was signed to produce the silicon detectors. Each silicon detector was mounted on a 0.5 mm thick FR4 PCB. This also acts as an additional degrader for protons and heavy ions. The degraders were chosen as three Aluminum and four Tantalum layers to minimize the weight and the height of the telescope while avoiding materials that generate a lot of secondaries. The sandwich layout of the telescope inside the GEANT4 simulation can be seen in Figure 2.1. The layered design described in the table should achieve a logarithmic separation between the hits recorded by each detector. A beam of protons having energies from 1 MeV and up to 1 GeV is sent towards the telescope in a Geant4 simulation. The energy deposition in each detector is plotted against the primary energy of the protons. In Figure 2.2, the detectors start measuring the incoming protons at equal logarithmically spaced bins from 5 MeV and up to 200 MeV.

Table 2.2 Layers of the proton telescope's initial design and their thicknesses and diameters.

Layer name	Layer Thickness [mm]	Layer Diameter [mm]
Silicon Detector	0.52	10
PCBs	0.50	15
First Aluminum degrader	0.25	20
Second Aluminum degrader	0.15	10
Third Aluminum degrader	0.50	10
First Tantalum degrader	0.50	10
Second Tantalum degrader	1.50	10
Third Tantalum degrader	2.50	10
Fourth Tantalum degrader	6.00	10

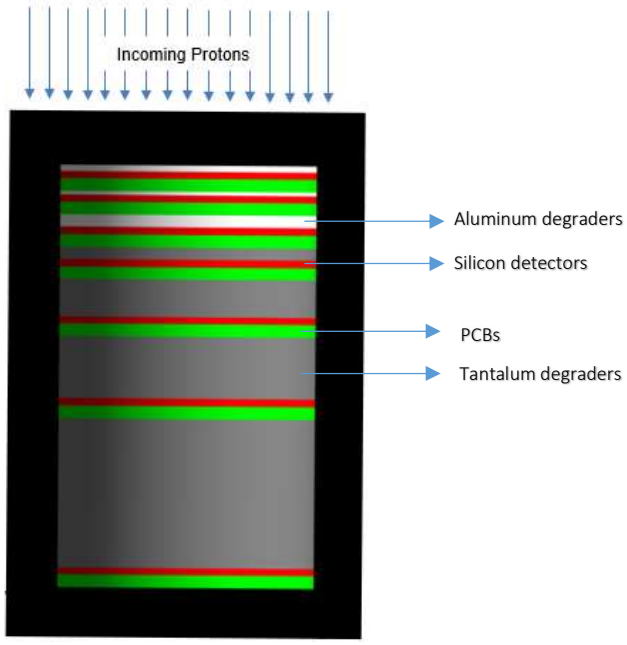


Figure 2.1 Proton telescope's initial geometry shown inside a Geant4 simulation visualization with direction of the incoming protons shown. Layers include Al degraders (white), Si detectors (red), PCBs (green) and Ta degraders (grey).

Layer #	Color	Minimum Recorded Energy
1	Blue	5.8 MeV
2	Red	13.7 MeV
3	Yellow	20.7 MeV
4	Purple	31.3 MeV
5	Green	49.2 MeV
6	Cyan	73.8 MeV
7	Magenta	114.0 MeV

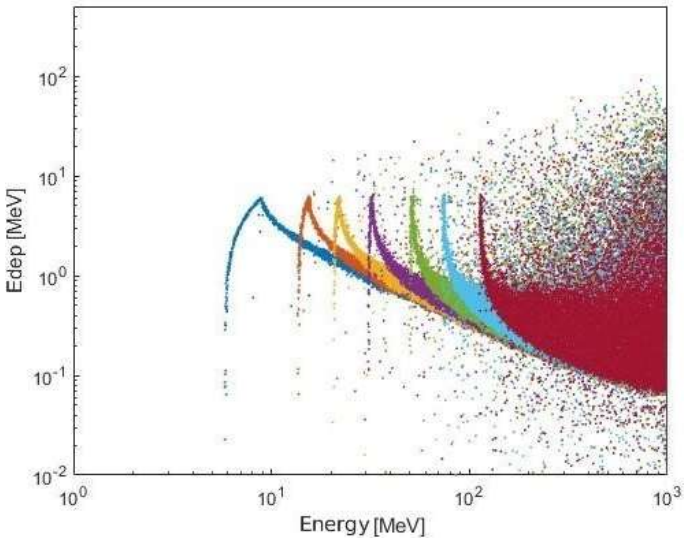


Figure 2.2 Energy deposition of protons in the silicon layers of the proton telescope as a function of primary kinetic energy in a Geant4 simulation in colors listed in the table.

Although the design criteria specified 2 MeV as the lowest sensitive bin for the proton telescope, that would require thinning the first aluminum degrader to 0.15 mm, at the expense of allowing some electron flux into the telescope, which would increase background from electrons and saturate the data acquisition.

The proton telescope must also be able to differentiate between proton and heavy ion hits. To achieve this, the energy deposition in consecutive detectors in coincidence must be investigated to form "physics channels". Heavier particles have a higher dE/dx and less range than protons at the same kinetic energy as a direct result of the Bethe-Bloch formula as discussed in Section 1.3. The energy depositions of O^{+8}, He^{+2} ions and protons with kinetic energies of 2-200 MeV/nucleon that passed through both of the first two silicon layers are presented in Figure 2.3. The energy deposition in the second detector is similar to the first detector if the particle has a

long range. It is larger at the end of its range where the particle makes a Bragg peak deposition, but it is smaller if the particle is past its R80 value.

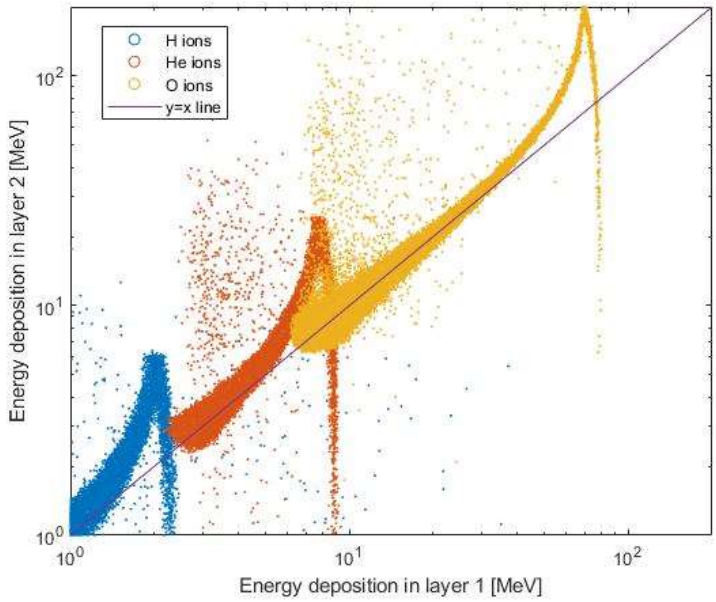


Figure 2.3 Energy deposition of O+8, He+2 ions and protons inside the first and second silicon layer. Protons are represented in red dots, alpha ions in yellow and oxygen ions in blue.

A low and a high threshold setting on each detector allows for a different coincidence logic to be performed inside the FPGA. The low threshold should be low enough to pass MIPs and charged particles beyond the R80 point, while the high one records the Bragg peak for protons and the MIP depositions from heavy ions.

The high threshold in the 7^{th} layer has been set to exclude hits in the 7^{th} detector that correspond to incident primary proton kinetic energies that are higher than 200 MeV. This allows for the creation of an 8^{th} bin that incorporates all recorded hits that do not deposit enough energy to cross the 7^{th} high threshold corresponding to all recordable particles above 200 MeV. Two comparators in the end of each readout electronics channel (one for each threshold) are responsible for the threshold discrimination, while a time window of 35 ns, determined by the signal width from the readout circuit, will be opened by the FPGA waiting for comparator outputs to

perform the coincidence logic. More details about the electronics can be found in Chapter 3.

The algorithm will use the logical values of the low threshold (LT) and high threshold (HT) comparator outputs to assign events to their respective physics channels or discard them. If the signal passes a threshold, it generates a logical True value if not, a False. Examples of such events are shown in Table 2.3. The algorithm will discard all events that do not have a LT True in the first detector, removing any events that might have penetrated the side shielding. The algorithm will ask for a coincidence of the LT and HT hits in order from 1 to 7 for a specific time window and if it encounters an LT False from any of the channels, it will stop the evaluation even if the following HT and LT values were True. Such events might be caused by an incoming particle scattering with high angle inside the detector and generating secondary particles or by accidental triggering of the thresholds by a separate energetic particle penetrating the shields. Once the algorithm encounters a False LT value, it will count how many detectors have their HTs triggered. If the number is equal to 1, then the proton energy channel bin corresponding to the last True HT value is incremented. If the number is larger, then the Heavy Ion energy channels counter corresponding the True HT value is incremented.

If no HTs are True in a given event, the event is discarded as a badly collimated particle (a high energy particle outside the acceptance of the telescope). However, if the particle manages to trigger all LT channels, but fails to trigger any HT channel, it is flagged as a passing MIP, thus the 8^{th} channel is incremented.

As high energy particles lose energy passing through the telescope, their dE/dx will also increase gradually and to have a high detection efficiency for each layer of the silicon detector, different thresholds can be set as shown in Section 2.3.2.

Table 2.3 Possible outcomes of the recording algorithm in different scenarios.

Layer #	Triggered Threshold					
	Case 1	Case 2	Case 3	Case 4	Case 5	Case 6
1	LT	LT	-	LT	LT	LT
2	LT	HT	LT	LT	LT	LT
3	HT	HT	HT	HT	LT	LT
4	-	-	-	-	LT	-
5	-	-	-	-	LT	-
6	-	-	-	LT	LT	-
7	-	-	-	LT	LT	-
RESULT	Proton event in 3rd channel	HI hit in 3rd bin	discarded	Proton hit in 3rd bin	Proton hit in 8th bin	discarded

2.3.2 Threshold Calculations

Low and high thresholds for the readout of the silicon detectors into physics channels were calculated using the dE/dx a stopping proton would deposit if it has enough kinetic energy to be recorded in the bin corresponding to a channel. Using the energy deposition obtained from Geant4 simulations, the energy deposition in each detector with respect to the initial proton energy were analyzed using the data shown in Figure 2.2. In Figure 2.4, the energy deposition of protons in consecutive silicon detectors are compared. The red line in the plot corresponds to $Edep_i = Edep_{i+1}$ line or where the energy deposition in consecutive detectors is the same. This plot shows the increased energy deposition in the i+1th detector compared to the ith detector.

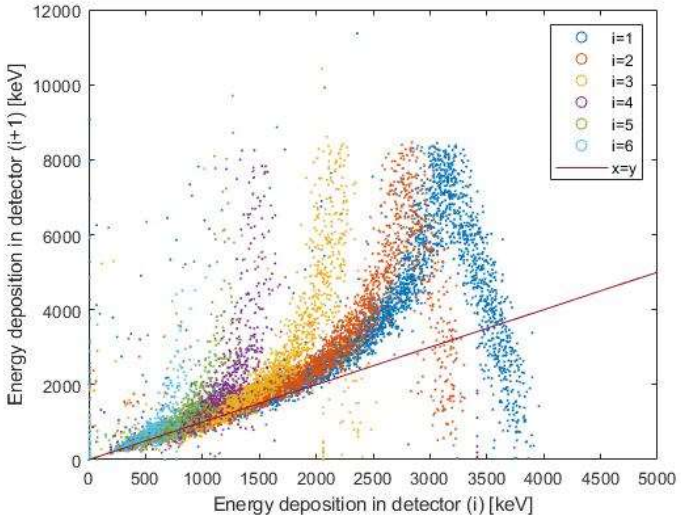


Figure 2.4 Energy deposition distribution of protons in consecutive silicon detectors.

A script to track the energy deposition of each proton and mark it with respect to where it stopped inside the proton telescope was written and the results are presented in Figure 2.5. The blue points correspond to particles that were not recorded in detectors past i+1, while red and others indicates particles that stop in later layers. A proton that reaches the 7^{th} layer deposit approximately the same energy in all the detectors before it, i.e., behave as minimum ionizing particles. A clear threshold can be set for each detector as indicated by the vertical line for the i^{th} layer and the horizontal line for the $i+1^{th}$ layer, which allows the particles also to be recorded by the next detector as summarized in Figure 2.5. The low threshold is set at 100 keV for all layers as it is suitable for rejecting electron signals and allows for the most amount of MIP protons to be recorded.

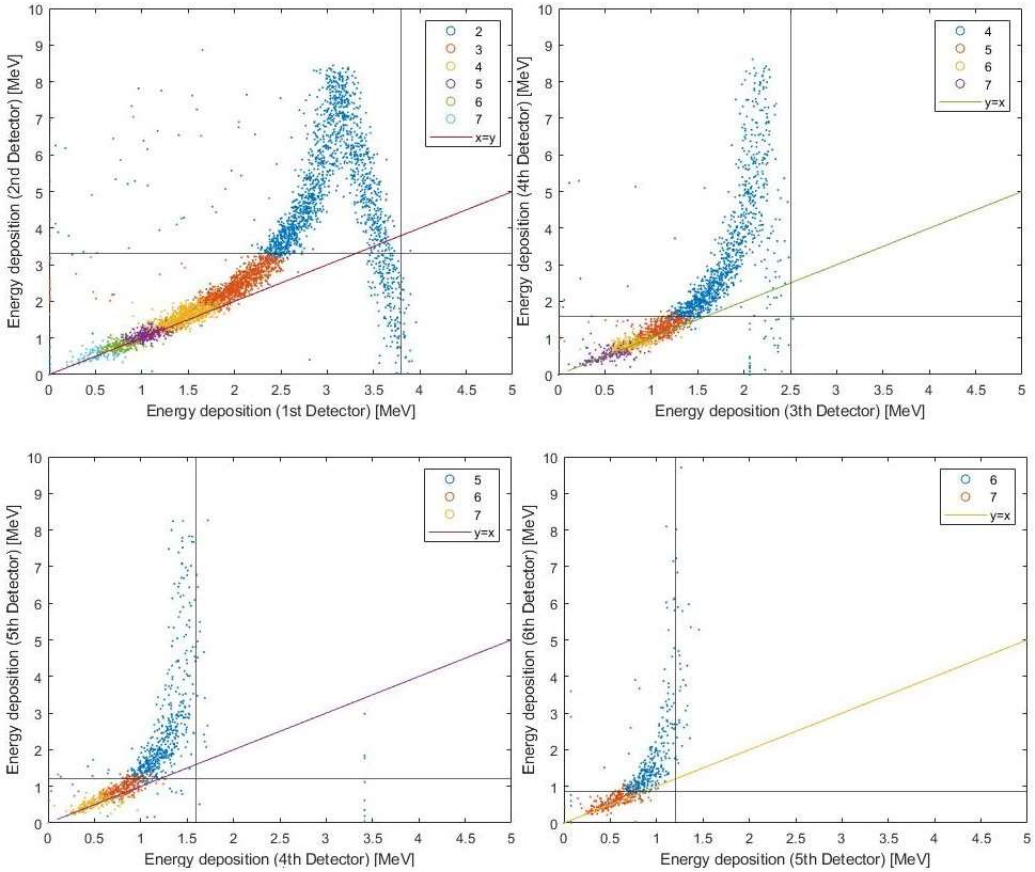


Figure 2.5 Energy deposition distribution of particles in pairs of consecutive detectors. Blue points indicate protons stopping at detector i+1; red points at i+2 and so on.

Table 2.4 The high energy thresholds for the proton telescope.

Detector	**High Thresholds [MeV]**
1	3.80
2	3.30
3	2.50
4	1.60
5	1.20
6	0.85
7	0.50

2.3.3 Shielding and Collimation

After verification of the working principle of the detector, the shielding of the detector/degrader setup comes next. Details and iterations on the exact design are discussed thoroughly in section 2.3.4. Two layers of shielding are common in all designs: an internal copper shield to against energetic gamma rays and an outside aluminum shield that is light weight and serves to stop particles (electrons and low/medium energy protons) that correspond to 99% of the radiation environment in LEO [65]. Thus, ensuring that particles that come in the acceptance angle defined by the collimator allows for an accurate calculation of flux using Geofactors. A technical drawing of the telescope is shown in Figure 2.6 along with accepted and rejected particles.

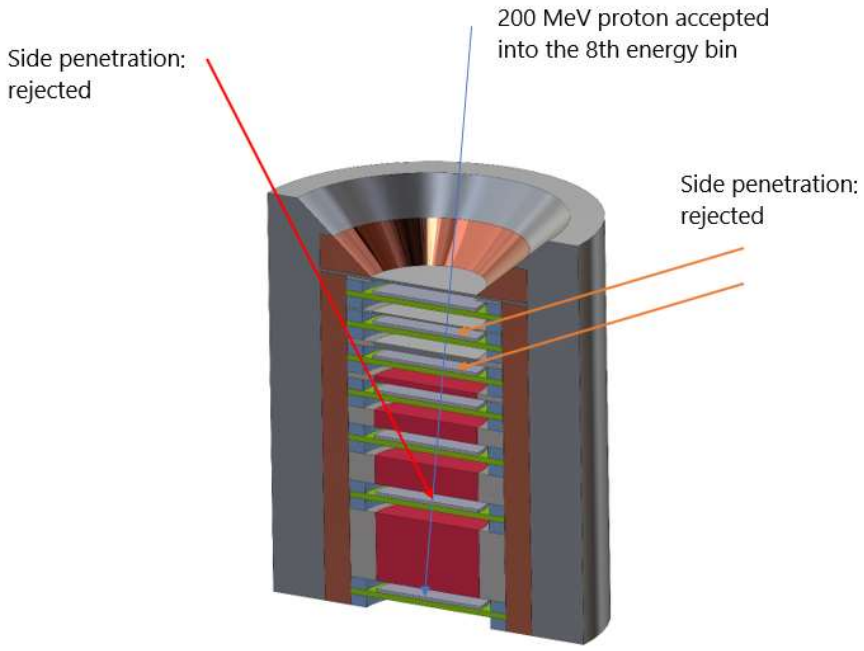


Figure 2.6 The general design and working principle of the proton telescope. Arrows represent incoming protons. Particles indicated with a blue arrow is accepted while the particles shown in red and orange are rejected as outside of acceptance.

2.3.4 Design Alternatives

Multiple design alternatives for the YRM proton telescope have been investigated in the process of writing this thesis. Different designs encompass different criteria and employ different strategies to achieve the best and most feasible proton spectrum measurement. Two of these designs will be discussed thoroughly and compared in the following sections.

The first of the design alternatives is the single sized detector design. Seven identical silicon detectors are placed in an aluminum column with energy degraders in between. The detectors are held in place with their PCBs using a polymer holder, whose purpose is to absorb shocks from the launch and to limit the effect of backscattering by employing a carbon rich material on the backside of the detector. The telescope has double layer shielding of copper and aluminum to increase the shielding efficiency without increasing the weight and beyond the design criteria.

An alternative design was suggested to increase the energy resolution of the telescope and reduce the effect of badly collimated incoming particles. Giving the telescope a conical angle, which increases detector size with increasing depth, achieves both of these goals with the added benefit of extra statistics gathered from the higher area detectors at higher energies, with the caveat of mis-identification of heavy ions.

The detectors of this design are also silicon circular detectors. However, they have varying sizes. The limiting factor to the size of these detectors is imposed by the manufacturing process. TÜBİTAK BİLGEM UEKAE YİTAL is the prospective manufacturer of these detectors and they have specified their production size limit as 2 cm per detector. Thus, in the design procedure the limit is 18 mm circles in diameter, putting 2 mm as a safety margin to avoid non-uniformities in the manufacturing process. Holders for the PCBs and detectors are not included in this design since it was still in early stages.

Since both designs are aiming to measure the flux in the same energy regime, and since the penetration depth of the incoming protons is the same, the thicknesses of the energy degraders are not changed. However, particles that do not have a normal incidence have to cross a higher thickness of material which creates the problem of misidentification. For the detectors, the signal coming from an energetic particle that has a high incidence angle is indiscernible from a heavy ion that has normal incidence. The angle reduces the effect of the critical angle at which the incoming protons start to deposit enough energy to cross the higher threshold, thus resulting in misidentification. The presented conical design has a higher acceptance angle than all other designs investigated for this thesis throughout this process. The effect this has on the quality of the energy spectrum measurement will also be investigated.

To check the feasibility of recording particles beyond the 200 MeV range with a higher resolution, an extension to the angled design was suggested and tested as part of the optimization process. To continue the logarithmic progression of the bins, a very large amount of metal must be used as for the energy degraders, thus increasing the weight of the telescope by a factor of two. Thus, only a very limited number of bins can be added with only a minor increase in statistics observed throughout the device's lifetime.

These three designs were subjected to simulations to measure their response to different spectrums of radiation. The trapped proton and electron spectra in LEO were sent to each suggested design along with the worst solar proton spectrum. The effect of the galactic cosmic protons and heavy ions was also investigated. The parameters of these three designs are summarized in Table 2.5.

The pros and the cons of each of these designs will be discussed and compared based on acceptance [2.3.5], background [2.3.6,2.3.9] and reconstruction [2.3.7, 2.3.9]in the following sections.

Table 2.5 The Design Parameters of the Different Proton Telescope Geometries

Design	Acceptance angle [degrees]	Total length [mm]	Total mass [g]	Number of bins	Number of detectors	Variable detector area
Single Sized	0	25	300	8	7	No
Conical Design	18	20	300	8	7	Yes
Extended Conical Design	11	66	500	10	9	Yes

2.3.5 Telescope Acceptance Calculations

The aim of the Geofactor and acceptance curves is to check if each of the proton energy channels is recording hits only in its specific energy regime. And thus, the telescope can resolve each energy bin separately. Achieving this is the most important design milestone for YRM. Using a Geant4 simulation, the acceptance curve for the ideal situation where truth is known about the particle trajectory and discrimination against particles penetrating the shields can be performed with perfect accuracy, is shown in Figure 2.7. This plot represents the best and unrealistic scenario from the proton telescope. The channels start recording exactly at the desired energy and stop exactly when the next channel starts recording. This is true for all detectors except for the first one since it is exposed to the most isotropic distribution of incident particles.

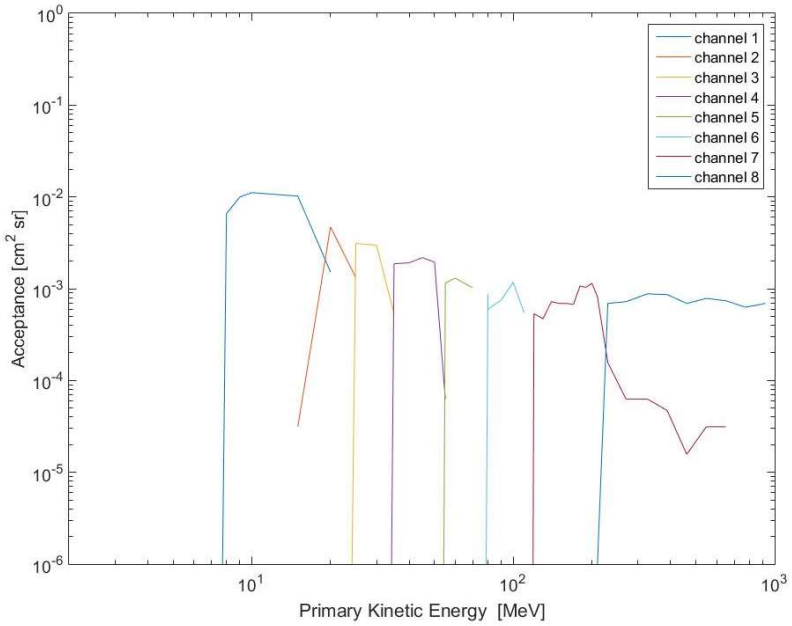


Figure 2.7 Ideal acceptance curve of the proton telescope for protons in a Geant4 simulation.

If truth is not known about these hits and rejection against them therefore cannot be performed, the acceptance of the telescope to hits that penetrate the side shielding is as high as the desired acceptance of the channels up to ~30 MeV then falling sharply, since the telescope's coincidence criteria for high energy channels is more scrutinous than low energy channels. The telescope's acceptance to these hits is shown in Figure 2.8.

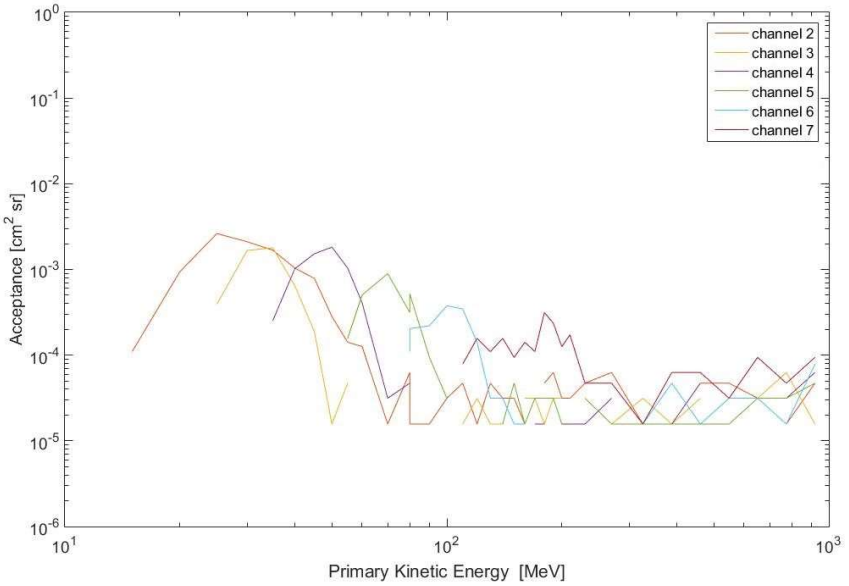


Figure 2.8 Undesired acceptance of the proton telescope hits from the side penetrating hits in a Geant4 simulation.

To avoid triggering on these events, the feasibility of adding an anti-coincidence detector to the sides of the telescope that is vertically transverse to rest of the detectors is investigated. However, upon simulation of such design, only minor improvement is observed. In the realistic case, a perfect anti-coincidence discrimination against side penetrating particles cannot be applied because of particle scattering.

The coincidence algorithm alongside energy thresholds and the collimator design of the conical geometry results in the acceptance curve shown in Figure 2.9. The first channel keeps recording evets even at very high energies with a significant probability. Other channels exhibit this behavior as well but not to the same extent. Thus, the need for some event redistribution algorithm arises.

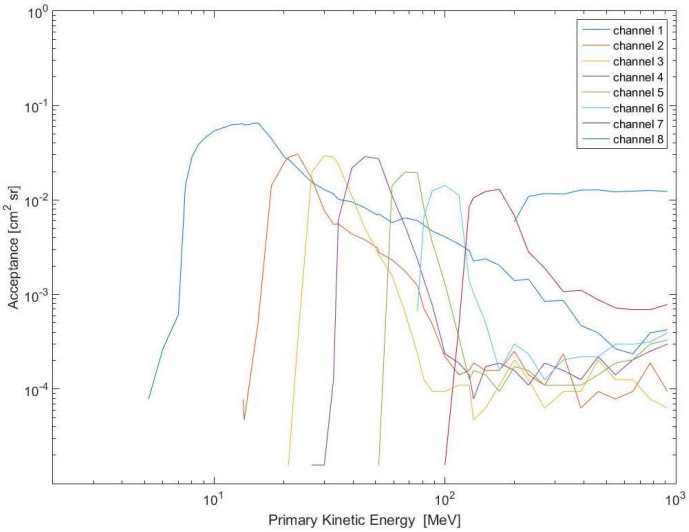


Figure 2.9 The Acceptance curve of the conical design of the proton telescope in a Geant4 simulation.

The single sized design performs inferiorly to the conical design in this aspect as shown in Figure 2.10. Since the conical design accepts particles at higher angles than the single sized design, the increase in acceptance at the wrong channels that the single sized telescope is exhibiting can be avoided.

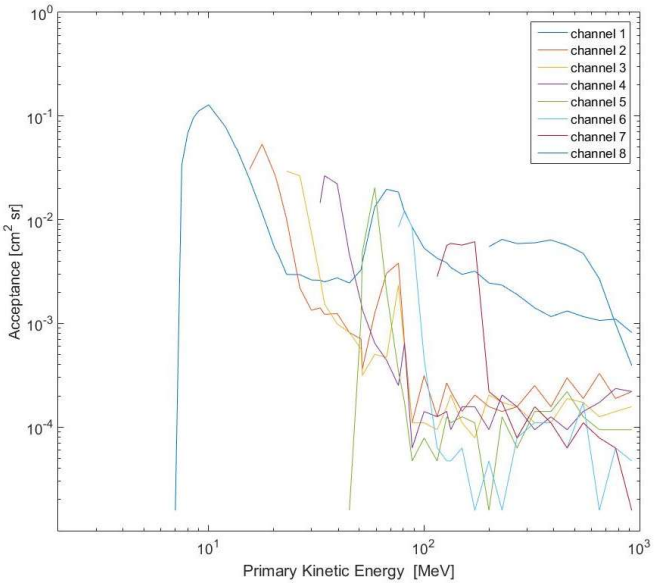


Figure 2.10 The Acceptance curve of the single sized design of the proton telescope in a Geant4 simulation.

The effect this difference in acceptance has on the quality of the measurement is shown in Section 2.3.9. For heavy ions, the telescope acceptance can be shown for each ion species individually. An example of the acceptance to alpha particles is shown in Figure 2.11. Alpha particles with increasing energy are being recorded in heavy-ion channels with good separation between the energy bins. However, since information about the ion species cannot be obtained, it is not feasible to designate energy values to the events as the channels will behave differently for each ion species.

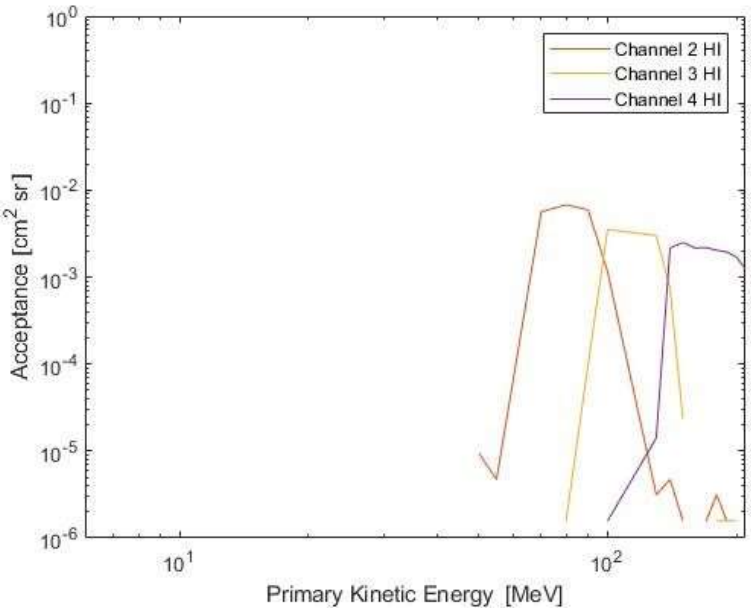


Figure 2.11 Acceptance curve of the proton telescope heavy-ion channels to alpha particle irradiation in Geant4 simulation.

2.3.6 Background Rejection

The investigation of the proton telescope's response to backgrounds is important to assess its performance. The response of the detector and the algorithm to primary electrons has been simulated using the same method as protons. The results are

shown in the Figure 2.12. As is the design objective, the shielding of the detectors and the lower thresholds protect the telescope from the electron radiation background since the vast majority of electrons in LEO have dE/dx values too low to pass the low threshold. Only a very small percentage of the electrons are recorded in the last channel with high primary electron energies. The rest of the channels were never triggered in the simulation.

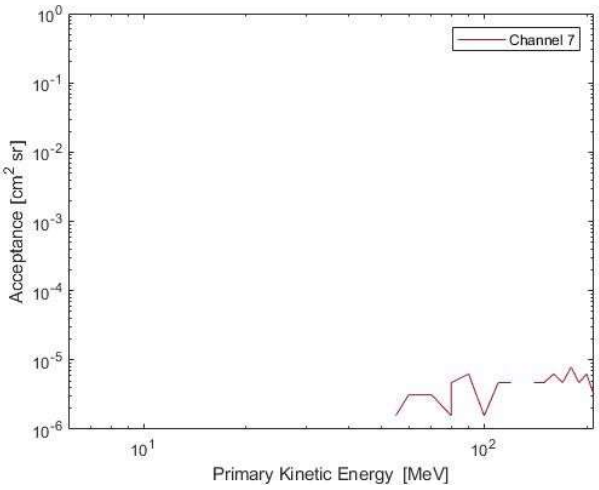


Figure 2.12 Acceptance of the proton telescope to primary electron radiation in Geant4 simulation. Only non-zero channel is at the seventh channel with very high energy electrons.

The electron telescope will be able to provide data about the electron spectrum and flux in the environment and can be used to clean up any background that could be caused in the proton telescope.

The background resulting from the heavy-ion irradiation in the proton channels is insignificant except for the first detector since the first detector since the algorithm relies on the data from two consecutive detectors to determine whether the particle is heavy ion or not. Thus, the first detector has no way of distinguishing heavy ions from protons. On the other hand, heavy-ion (HI) channels also have a probability of erroneously triggering under proton irradiation. Such probabilities of each HI

channel have been calculated via simulations and the results are shown in Figure 2.13.

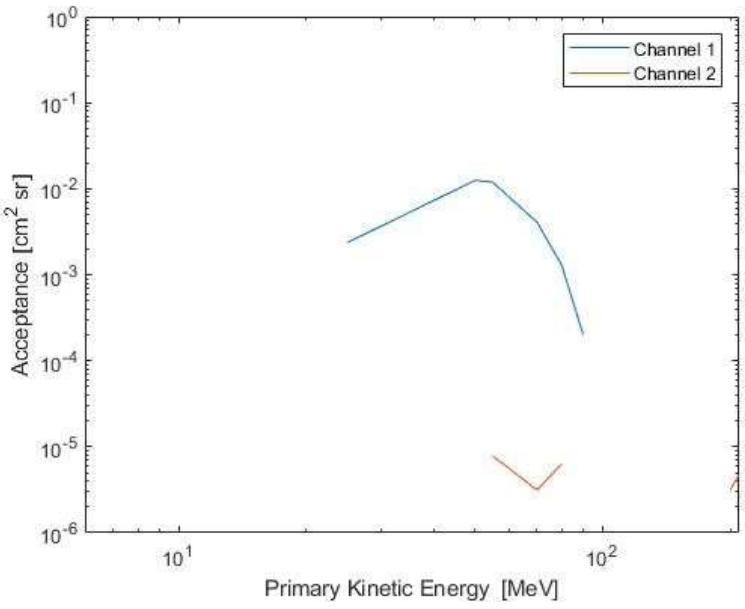


Figure 2.13 Helium background contribution to the proton telescope acceptance for proton channels in Geant4 simulations.

.

2.3.7 Bin-to-Bin Migration and Spectrum Reconstruction

The reassignment of the counts from the coincidence channels to measured counts of particles in a specific energy bin is the last step to obtain the measured energy spectrum of the protons. To achieve this task, migration matrices are employed. Since the value of the acceptance correspond to the probability that a particle coming in from a surrounding sphere with an isotropic angular distribution will result in an event being recorded in the counter of the energy bin, it should be considered as the determining factor of the energy of a recorded event. The acceptance curve is divided into 8 regions corresponding to the 7 logarithmically equal energy bins with the 8th bin extending up to 1 GeV as shown in Figure 2.14.

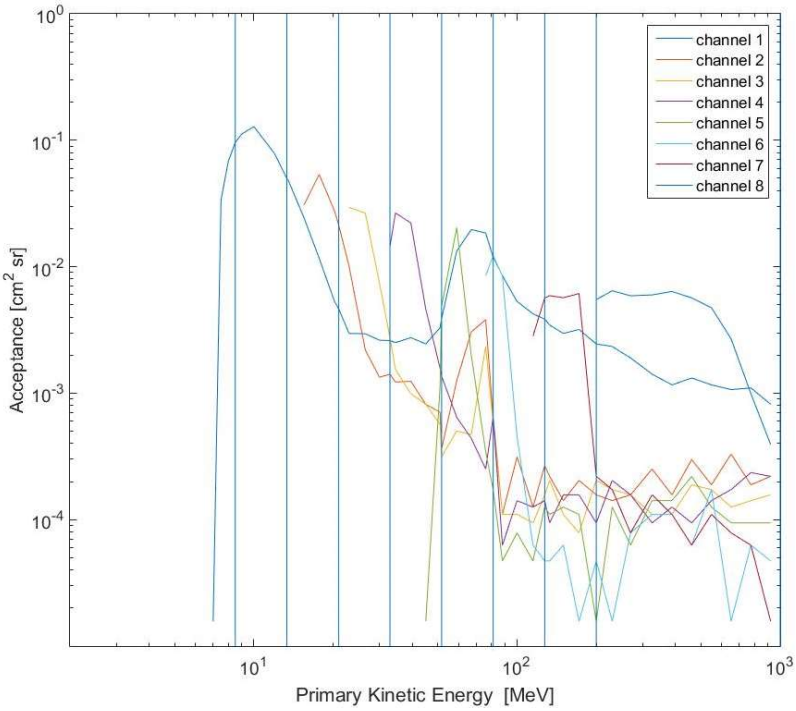


Figure 2.14 Acceptance curve of the proton telescope single sized design, divided into 8 energy regions for calculation of reconstruction algorithm parameters.

It is important to note that the probability of the telescope recording an event from a particle with an incident energy that is outside its respective energy regime is non-zero, which means that some events are being recorded into the wrong energy bins. The average amount of these falsely allocated events can be calculated from the acceptance curve. By calculating the area under the acceptance curve for a specific channel and finding the ratio of the area contained inside one bin to the total area, the average mixing of each channel with respect to the other can be found. For each design, these ratios are gathered in a bin-to-bin migration matrix $\underline{\underline{A}}$. The matrix has the structure:

$$A_{ij} = \frac{P_{ij}}{I_i} \tag{2.1}$$

where I_i : $total\ area\ under\ the\ curve\ for\ channel\ i$

and P_{ij} : $area\ under\ the\ curve\ for\ channel\ i\ in\ bin\ j$

The rows of $\underline{\underline{A}}$ must have a sum close to 1 to preserve the total number of counts inside the measurement energy region. The reconstruction algorithm makes use of the migration matrix by using the matrix elements in the following formula:

$$(new\ bin)_i = N_i * \sum_{i=1,j=1}^{7} bin_i * A_{ij} \tag{2.2}$$

where N_i is the normalization factor for the specific bin including area, exposure time and other simulation parameters. An example of such a matrix is shown below for the single sized design telescope geometry.

$$A = \begin{bmatrix} 0.177 & 0.055 & 0.013 & 0.020 & 0.169 & 0.105 & 0.084 & 0.348 \\ 0 & 0.425 & 0.109 & 0.033 & 0.113 & 0.019 & 0.023 & 0.278 \\ 0 & 0 & 0.543 & 0.052 & 0.073 & 0.018 & 0.026 & 0.289 \\ 0 & 0 & 0.050 & 0.588 & 0.041 & 0.017 & 0.023 & 0.281 \\ 0 & 0 & 0 & 0.019 & 0.657 & 0.012 & 0.024 & 0.289 \\ 0 & 0 & 0 & 0 & 0.329 & 0.465 & 0.011 & 0.195 \\ 0 & 0 & 0 & 0 & 0 & 0.151 & 0.718 & 0.131 \\ 0 & 0 & 0 & 0 & 0 & 0 & 0.027 & 0.973 \end{bmatrix}$$

It should be noted that this method automatically assumes that the incidence probabilities for all energies that the telescope is sensitive to is equal. This means that this algorithm works best for measuring uniform energy spectra and is worst performing at mono-energetic spectra. Thus, incident energy spectrums that have sharp changes will be difficult to resolve. Calibration of the telescope using particle beams is therefore necessary for the telescope to achieve better accuracy. Machine learning algorithms could also be used in the future along with Geant4 simulations to simulate the telescope's response for different primary spectra and generate an algorithm to accurately reconstruct the primary energy spectrum.

Results of applying this method to the counts in each detector channels and the reconstructed spectrum along with the misidentification probabilities are presented in section 2.3.9.

2.3.8 Effect of Incidence Angles

To find the optimal geometry with the flattest and highest acceptance with the lowest background, different acceptance angles of the detector are tried. The acceptance angle of a telescope is defined as θ, the algorithm described in Section 2.3.1 is reviewed such that particles having angles higher than θ will only trigger the low threshold in each detector as they pass by, and will not deposit the bulk of their energies until they stop at the inner surface of the side shield. The algorithm will recognize such particles as badly collimated. This is scenario is illustrated in Figure 2.15.

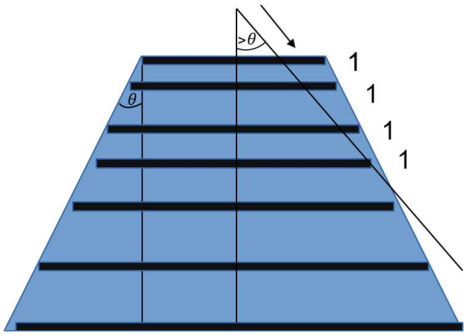


Figure 2.15 Normal operation scenario for a high incidence angle particle incoming at the proton telescope.

However, there are two cases where this algorithm fails to make the correct discrimination. The first of which is when the particle is angled at an angle so sharp that it travels significantly more distance in the telescope's material compared to particles with normal incidence. Thus, the particle can deposit enough energy to trigger the high threshold and be counted as a valid signal. Such a scenario is illustrated in Figure 2.16.

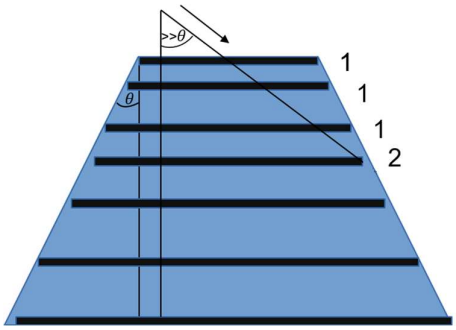


Figure 2.16 The first scenario by which particles with high incidence angles can cause faulty measurements

Such events have a rate that is dependent on the quality of the collimator on top of the 1st detector. For such a collimator can block these particles from going in with such high angles. The angle at which the high threshold gets triggered by a particle that is supposed to trigger the next detector instead (if having perpendicular incidence) is defined as $\alpha_{CRITICAL}$. This angle is itself independent of the acceptance angle θ and is different for each detector. This angle is decreasing as the detector number increases, since the distance travelled inside the telescope material changes according to the dependence below:

$$Distance = \frac{Depth\ inside\ the\ detector}{Cos(\alpha)} \tag{2.3}$$

where α is the incidence angle of the incoming particle. For the condition that $\alpha > \alpha_{CRITICAL}$, an errneous signal of the first kind will occur. Thus, if θ is larger than $\alpha_{CRITICAL}$, This means that the telescope actively allows for this effect to occur uninterruptedly, thus making sure θ is below a certain limit is of utmost importance. This effect can also be limited by efficiently collimating incoming particles and forbidding any high α particles from entering the enclosure.

The second effect occurs when α for a proton or heavy ion is slightly higher than θ and below a certain Δθ such that $\alpha_{CRITICAL} > \alpha = \theta + \Delta\theta$ that allows for the particle to actually actuate the last detector it sees without being hindered by the collimator on the top of the telescope, while being terminated before depositing the last of its

energy. such effect is prominent at the sides of the detector where the particle flight path is abruptly terminated as demonstrated in Figure 2.17.

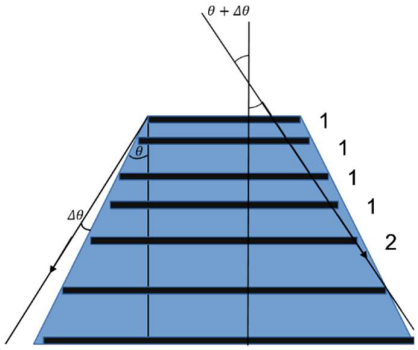


Figure 2.17 The first scenario by which particles with high incidence angles can cause faulty measurements

The rate of such effect is dependent on the ratio $\frac{\Delta\theta}{\theta}$, and thus increasing θ will intern decrease the occurrence of this effect. Another way to decrease the error caused by this is to increase the area of the detectors. Consequently, the contribution from the sides will be less significant to the bulk of the detector since the area increases as a function of r^2 while the circumference increases by as a function of r.

At the event of such a particle hitting the telescope not close to the sides, a proton will be misidentified as a heavy ion, this is intrinsic to all θ values since distinguishing between an angled proton or a normally incident heavy ion without spatial resolution in the detectors is not possible. This is illustrated in Figure 2.18.

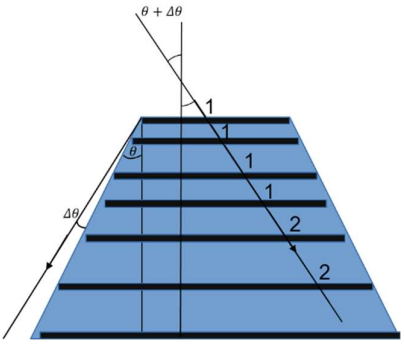


Figure 2.18 Scenario by which misidentification in Heavy-Ion channels occur.

These unfortunate sources of error have to be weighed against the gained increases in resolution observed in simulations and reconstruction results in 2.3.9. An investigation of the most appropriate θ value was done by trial and error. The θ value for conical design was found to be the most suitable for YRM's purposes.

2.3.9 Simulation Results

2.3.9.1 Single Sized Design

The first test was to test to subject the old geometry to trapped proton radiation in LEO environment. Such a spectrum was imported from SPENVIS as shown in section 1.1.1. All the simulations in this section have been done with 10^9 primary particles, so all spectrums had to be scaled accordingly. To check the validity of the sent spectrum and the normalization procedure. The normalized histogram of the sent particles inside the simulation is compared with the raw data from SPENVIS. The histogram was cut at energies below 2 MeV since the telescope is not sensitive to them, in order to reduce the number of particles that need to be generated in order to reach statistically significant hits in the telescope. In Figure 2.19, good agreement can be seen between the simulation histogram and the theoretical data. The Geant4 spectrum was cut at 2 MeV since protons below that energy do not make it past the first degrader, thus increasing the simulation statistics with lower computation time.

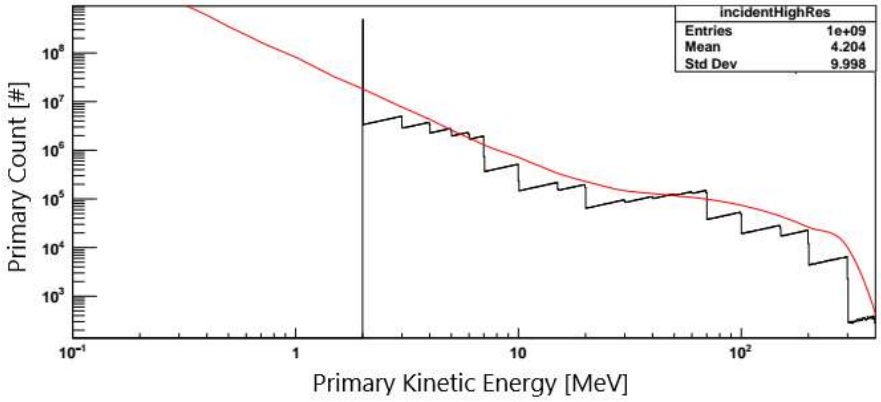


Figure 2.19 Primary protons energy spectrum in Geant4 (black), normalized SPENVIS trapped proton energy spectrum (red). Geant4 histogram is cut at 2 MeV.

Primary protons with this energy distribution were shot isotopically from a dome on the upper side of the telescope in the simulation. A solid cube of aluminum was put under the telescope to simulate the bulk material the telescope is going to be mounted to, which is important for analysis of backscattering effects.

The resulting counts in the detectors are shown in Figure 2.20 along with a comparison on with the incident spectrum. The values are almost an order of magnitude out of agreement especially at high energies.

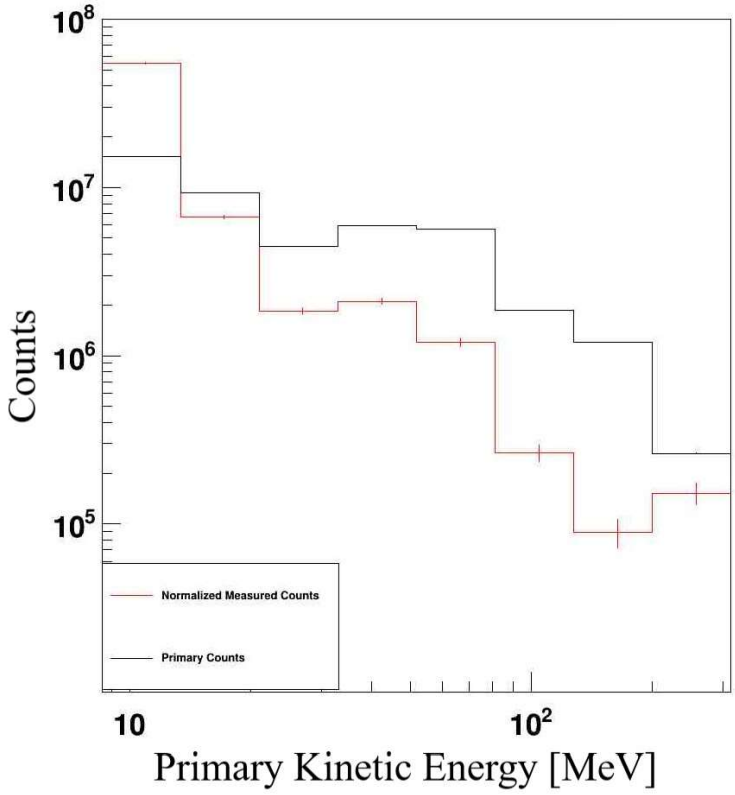


Figure 2.20 The resulting counts in the energy bins of the proton telescope single sized design compared with the primary particle counts in the Geant4 simulation.

To check the integrity of these results, the sensitivity of the telescope to the incident energies is investigated. i.e., the recording probability of a proton by the telescope versus the proton's primary kinetic energy. Such a measurement is called the "sensitivity" of the telescope to a certain energy. The result can be seen in Figure 2.21. This plot shows clearly the disparity between the particles that reach the telescope and what the telescope is sensitive to. Such result is indication that the fault lies within the actual resolving power of the detector and its physical layout instead of the scoring algorithm or the reconstruction logic. Thus, this is considered as a primary measure of the quality of the detector.

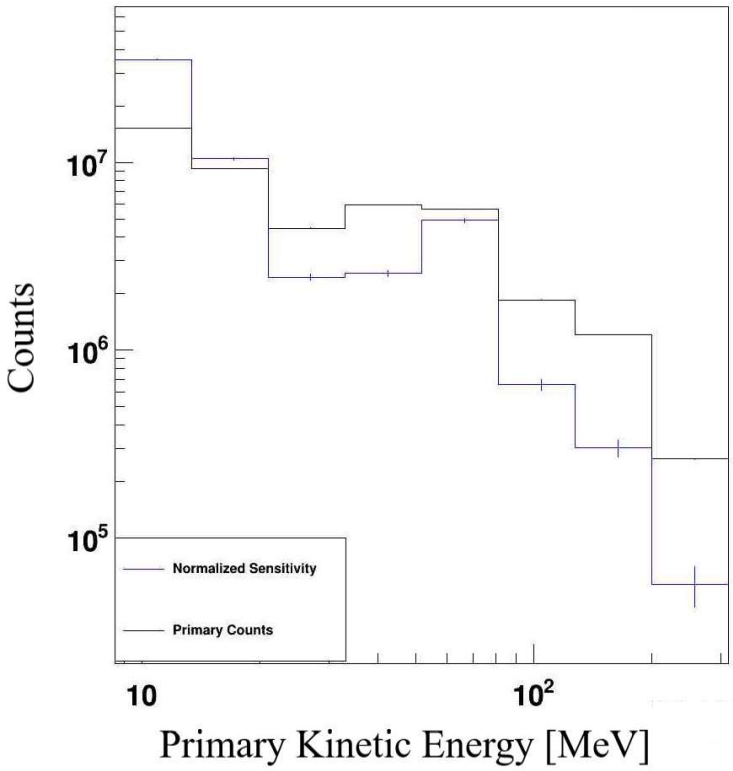


Figure 2.21 The sensitivity of proton telescope energy bins compared to the incident primary proton energy spectrum in Geant4 simulation.

Naturally, applying the reconstruction algorithm to this data will yield erroneous results. However, it is important to report that out of the almost 20,000 events collected by this detector, only 17 were mis-identified to be heavy ions.

The performance of this telescope under the solar proton spectrum in LEO at the solar maximum was investigated since it is the most dominant mode of radiation during the lifetime satellites in LEO orbits. The spectrum in Geant4 simulations were inputted from SPENVIS as shown in Section 1.1.2. Under this irradiation, the telescope remarkably recorded no events in the Heavy ion channels, although that can be attributed to the spectrum having exceedingly high concentrations of low energy protons at the cost of higher energy protons. It can be seen from Figure 2.22 that only a few particles had energies above 200 MeV and a few hundred particles above 100 MeV.

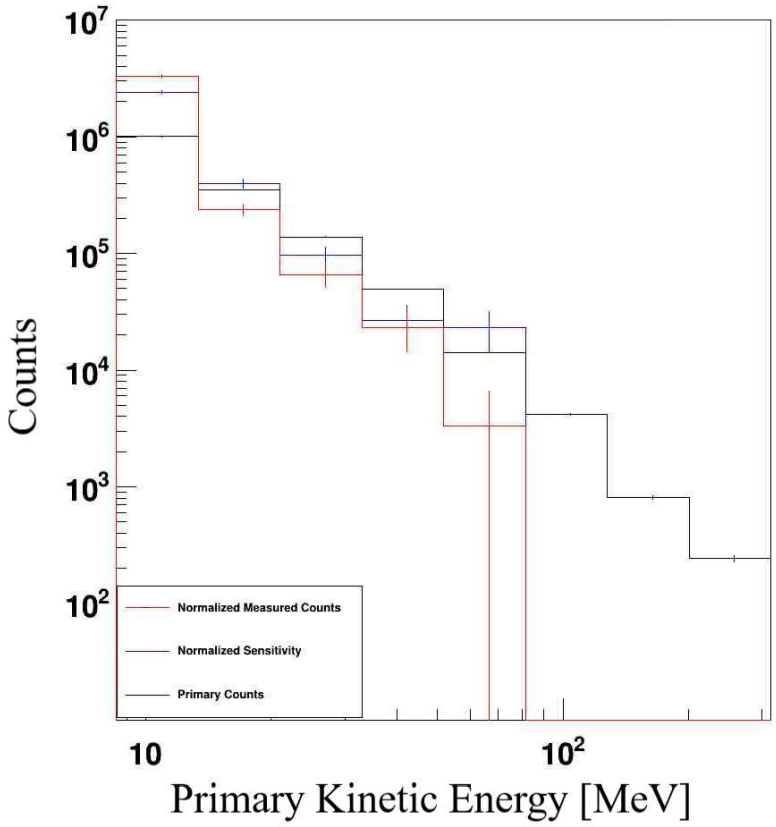


Figure 2.22 The sensitivity of the energy channels to primary solar protons and the counts in the telescope energy channels compared to the primary solar proton spectrum.

In the case of solar radiation, the telescope maintains acceptable results indicating its suitability to work in environments solemnly dominated by solar protons. The reason for which is that the spectrum in this case is highly shifted towards low energies, making it easier to resolve.

To simulate the effects of heavy ions on this detector, the cosmic heavy ion spectrum of alpha particles from the SPENVIS data base at LEO orbits is sent to it. This spectrum starts from energies at 1 MeV and goes up to the GeV scale. This gives a good look on different effects heavy ion signals might have on the telescope. As in the previous cases, the primary energy spectrum was scaled for 10^9 primaries in the simulation.

The response of this telescope to heavy ions can be seen in Figure 2.23. The proton channels were triggered about two-fold more than the heavy ion channels. With no relationship to be observed between the incident spectrum and the counts in either types of channels, these results can be regarded as significant contamination of heavy ions in the proton channels. It can be seen where the ions begin to penetrate the sides of the detector at the fourth proton bin resulting in an increased count.

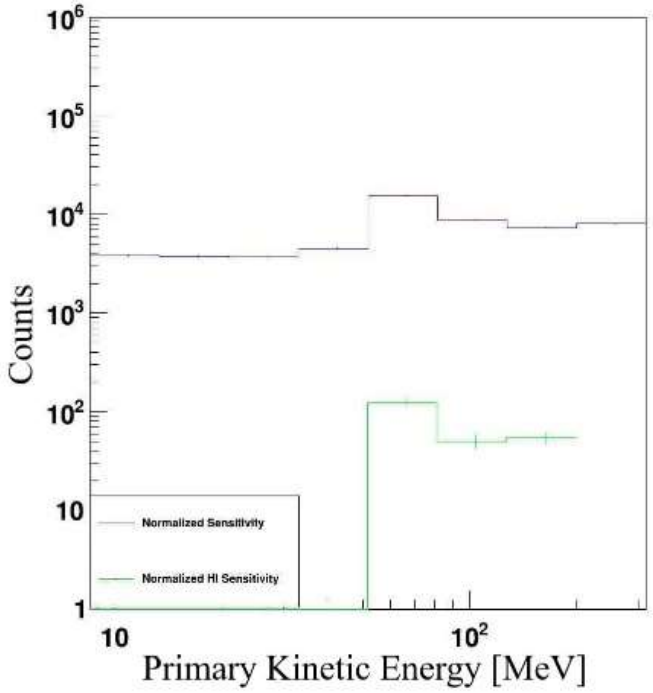


Figure 2.23 The sensitivity of detector proton channels and Heavy Ion channels against GCR alpha particles.

In the case of high energy protons coming from cosmic rays (up-to 100 GeV), the incoming spectrum is very similar to the cosmic alpha spectrum. The sensitivity plots in Figure 2.24 show that the particles recorded in proton channels have energies higher than 20 MeV and 50 MeV for Heavy ions, with the sensitivity of heavy ion channels mimicking that of the incident spectrum. Thus, creating a very chaotic signal in both heavy ion and proton channels. From this result, and since no

proportionality can be observed in the spectrum, no obvious contamination removal strategy is available to employ at this stage.

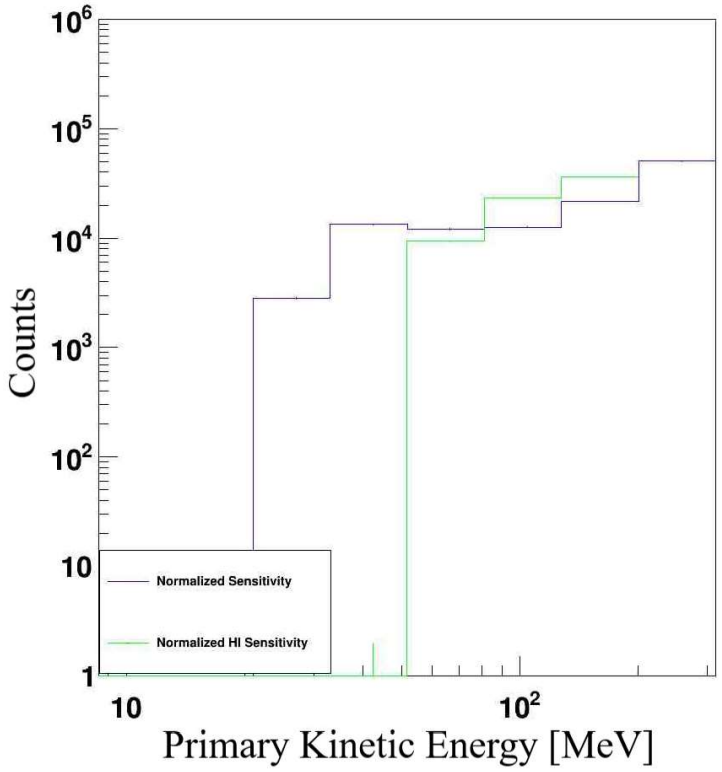


Figure 2.24 The sensitivity of detector proton channels (left) and Heavy Ion channels (right) against GCR protons.

The results of all tests done for the single sized detector design geometry are summarized in Table 2.6.

Table 2.6 Summary of simulation results of the single sized design.

Particle	**Inside design measurement energy region**	**Outside design measurement energy region**	**Contamination to other channels**
Electrons	No sensitivity	Can be removed (Electron Telescope)	Not significant
Protons	Good sensitivity Bad reconstruction	Can be removed	Not significant
Heavy ions	Bad sensitivity	Very high, can be removed	Very high, no obvious removal strategy

2.3.9.2 Conical Geometry

This design underwent the same tests as the single sized design. First, its response under trapped proton radiation in LEO was investigated. The normalized counts of the channels are shown in the plots in Figure 2.25. Significant improvement can be observed in the aspect that the counts are within the same order of magnitude as the primary spectrum. That is due to the sensitivity curve being in good agreement with the primary spectrum as shown in Figure 2.26. This points to the superiority of this design to its predecessor in terms of resolving power.

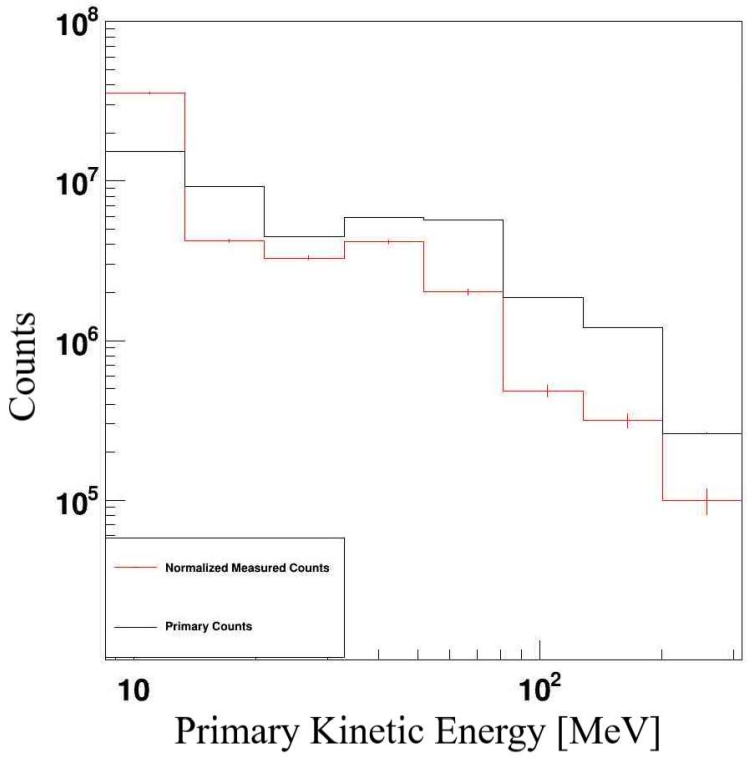


Figure 2.25 The measured and normalized counts of the proton telescope inside the Geant4 simulation compared to the incident primary proton energy spectrum.

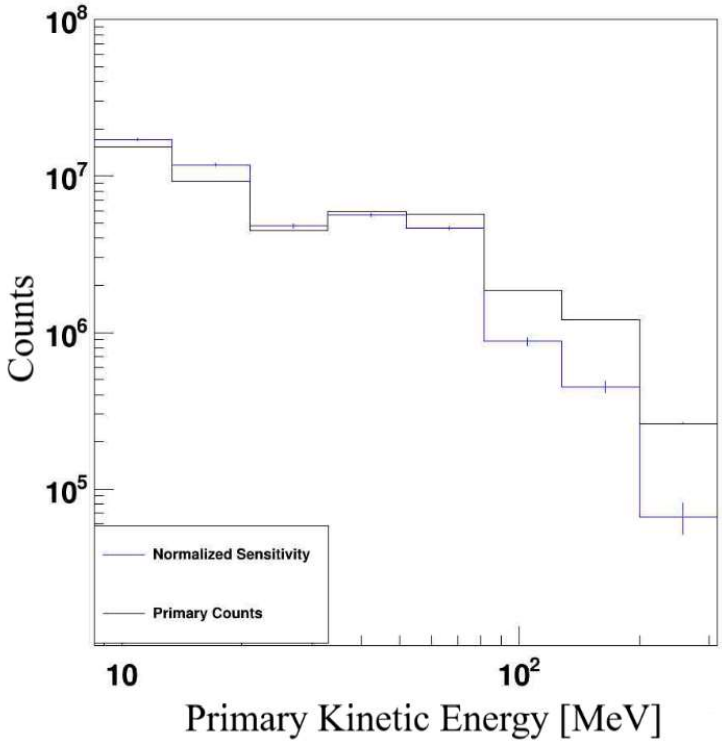


Figure 2.26 The sensitivity of proton telescope energy bins compared to the incident primary proton energy spectrum in Geant4 simulation.

Except for when the spectrum is fluctuating, the conical design exhibits better performance under trapped radiation than the single sized design. However, the number of events that are mis-identified as heavy ions was 1260 events out of the total 10^9. Which is two orders of magnitude higher than the previous design. So, a tradeoff between resolution and correct identification must be made. Under solar proton radiation the telescope also has good agreement with the primary spectrum as shown in Figure 2.27. With 62 misidentified particles, the mis-identification probability is still higher in this case than the single sized design.

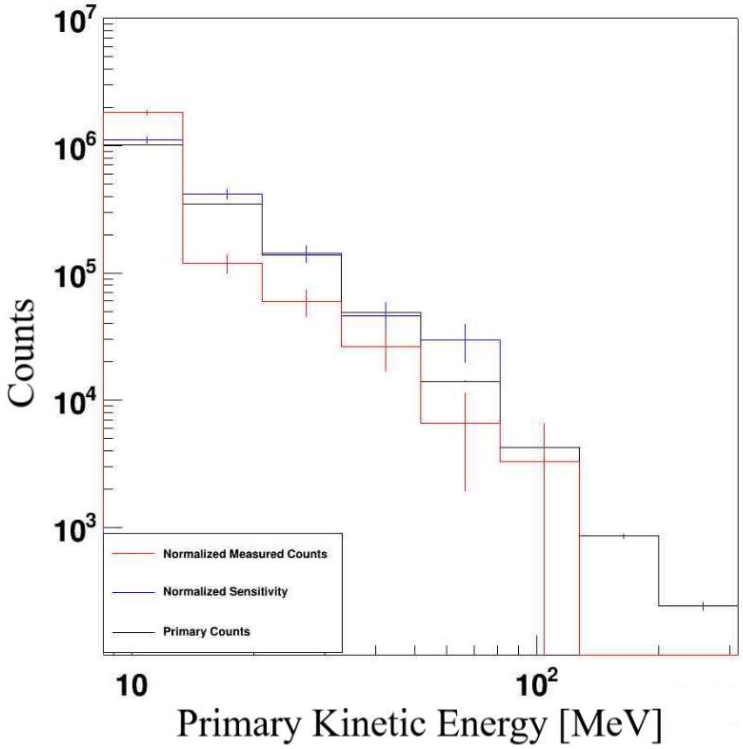


Figure 2.27 The sensitivity of proton telescope energy bins compared to the incident primary solar proton energy spectrum in Geant4 simulation.

To circumvent this issue, the portion of the primary spectrum being misidentified, in the trapped proton case was investigated. The sensitivity of heavy ion channels to primary proton energies can be used to clean the heavy ion channels of the proton contamination by finding the proportionality of the proton signals to the falsely identified heavy ions signals and removing this portion of the signal from the data. Thus, a simple way of cleaning the signal can be applied. Furthermore, under cosmic alpha radiation, the channel signals are directly proportional to each other. Making the opposite contamination (from heavy ions into proton channels) also removable as shown in Figure 2.28.

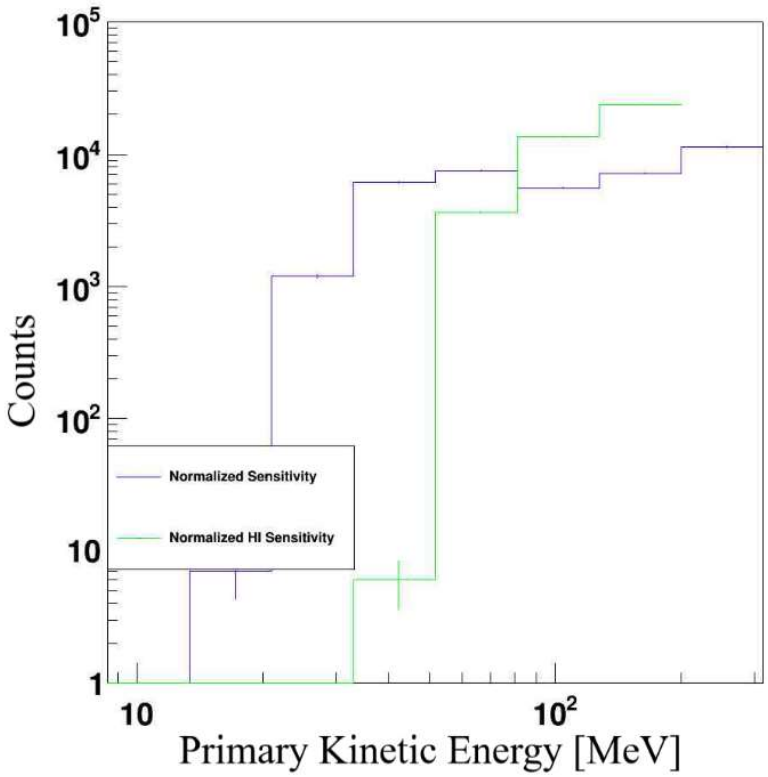


Figure 2.28 The sensitivity of proton telescopes proton channels and heavy ion channels against GCR alphas.

Under high energy proton irradiation, the resulting sensitivity curve are not in agreement with the primary spectrum in the high energy region since the higher energy particles penetrate the shield and cause an increase in the count rate in the low energy channels as shown in Figure 2.29.

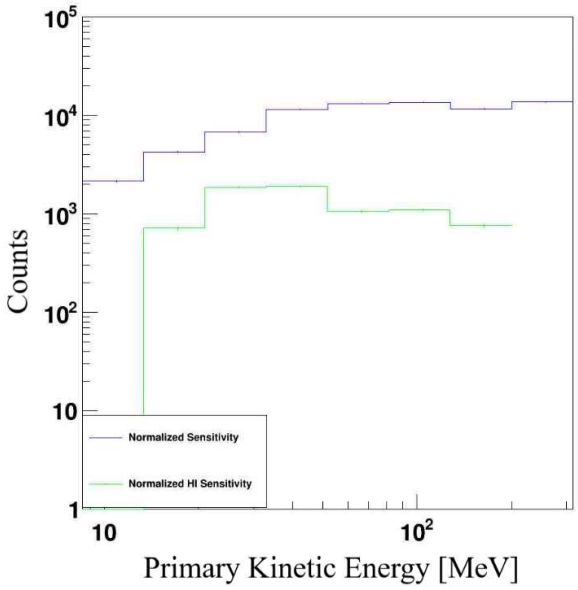


Figure 2.29 The sensitivity of proton telescopes proton channels and heavy ion channels against GCR protons.

This result indicates that by correlating the resulting counts in the heavy ion channels with their respective ratios from the sensitivity curves, the contamination from the heavy ion channels can be removed. This method accompanied with better shielding of the telescope will perform better under high energy proton radiation. The behavior of this design is summarized in Table 2.7. A comparison of this design's performance compared to the single sized design and an extended version of the conical design is presented in Table 2.8.

Table 2.7 Summary of simulation results of the conical geometry design.

Particle	**Inside design measurement energy region**	**Outside design measurement energy region**	**Contamination to other channels**
Electrons	No sensitivity	Can be removed (Electron Telescope)	Not significant
Protons	Good sensitivity Needs algorithm for reconstruction	Can be removed.	Can be removed and is low
Heavy ions	Good sensitivity	Can be removed	Can be removed (2 methods)

Table 2.8 Comparison between the design alternatives and their performance in the simulations at LEO environment

Performance At LEO trapped particle radiation	**Contamination in HI [/10^9]**	**Agreement of reconstruction to Truth**	**Statistics [/10^9]**	**Contamination from cosmic rays**
Single Sized	17	Bad agreement	19800	Insignificant
Conical Design	126	Good agreement	15000	significant (can be removed)
Extended Conical Design	105	Good agreement + 2 more bins	3800	Less significant (can be removed)

2.3.9.3 Performance at GEO

The same calculation was done for these geometries in GEO radiation environment to determine if they are suitable for GEO missions. The radiation environment at GEO and its comparison with LEO can be summarized in Table 2.9.

Table 2.9 Comparison between the radiation environments in LEO and GEO

Measurable proton flux [p/m^2/s]	**LEO-Heliosynchronous**	**GEO**
Trapped particles	10^2	10^{-2}
Solar particles	10^1 -10^9 (66% Exposure time)	10^7 (99% Exposure time)
Cosmic particles	10^3	10^4

The results of the simulations of the different designs in the GEO environment can be summarized in Table 2.10 .

Table 2.10 Comparison between the design alternatives and their performance in the simulations at GEO environment.

Performance At GEO	**Noise in HI [/10^9]**	**Agreement of reconstruction to Truth**	**Statistics [/10^9]**	**Noise from cosmic rays**
Single Sized	0	fails at high energy	2100	Insignificant
Conical Design	62	Good agreement	1200	significant (can be removed)
Extended Conical Design	9*	Good agreement + 2 more bins (not very active)	320*	Less significant (can be removed)

The conical geometry has good resolution for high energies and is suited for both GEO and LEO (HEO). It however lacks in particle differentiation accuracy. Single sized model is well suited for LEO orbits with low energy solar particles and shielded geo missions. It is also better at isolating Heavy Ions. The extended design has a weight issue. Along with statistics issue in the last bins. The conical geometry is better suited for noise reduction from cosmic rays with proper calibration. And is recommended to pursue as the main candidate.

* Different simulation technique was used to account for larger size. Comparison shown as a ballpark figure.

CHAPTER 3
YRM Readout Electronics and Detector Characterization with Data From Space Flight

In this chapter, measurements of one of the silicon detector candidates of YRM and the readout electronics design and performance will be presented. The properties of the DDA3 and TDA detectors manufactured by TÜBITAK BİLGEM UEKAE YİTAL such as their leakage current and reverse bias relationship (I-V) are measured as well as their reverse bias and capacitance relationship (C-V) characteristics. The detectors response to ionizing radiation is also investigated along with the electronic readout behavior from the incident particles. Signal-to-Noise Ratio (SNR) values are also compared for different setups with radioactive sources and 15 MeV and 30 MeV protons from METU-DBL [48].

The ROKETSAN SR0.1 sounding rocket carried the YRM prototype code named (SB) up to an altitude of 136 km twice on the 26^{th}-29^{th} of October 2020. The data obtained from a sounding rocket test flight to space is analyzed and presented.

3.1 I-V Characteristics

The DDA3 detector is circular in shape with a radius of 7mm divided into 4 quadrants with a thickness of 0.52 mm. Subjecting this detector to a reverse bias voltage at room temperature will result in a leakage current as shown in Figure 3.1. These measurements were taken in the IVMER lab in an ESD-safe dark chamber controlled at 23℃ since this diode is sensitive to visible light and to temperature changes. The measurement was performed using a Keysight 34470A multimeter for as a sensitive ammeter.

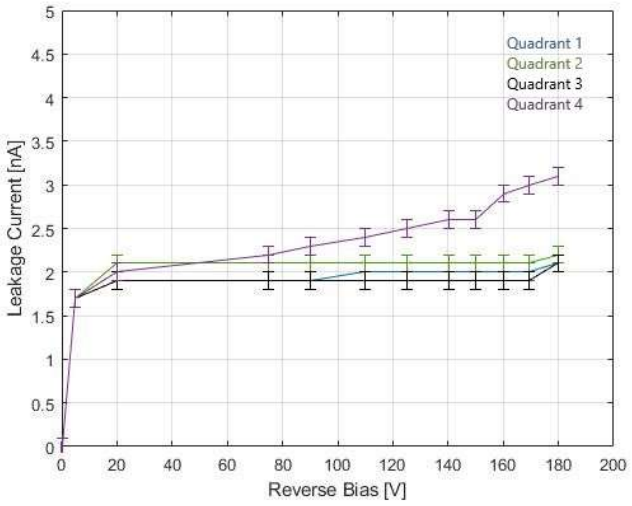


Figure 3.1 The I-V Characteristics of DDA3 Detector Quadrants.

The measurements show that the DDA3 detector has a low leakage current (<3nA) in all its quadrants up to a reverse bias voltage of 180V, which is beneficial for low noise particle detection [66]. Another version of the same detector where the area of the diode is not divided into four quadrants was supplied by TÜBITAK YİTAL as a suitable candidate for YRM's proton telescope for the single sized design. Named TDA, this detector has the same area and thickness as DDA3, but with a single active area. The I-V Characteristics of this detector is measured using the same setup and is shown in Figure 3.2. Since this detector has an active area four times larger than the active area of the quadrants in DDA3, the leakage current is also larger for any given reverse bias voltage. However, the leakage current values are only limited to < 20 nA which is still suitable for low noise particle measurements with a larger detector area.

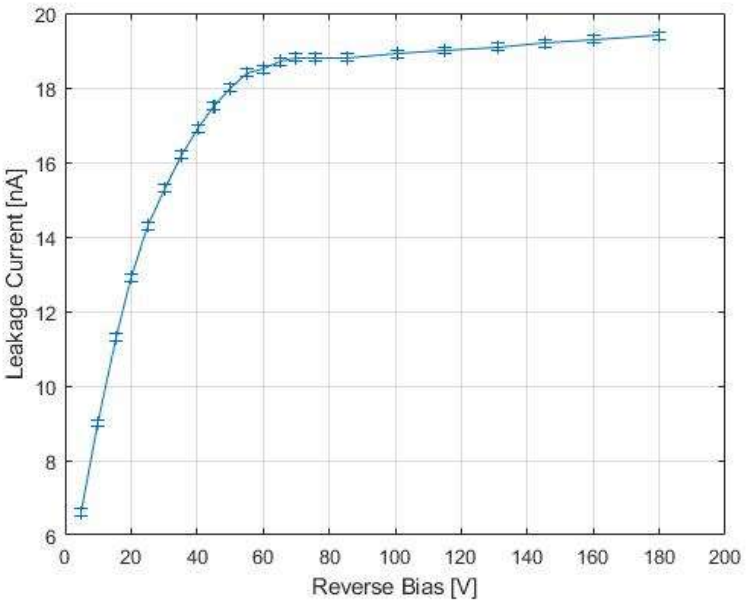


Figure 3.2 I-V Characteristics of a TDA Detector.

From theses graphs, it can be seen that the full depletion point where the leakage currents stops increasing exponentially and starts increasing linearly is at 40 ±5 V [67, 68]. To achieve a sizable particle signal using these detectors, the reverse bias voltage should be high enough to achieve full depletion and also provide high enough electric field to improve the charge collection efficiency and thus decrease the pulse width. Doing so will help increase the maximum particle rate the detector is able to measure. Since the breakdown voltage of these detectors is specified at 200V, the reverse bias voltage selected for YRM's detectors is set at 180V, using 20V as a safety margin.

Leakage current (J_R) of PIN diodes is commonly described in literature as a combination of the diffusion current (J_{Diff}) and the generation current (J_{Gen}) as shown in Equation (3.1) [69].

$$J_R = J_{Diff} + J_{Gen} = q\sqrt{\frac{D_p}{\tau_p}}\frac{n_i^2}{N_A} + \frac{qn_iW}{\tau_e} \tag{3.1}$$

where q is the charge of the electron, $D_p$is the diffusion coefficient of silicon, τ_p is the minority carrier lifetime, τ_e is the effective lifetime, n_i is the intrinsic carrier concentration, N_A is the doping concentration and W is the depletion width. The depletion width increases with the square root of the reverse bias voltage as described by Equation (3.2) [69].

$$W = \sqrt{\frac{2\varepsilon_s}{qN_A}(V_{bi} + V_R)} \tag{3.2}$$

where ε_s is the permittivity of silicon, V_{bi} is the built-in potential of the junction and V_R is the reverse bias voltage. Thus, the leakage current of the silicon diode is a function of the square root of the reverse bias voltage and can be expressed as in Equation (3.3)

$$J_R = A + B\sqrt{V_R} \tag{3.3}$$

where A and B are fitting parameters representing J_{Diff} and J_{Gen} respectively. The minority carrier lifetime and the effective carrier lifetime are dependent on the temperature and are difficult to estimate theoretically without an injection current measurement. Thus, the effect of temperature on the leakage current must be investigated.

3.2 Temperature Dependence of the Leakage Current

The leakage current dependency of TDA on temperature was investigated by using a MIKROTEST mst-120 oven at the IVMER lab. The oven was used to heat the detector attached to a readout PCB while the measurement equipment was connected via probes from outside the oven. When the setup reached thermal equilibrium, the leakage current of the detector stabilized, and the measurement was taken. How the IV curves depend on temperature can be seen in Figure 3.3. The curves fit to a square root function up to the point of full depletion and then stabilize to a constant value.

The measurements can be used to determine the doping concentration in silicon crystal of the PIN diodes.

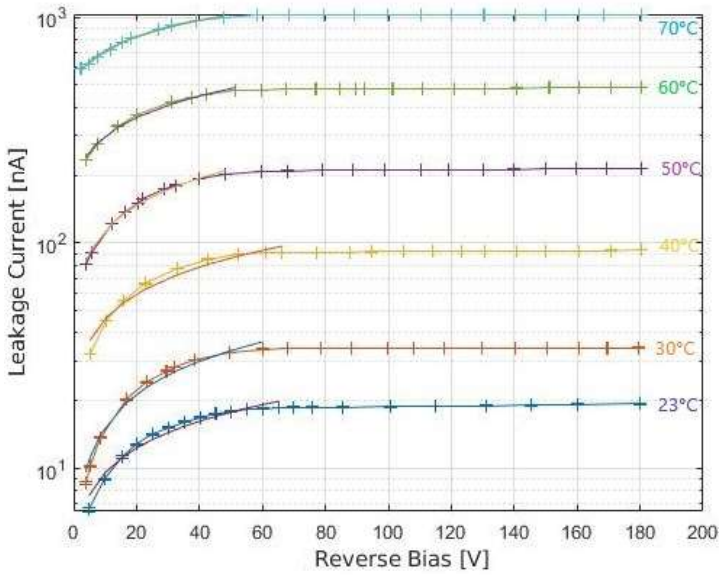


Figure 3.3 The dependence of the I-V characteristics of the TDA detector on temperature. Solid lines correspond to the fit functions.

The curves fit the model in Equation (3.3) using a script with χ^2 values higher than 0.95 for the A and B parameters listed in Table 3.1, showing that the measurements are conforming with the prediction. A defines the leakage current at 0 V reverse bias and B defines the proportionality of the leakage current to the square root of the reverse bias voltage.

Table 3.1 A and B Fit Parameters from Equation (3.3) Calculated for TDA for Different Temperatures

Temperature [ºC]	A [nA]	B [nA/V$^{1/2}$]
23.0 ± 0.1	3.0 ± 0.1	2.1 ± 0.1
30.0 ± 0.1	6.6 ± 0.1	4.6 ± 0.1
40.0 ± 0.1	13.9 ± 0.1	10.2 ± 0.1
50.0 ± 0.1	33.2 ± 0.1	25.4 ± 0.1
60.0 ± 0.1	146.6 ± 0.5	47.6 ± 0.1
70.0 ± 0.1	455.8 ± 0.5	81.0 ± 0.1

The leakage current of a PIN diode depends on the temperature through the following Equation:

$$J_R = C \times \exp\left(\frac{-E_a}{kT}\right) \tag{3.4}$$

where C is a fitting constant, E_a is the activation energy, k is Boltzmann's constant and T is the temperature in kelvins. So, a plot of the logarithm of the leakage current versus 1/kT should be linear with a slope of $-E_a$. This plot for different reverse bias voltage values is presented in Figure 3.4 and the values calculated for E_a are shown in Table 3.2. These results again show that full depletion is reached at 40 ±5 V of reverse bias since the change in E_a switches from exponential to linear with a very low slope.

Table 3.2 Activation Energies for different Reverse Bias Voltages as Calculated by Fitting of the Data in Figure 3.4 to Equation (3.4).

V_R: Reverse Bias Voltage [V]	E_a: Activation Energy [eV]
20.0 ± 0.1	0.81 ± 0.01
30.0 ± 0.1	0.79 ± 0.01
40.0 ± 0.1	0.78 ± 0.01
50.0 ± 0.1	0.78 ± 0.01
70.0 ± 0.1	0.77 ± 0.01
100.0 ± 0.1	0.77 ± 0.01
120.0 ± 0.1	0.77 ± 0.01
160.0 ± 0.1	0.77 ± 0.01
180.0 ± 0.1	0.77 ± 0.01

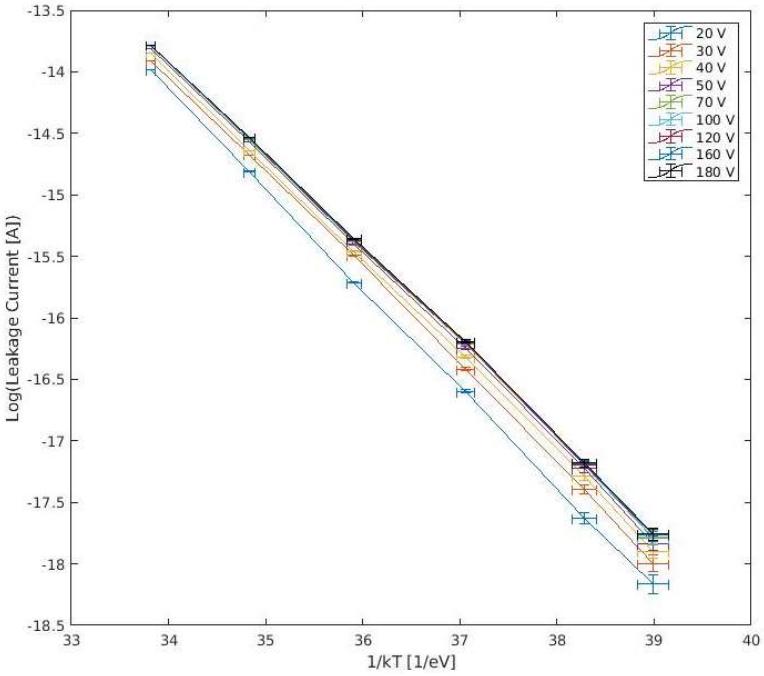


Figure 3.4 Linear fits to the logarithm of leakage current against 1/kT for activation energy calculation of the TDA detector.

3.3 C-V Characteristics

The change of the capacitance of the detector as the reverse bias voltage changes is one of the most important properties to be investigated. The capacitance curve can show the full depletion width and along with the I-V curve provide information about the doping of the PIN diode. The C-V curve was measured for a DDA3 detector using a Keysight B1500A semiconductor characterization device in YITAL laboratories. The results can be seen in Figure 3.5. It should be noted that error bars are not provided by the device for error propagation analysis. Figure 3.5 clearly shows that full depletion occurs for both detectors at 40 ±5 V. The capacitance C of the detector is related to the reverse bias voltage with Equation (3.5) [67]:

$$C = qAN_A(W)\frac{dW}{dV_R} \tag{3.5}$$

where $N_A(W)$ is the doping concentration as a function of the depletion width. Here, C is directly dependent on the derivative of the depletion width with respect to the reverse bias voltage $\frac{dW}{dV_R}$. The depletion width W dependence on the capacitance is described by (3.6):

$$W = \frac{K_s\varepsilon_0 A}{C} \tag{3.6}$$

where K_s is the semiconductor dielectric constant, ε_0 is the permittivity of free space. Thus, the doping concentration becomes:

$$N_A(W) = \frac{2}{qK_s\varepsilon_0 A^2 \cdot d(1/C^2)/dV_R} \tag{3.7}$$

Here, the doping concentration depends on the slope of the $1/C^2$ versus V curve. A script was used to perform the calculation above and the results are shown in Figure 3.6. The doping concentration of 2-8×10^{12} ions/cm^3 agree with the specifications provided by the manufacturer [70]. The expression in (3.7) is only valid until the full depletion point [55]. Variation of the doping concentration from the model depends on many factors such as the internal geometry of the PIN diode layers and the quality of the silicon crystal manufacturing process, the analysis of which is beyond the

scope of this thesis. According to the manufacturer, the doping concentration of the DDA3 and TDA detectors does not change much inside the silicon crystals for the entirety of its depth since they are grown in the same homogenous and mostly pure environment. An impurity concentration in the range of 10^{11}-10^{12} cm^{-3} is considered to be very pure.

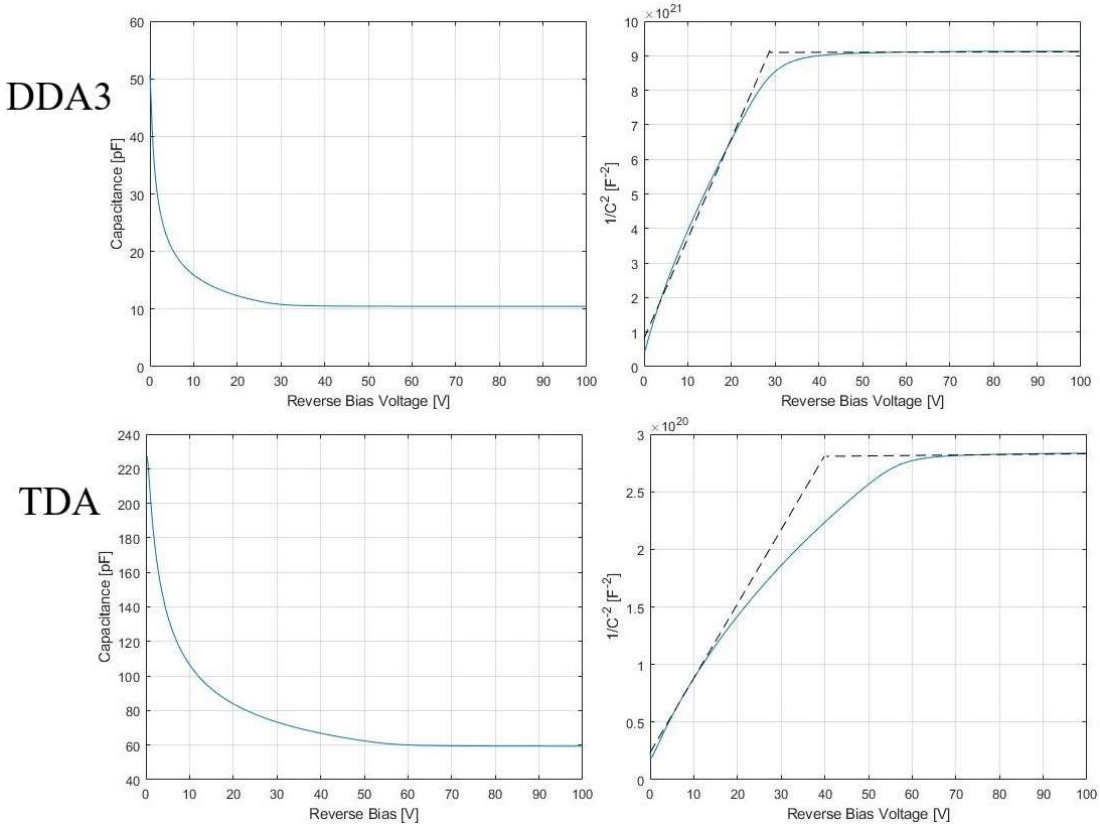


Figure 3.5 C-V (upper left) and $1/C^2$-V (upper right) plots for a single quadrant in a DDA3 detector and C-V (lower left) and $1/C^2$-V (lower right) plots for the TDA detector.

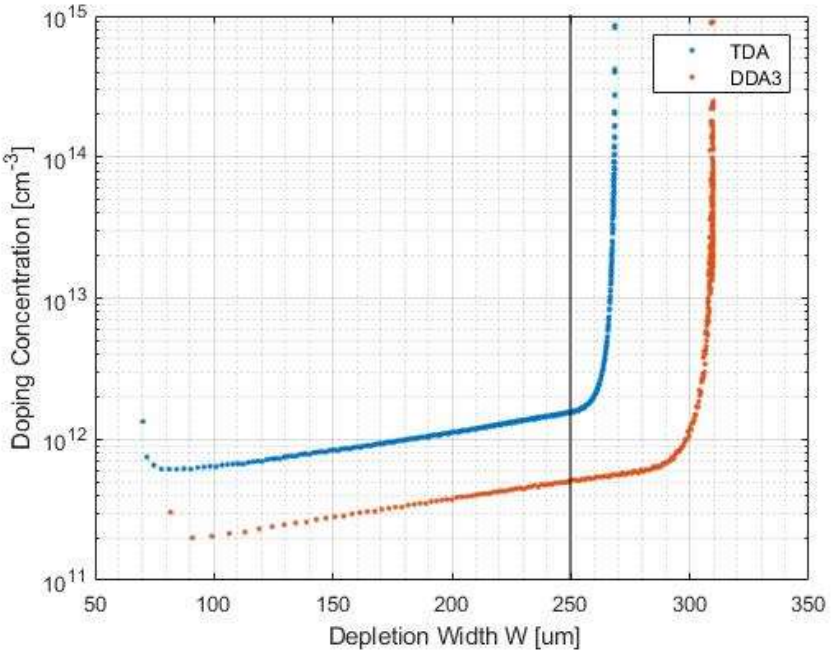


Figure 3.6 The doping concentration in the DDA3 and TDA detectors obtained as a function of the depletion width. The model used to generate data right of the black line is considered invalid [67].

3.4 Prototype Radiation Monitor (SB) and Readout Electronics

An initial prototype of YRM's working principal, code named "SB", was designed to test the detectors' sensitivity to space radiation, the readout electronics performance and the FPGA logic. The size of the SB box was limited to 110x70x60 mm by ROKETSAN^{TM}, which influenced the mechanical and electronic design choices. The prototype employs two DDA3 detectors in a vertical alignment to perform coincidence logic. Each detector has its readout card which feeds a logical signal to the FPGA card in the middle as shown in the CAD drawing in Figure 3.7. DDA3 is light sensitive and very fragile and therefore must operate inside a light-tight metal SB box. The prototype also incorporates a glass Geiger tube sensitive to electrons and gammas to compare the counts of particles outside the box measured during the test period. This prototype was sent to space on a sounding rocket in late

October in collaboration with ROKETSAN^{TM} [71]. The device was limited at a mass of 0.5 kg and a power consumption of 5 W. The 2mm thick aluminum shielding on top of SB was thinned in an area that is 8 mm wide to 2 mm to allow for more particles to pass through right above the DDA3. A J305βγ type of length 90 mm was selected to fit above the box and is biased at 400V. It has a functional temperature range between -40℃ and 55℃ and is certified for a lifetime up-to 10^9 particles. The box was powered by 28 V and was required to send data over RS422.

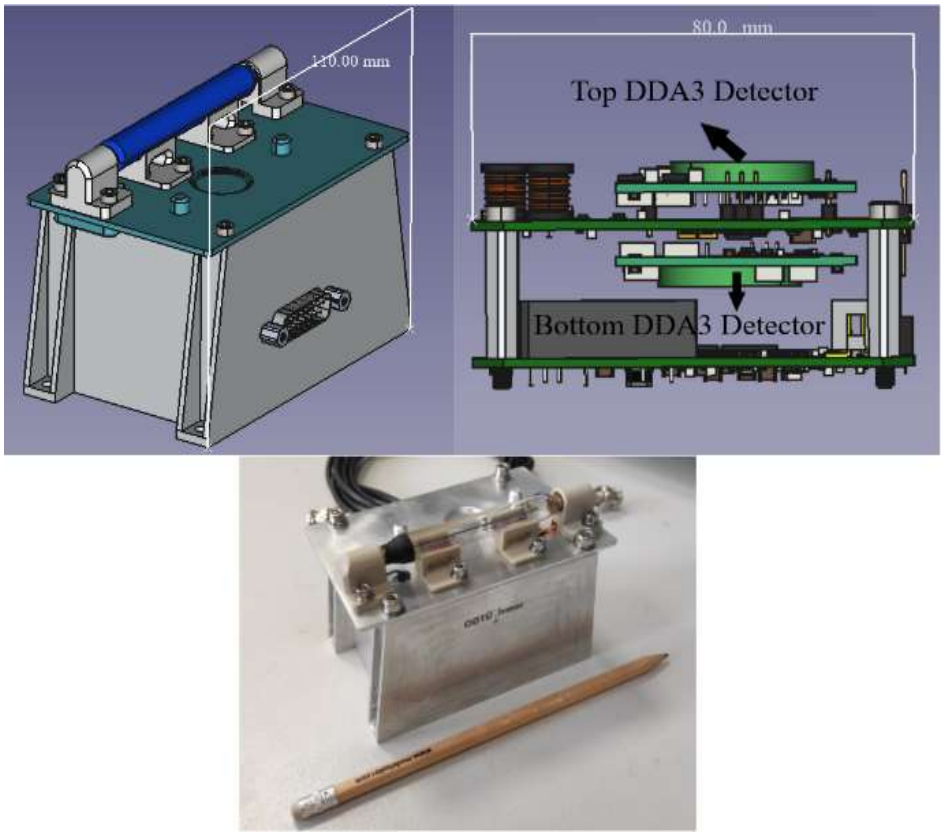


Figure 3.7 The CAD design of the prototype Radiation Monitor "SB" in the upper panel and a picture of the flight module with a pencil for scale in the lower panel.

The design of the readout electronics for these detectors went through several stages. At first, the circuit employed a two-stage amplification of the signal through a preamplifier (U2) and an amplifier (U3) as shown in Figure 3.8. The amplified signal

is then fed into a comparator (U4) that has a low and high threshold discrimination levels for noise suppression and for separating MIPs from stopping particles respectively. The reference voltage for the comparator is defined using a voltage divider at the inverting input of the comparator. The digital output from the comparator is then fed to an IGLOO2 FGPA to count particles and coincidences between the two silicon detectors. Initially the four quadrants of DDA3 (A1-4) were joined immediately at the output of the detector to allow for use of the whole detector area as a single detector as shown in the circuit schematic.

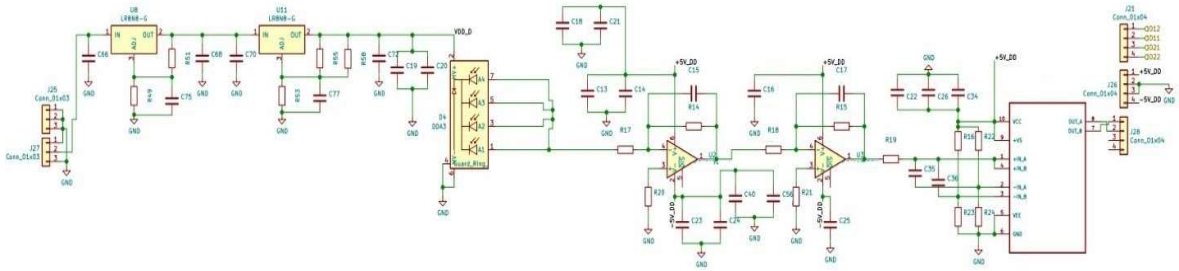


Figure 3.8 Circuit diagram for the prototype Radiation Monitor, version 1.

This design was printed on a 2-layer PCB and the electronics were calibrated using alphas from an Am-241 source. The combination of the detector quadrants before being discriminated increased the noise levels in the circuit significantly. Moreover, the two-stage amplification had the effect of amplifying the noise as well as the signal pulses. Thus, the SNR values were poor even at very high thresholds as shown in Figure 3.9. The measurement was performed using a Lecroy PP022 probe connected to a Teledyne Lecroy WaveRunner8254 oscilloscope at the preamplifier (U2) output with the alphas from an Am-241 alpha particle source.

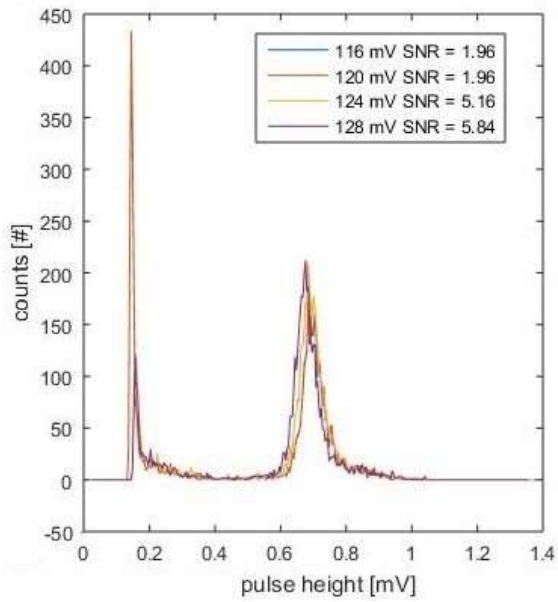


Figure 3.9 Pulse height histogram showing the preamplifier (U2) output in response to alpha hits from an Am-241 source. Blue curve is under the orange one.

The design in Figure 3.8 was revised through multiple steps to include a comparator with a single noise eliminating threshold after a single stage amplification as shown in Figure 3.10. The first trans-impedance amplifier transforms the current signal into a voltage pulse and amplifies it, while the second amplifier has a gain of 1.3 and serves mostly as an inverter. Different quadrants of the DDA3 are no longer joined before the amplification stage. Instead, the noise suppressed digital outputs of the comparators are joined using an OR logic gate. In addition, the measurement of the noise levels is no longer made using the probe but rather through the digital output of the OR gate to minimize the interference of the measurement with the results. The comparator also employs an external hysteresis positive feedback loop that in addition to its own provides an additional 41 mV to its internal 9mV hysteresis value. This helps the comparator to discriminate sensitively against noise levels close to the reference voltage.

The final circuit diagram is shown for one quadrant of the DDA3 detector in Figure 3.10. All quadrants are readout through the same circuit topology. Feedback capacitances of the first stage amplifiers have been removed in this version since the

parasitic capacitance of the setup is enough to supply the 0.1 pF capacitance necessary to achieve the required amplification. A comparison of different feedback capacitance values on the signal at the output of the amplifier, U1, which alpha particles from an Am241 source is shown in Figure 3.11. No feedback capacitance option is shown to be superior in terms of SNR, since while the noise level stays the same the signal is highest.

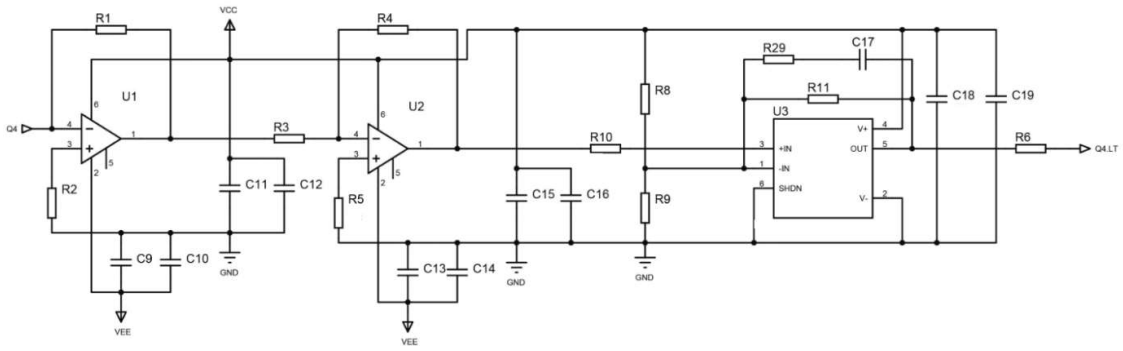


Figure 3.10 Final version (v11) of the circuit for the prototype radiation monitor for a single quadrant of the DDA3 detector.

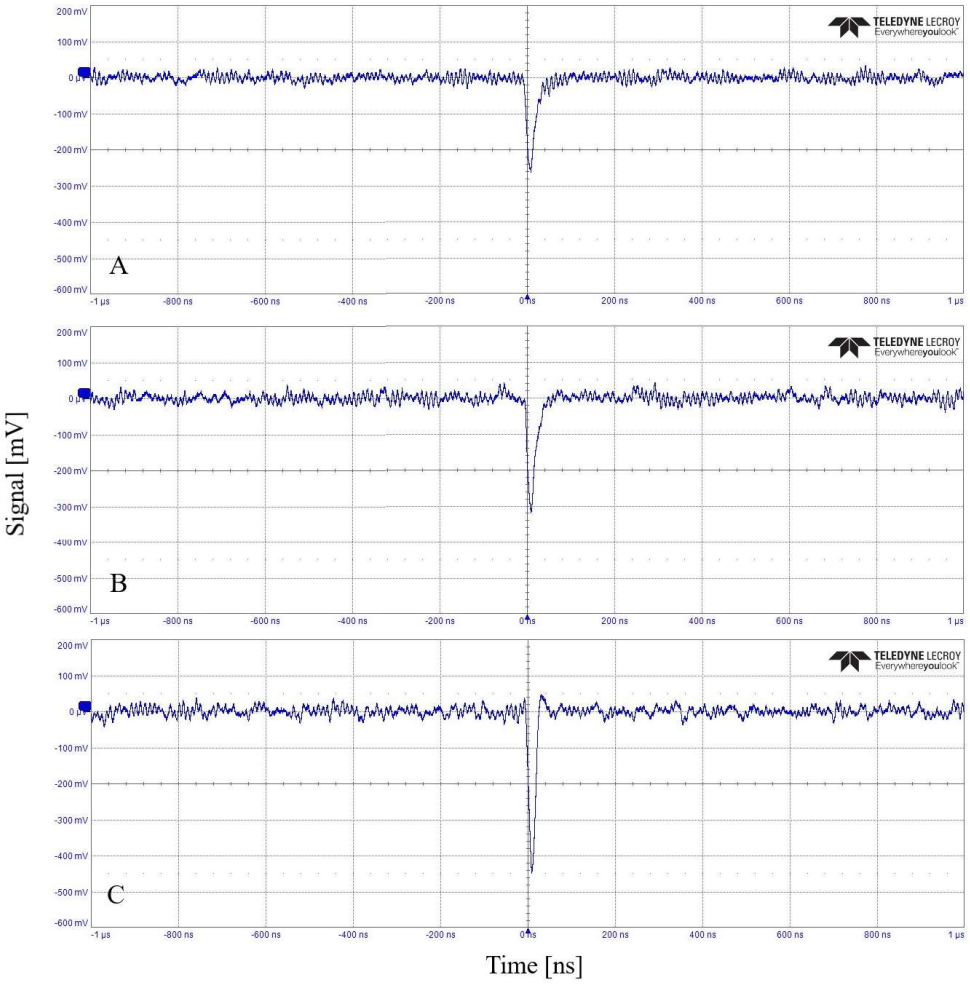


Figure 3.11 Comparison of the pulse generated by an alpha particle from an Am241 source for 0.2pF (A), 0.1pF (B) and no capacitance (C) for the feedback on the U1 op-amp as seen by a Lecroy WaveRunner8254 oscilloscope.

3.5 Calibration of the Prototype Radiation Monitor (SB)

On a sounding rocket SR0.1 that goes up to 136 km, the prototype radiation monitor is not expected to be exposed to trapped radiation, but only to cosmic rays penetrating into the upper atmosphere and their secondaries as shown in Figure 1.7. The MIPs in those high altitudes are the sensitivity target for this experiment, since the energy deposition of the MIPs is the lower limit of all other particles for the same

species. This means that if a radiation monitor can measure MIPs of a certain species, it is also able to measure all primaries of that species regardless of kinetic energy. To calibrate the radiation monitor, SB, it was tested with alphas from an Am-241 source in air environment in the IVMER lab. The distance between the source and the detector was changed and the generated pulse height spectrum was measured in one-minute intervals. The number of counts fall as expected with increasing distance since the intensity of the radiation is depends on r^2. The results are shown in Figure 3.12.

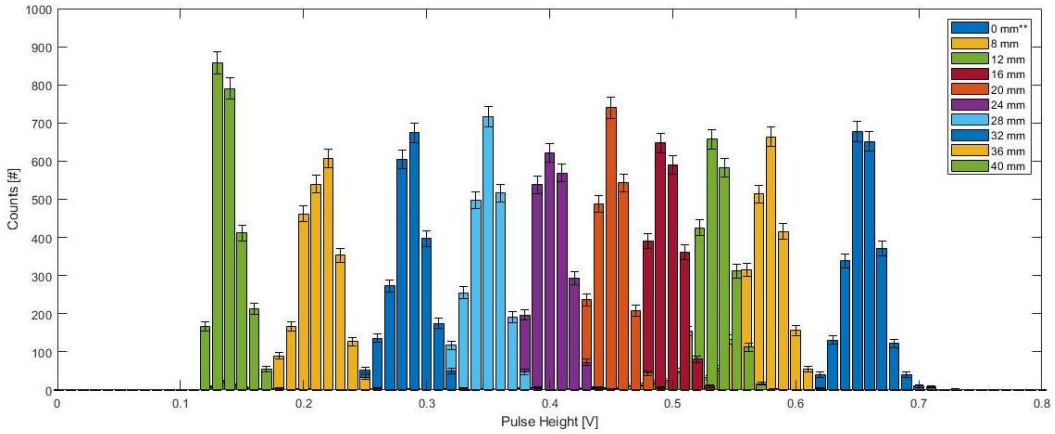


Figure 3.12 Measured Pulse Height of Am-241 alpha particles with different distances between the source and the detector. (**) The measurement at 0 mm indicates measurement done in vacuum (5×10^{-2} torr) and at 35mm distance from detector.

The energy deposition of the alpha particles from Am-241 in air was also simulated using Geant4 and taking into account the air density in Ankara at the time ($\boldsymbol{\rho_{Air}}$ = **1.08 kg/m^3**). The maximum range of an alpha from Am-241 in silicon is 28 μm, calculated using SRIM [72]. The Geant4 simulation result for energy deposition were compared with the measurements of the pulse heights at different distances as shown in Figure 3.13. This plot shows the linear correlation between the energy deposited in the detector and the measured pulse height to be used in determining the particle energy for a given pulse height. This calibration was performed for preamplifier U2 gain value of 1.3. The was chosen to make sure that the minimum pulse width

(resulting from a particle depositing an energy equivalent to the threshold voltage at the comparator U3) is wide enough to be detectable by the FPGA at all times as will be shown in Section 3.6.

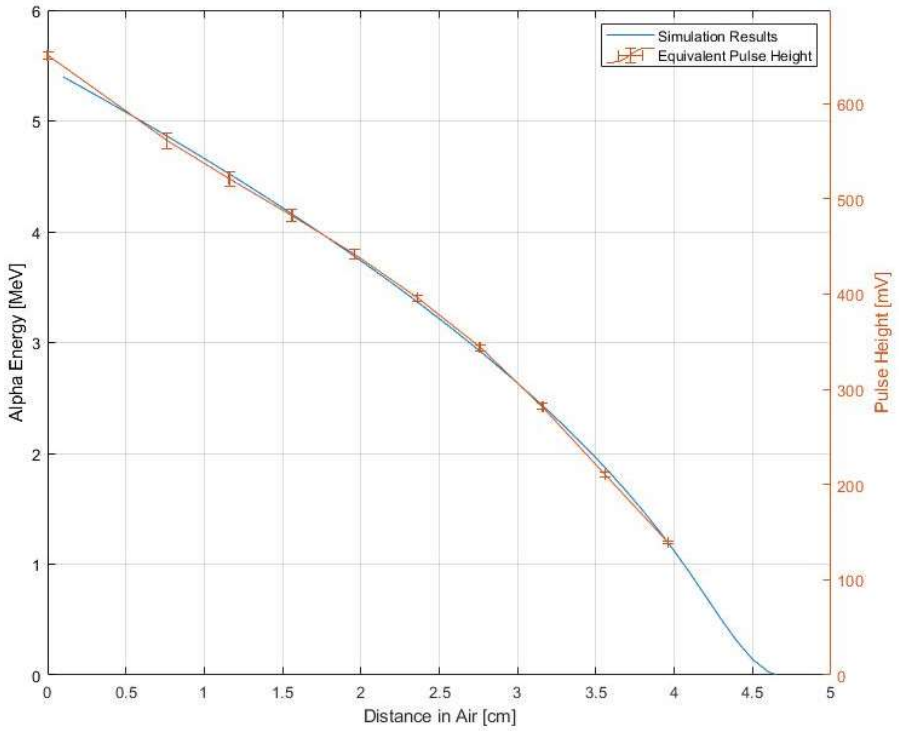


Figure 3.13 The similar behavior of Geant4 simulation results of alpha energy deposited in the detector and Am-241 alpha pulse heights at different distances between the source and the detector demonstrated a linear correlation (ratio = 116.2 mV/MeV).

The energy deposition of the common cosmic ray MIPs was also simulated using Geant4. The energy depositions for different particles as well as the equivalent pulse heights that were calculated using the alphas from an Am-241 calibration source are presented in Table 3.3. The noise in the detector readout electronics must be lower than the equivalent pulse height for the particles in question for a reliable readout.

Table 3.3 Energy depositions of common cosmic ray MIPs in the detector from Geant4 and the calculated corresponding equivalent pulse height from the calibration.

Particle	**Source**	**Mean Energy Deposition [MeV]**	**Equivalent Pulse Height [mV]**
Alpha	Am-241 (1.72 mm)	3.92 ± 0.01	457.3 ± 1.2
Alpha	MIP	1.40 ± 0.04	161.2 ± 4.7
Proton	MIP	0.43 ± 0.05	50.1 ± 5.8
Muon	MIP	0.25 ± 0.03	29.2 ± 3.5

The noise in the detector readout electronics was measured by changing the reference voltage at the inverting input of the comparator at U2 gain of 1.3 by changing the R9 resistance and measuring the number of counts per minute at the OR gate output. At 74 mV reference voltage, the noise count rate was less than 1 particle/minute, which was the upper noise limit for this design since the expected particle fluxes to be measured are low. At lower reference voltages, the count rate was seen to be higher than the set limit. Thus, the lower threshold was set at 74 mV for the prototype radiation monitor. The same measurement was repeated with the alphas from an Am 241 particle source at 1.7±0.1 cm distance and the results are shown in Figure 3.14. At high reference voltages corresponding to energies higher than that of the alpha particle, the count rate falls sharply. At around 500 mV, the detector is able to measure all the alpha particles reaching it. The count rate increases slightly at reference voltages lower than 100 mV because of the noise induced by the measurement procedure.

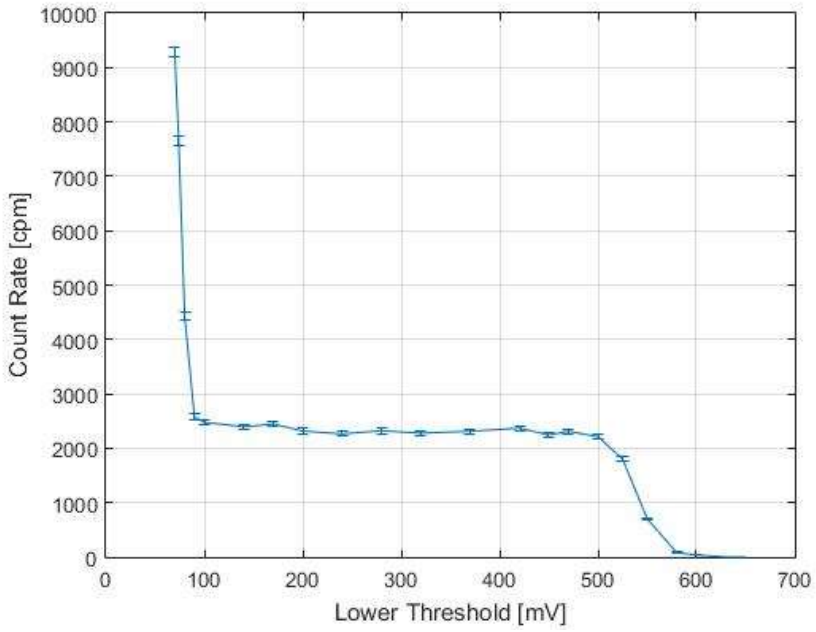


Figure 3.14 Threshold scan performed using Am-241 source at distance 1.7±0.1 cm from the detector.

3.6 FPGA Logic for SB

To achieve better noise rejection and distinguish low and high $\frac{dE}{dx}$ of particles in the detectors, signal width algorithms were introduced to the FPGA. The signal arriving at the FPGA from the detectors has a width proportional to the amount of time the analog signal is above the reference voltage in the comparator (U3). Thus, a low energy or a noise hit will result in a narrow input signal for the FPGA, while a high or a stopping particle will result in a wide signal as shown in the comparison in Figure 3.15.

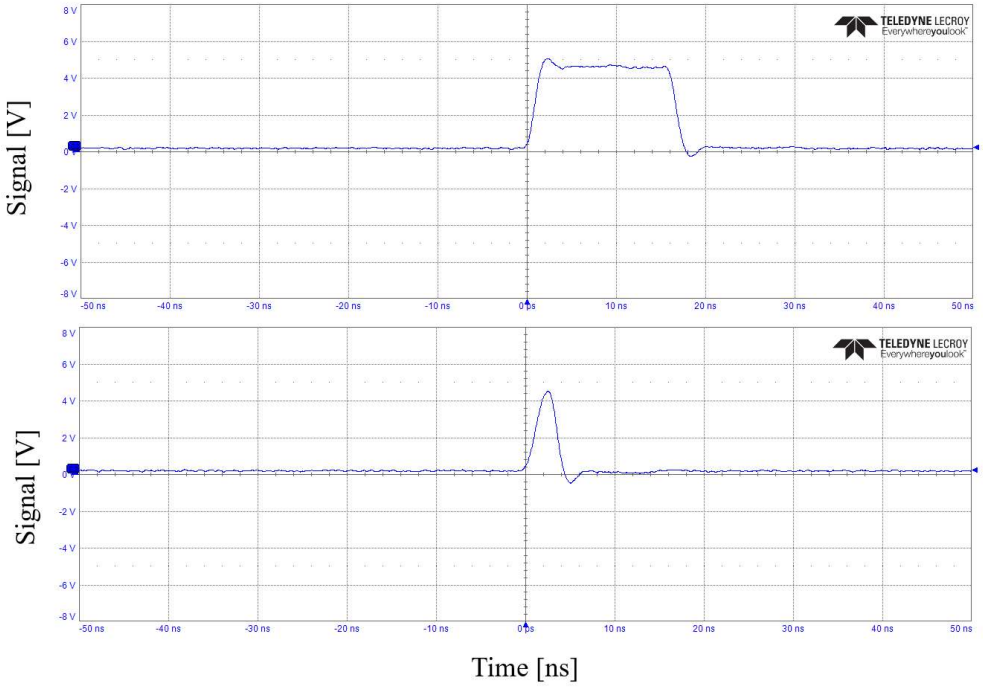


Figure 3.15 Comparison between low energy or noise hit (below) and a high energy or stopping particle (above) signal shapes at the comparator output (U3) as seen by a Lecroy WaveRunner510 oscilloscope.

The IGLOO2 FPGA employs a 128 MHz clock which corresponds to a 7.8 ns signal width [73]. The FPGA is able to detect the signal on each rising and falling edge of the clock, so signals that are narrower than 7.8 ns have a chance to be missed by the FPGA. Thus, the gain of the U2 amplifier was adjusted to 1.3 to make sure the minimum signal width is larger. Higher energy deposition will result in wider signals that span over multiple clock cycles. Trivial FPGA counting of above the 3.3 V threshold signals on each clock cycle might result in some particles being counted multiple times. Moreover, depending on the environmental conditions, some ringing in the signal can also happen due to op-amp oscillations as shown in Figure 3.16 [74]. Therefore, the FPGA must incorporate deadtime into its counting algorithm such that when a particle is detected the algorithm will stop counting for some amount of clock cycles.

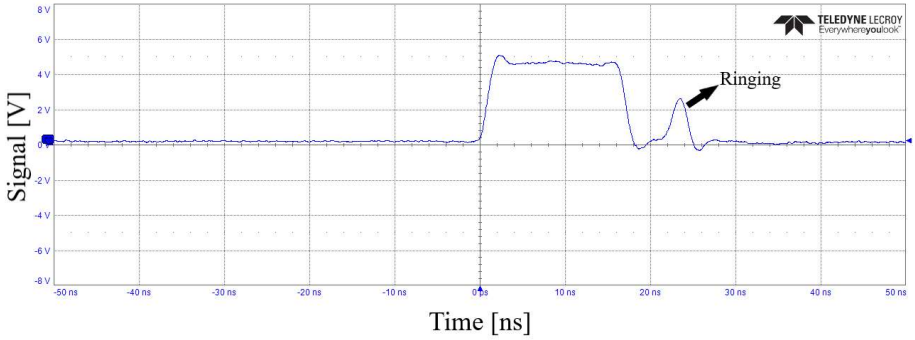


Figure 3.16 Particle signal in the showing ringing in the output of the comparator (U3) as recorded by a Lecroy WaveRunner8254 oscilloscope.

The number of cycles that correspond to an alpha particle from an Am-241 source hitting the detectors was determined by dumping the data recorded by the FPGA in a 128 clock cycle, for 4096 times. The resulting data dump is shown in Figure 3.17.

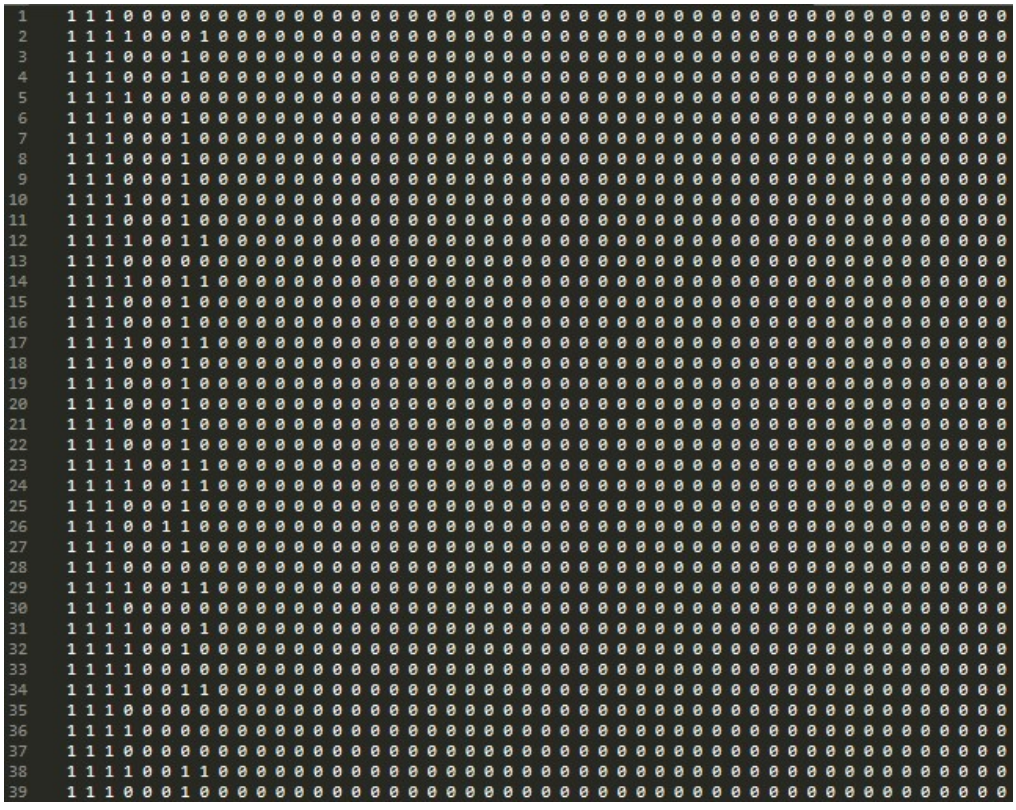


Figure 3.17 A snippet from the data dump generated by the FPGA for the readout by the DDA3 tested with alphas from an Am241 source.

Analysis of the data dump reveals that a typical energetic particle (~ 5 MeV) corresponding to a response of ~ 700 mV at the comparator input will result in the FPGA being triggered for at least 3 consecutive cycles. This was further tested by counting the alphas measured per minute with different cycle threshold settings. For cycle thresholds larger than 3, the efficiency begins to drop as some alphas fail to produce long enough pulses. The results are shown in Figure 3.18 verifying the choice of 3 cycles with different (120 and 80 ns) deadtime settings. Thus, the trigger threshold was set to 3 cycles for DDA3 “High threshold (HT)” channels. Another data accumulating channel was setup called the “Low Threshold (LT)” channel to record events shorter than 3 cycles.

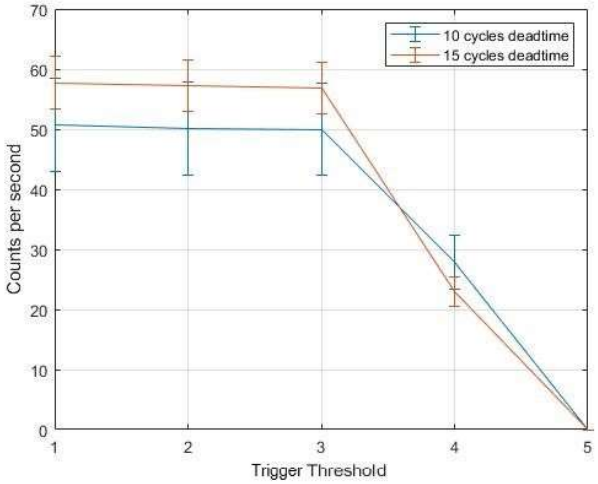


Figure 3.18 Cycle threshold scan of signal width for the FPGA algorithm for different deadtimes.

A comparison of the counts per second in LT and HT channels versus distance is shown in Figure 3.19 for alphas from an Am-241 source. The count rates overlap which is indicative of a clean signal with minimal noise and no ringing. In order to stay on the safe side and since the expected particle fluxes to be measured are low, the deadtime was set to 15 cycles after the trigger for both LT and HT channels.

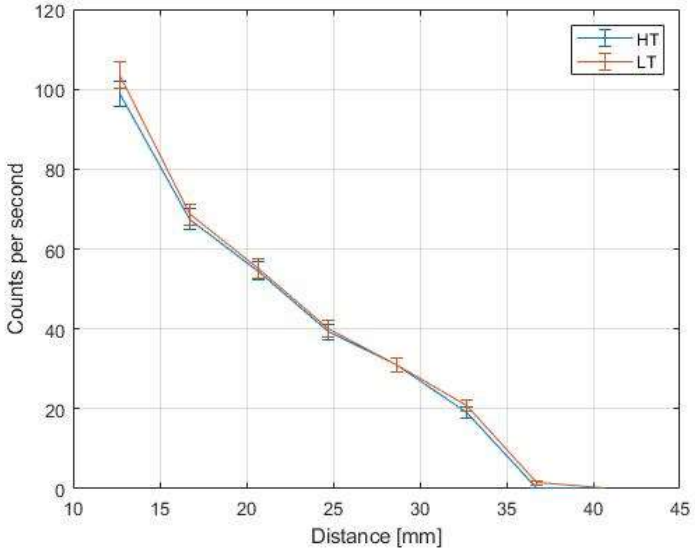


Figure 3.19 Comparison of count rates for HT and LT channels versus distance using an Am-241 alpha source.

The FPGA uses UART with an RS422 interface for sending the measured data. SB was designed to send out one data packet containing 64 bytes per second, containing the accumulated particle counts during that second. The data packet also contains 4 header bytes,15 sub-header bytes and a CRC byte to maintain the integrity of the data through rough operating telemetry conditions as shown in Table 3.4. An example of the data packet is shown in Figure 3.20. For verification and redundancy purposes, the data packet also contains information about the total accumulated particle count in each DDA3 detector channel individually as well as the Geiger counter. This packet is replicated by the main computer of SR0.1 and sent to the ground 100 times per second to prevent packet loss and achieve more redundancy.

Table 3.4 Data format of the packet sent by SB.

Offset	Size [Bytes]	Parameter	Content
0	4	Header	9A 4E B5 98 (constant)
4	1	Sub Header	0x00
5	2	Time	Time counter increasing by 1 per second
7	1	Sub Header	0x01
8	3	Geiger Total	Total count in Geiger since power on
11	1	Sub Header	0x02
12	3	DDA3_HT Total	Total count in top DDA3_HT since power on
15	1	Sub Header	0x03
16	3	DDA3_LT Total	Total count in top DDA3_LT since power on
19	1	Sub Header	0x04
20	3	DDA3_HT Total	Total count in bottom DDA3_HT since power on
23	1	Sub Header	0x05
24	3	DDA3_LT Total	Total count in bottom DDA3_LT since power on
27	1	Sub Header	0x06
28	3	Geiger 1s	Counts in Geiger in the past 1 second
31	1	Sub Header	0x07
32	3	DDA3_HT_1s	Counts in top DDA3_HT in the past 1 second
35	1	Sub Header	0x08
36	3	DDA3_LT_1s	Counts in top DDA3_LT in the past 1 second
39	1	Sub Header	0x09
40	3	DDA3_HT_1s	Counts in bottom DDA3_HT in the past 1 second
43	1	Sub Header	0x0A
44	3	DDA3_LT_1s	Counts in bottom DDA3_LT in the past 1 second
47	1	Sub Header	0x0B
48	3	Coincidence_1	Coincidence counter for top and bottom DDA3 HT per second
51	1	Sub Header	0x0C
52	3	Coincidence _2	Coincidence counter for top and bottom DDA3 LT per second
55	1	Sub Header	0x0D
56	3	Coincidence _3	Coincidence counter for top DDA3 HT and bottom LT per second

59	1	Sub Header	0x0E
60	3	Coincidence _4	Coincidence counter for top DDA3 LT and bottom HT per second
63	1	CRC	(sum of previous 63 Bytes)/0xFF

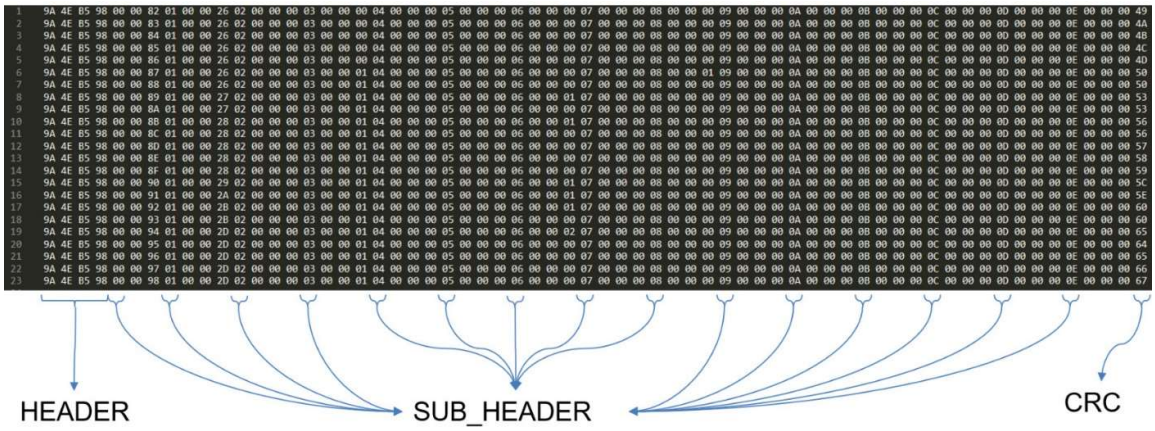


Figure 3.20 An example 64-byte long data packet from SB

The prototype was tested in METU-IVMER labs for 3 hours. DDA3 readout cards reach a temperature of ~60 ℃ after 30 mins of power-on time as shown in Figure 3.21. As the temperature of DDA3 increases the noise contribution to the particle counts in the top DDA3 detector until thermal equilibrium is reached. Most of the heat is generated by the op-amps because of their high gain. For the final design of YRM, use of an ASIC with low power consumption is necessary to prevent thermal issues in vacuum. During this test, a high energy cosmic particle shower was observed where both the top and bottom DDA3 detectors observed high particle counts in HT channels near the 3800th second of measurement. The coincidence HT-HT channel was also triggered on this shower.

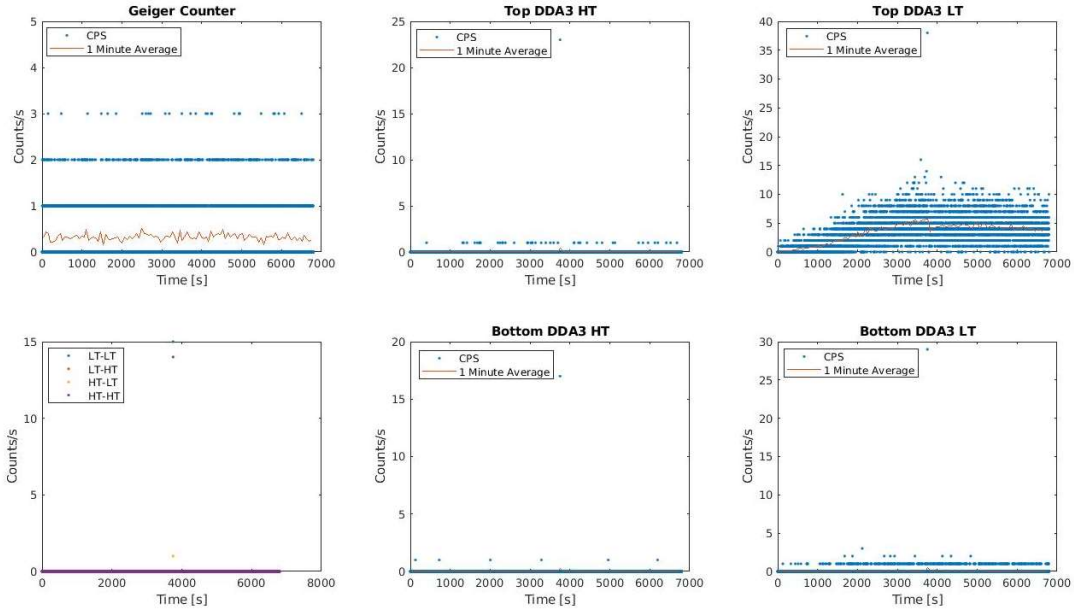


Figure 3.21 Test run of the YRM prototype in the IVMER lab showing data acquisition for 2 hours.

To test SB's sensitivity to different particles, the Geiger counter and DDA3 detectors were exposed to different radiation sources as summarized in Table 3.5 and

Table 3.6 respectively. SB.001 and SB.003 are flight modules while SB.002 was the module used for the environmental and flight-readiness tests. The tests were performed in the IVMER lab and the sources were held 1.0 cm away from the Geiger counter and 2.0 cm away from the DDA3 detectors. The sources used are listed below:

- 37 kBq Cs137 electron source
- 406 MBq Co57 gamma source
- 74 kBq Am241 alpha source (for Geiger counter)
- 3.7 kBq Am241 alpha source (for DDA3)

Table 3.5 Geiger counter count rates for using different sources and different SB modules.

SB serial number	Cs137 [cps]	Co57 [cps]	Am241 (secondaries) [cps]
SB.001 - Geiger	24	589	11
SB.002 - Geiger	29	685	7
SB.003 - Geiger	21	370	10

Table 3.6 DDA3 LT and HT count rates for using different sources and different modules.

SB serial number	Am241 [cps]	Cs137 [cps]
SB.001 – Top DDA3	LT: 109 HT: 109	LT: 2 HT: ~0
SB.001 – Bottom DDA3	LT: 92 HT: 92	LT: 0 HT: ~0
SB.002 – Top DDA3	LT: 106 HT: 106	LT: 1 HT: ~0
SB.002 – Alt DDA3	LT: 95 HT: 95	LT: 1 HT: ~0
SB.003 – Top DDA3	LT: 99 HT: 99	LT: 1 HT: ~ 0
SB.003 – Bottom DDA3	LT: 101 HT: 101	LT: 1 HT: ~0

SB also underwent a number of environmental tests, including: random vibration tests in 3-axes up-to 6.06 gRMS, shock tests in 3-axes for 11 ms at 30 g, pyro-separation tests, thermal vacuum tests from -10 ℃ to 50 ℃ for two cycles at $2.5x10^{-5}$ mbar, acceleration test at 20 g and a humidity test at 95% relative humidity from -10 ℃ to 30 ℃. SB passed all environmental tests without suffering physical

damage, loss of signal or signal packets, fatal logic errors or a change in the background level measurement of radiation.

3.7 Detector Testing in METU-DBL Facility

A DDA3 detector and its readout electronics were tested in the proton beam test facility of METU DBL [75, 48, 76]. 15 MeV and 30 MeV primary proton beams with fluxes ~10^8 p/cm^2/s exit the METU-DBL through a 50 μm titanium window and travel about 5 cm before they hit the target area. The detector readout card was housed in a shielded enclosure with aluminum plates and polyethylene blocks to shield the card against protons and secondary neutrons. The shielded enclosure had a straight aperture to fit the DDA3 detector such that the protons can pass to the sensitive area, and the aperture was sealed with 100μm aluminum foil to block light from reaching the DDA3 detector. The signal was readout using a Redpitaya^{TM} 125-14 card at a sampling rate of 125 MHz [77] and was sent via SCPI server to a computer running a script for analysis.

The pulse width of generated by the 15 and 30 MeV protons in the upper DDA3 detector was investigated and the results are shown in Figure 3.22. The energy deposition of 15 MeV and 30 MeV protons in the DDA3 detectors were found to be 3.7±0.4 and 1.9±0.1 MeV respectively using detailed Geant4 simulations which includes energy loss in the titanium and aluminum windows as well as air. Thus, the signal width of 15 MeV. The mean signal width for 15 MeV and 30 MeV is 4.2 and 10.0 samples respectively. These values are summarized in Table 3.7. The ratios between the mean signal width and mean energy deposition for 30 MeV and 15 MeV are slightly different but within error bars which shows the correlation between them. The signal width does not correspond linearly to the deposited energy. Rather, it depends mostly on the feedback capacitance in the trans-impedance amplification

stage and the RC constant of the readout electronics which plays a big role in determining the shape of the peak based on the current pulse through a non-linear relationship [78].

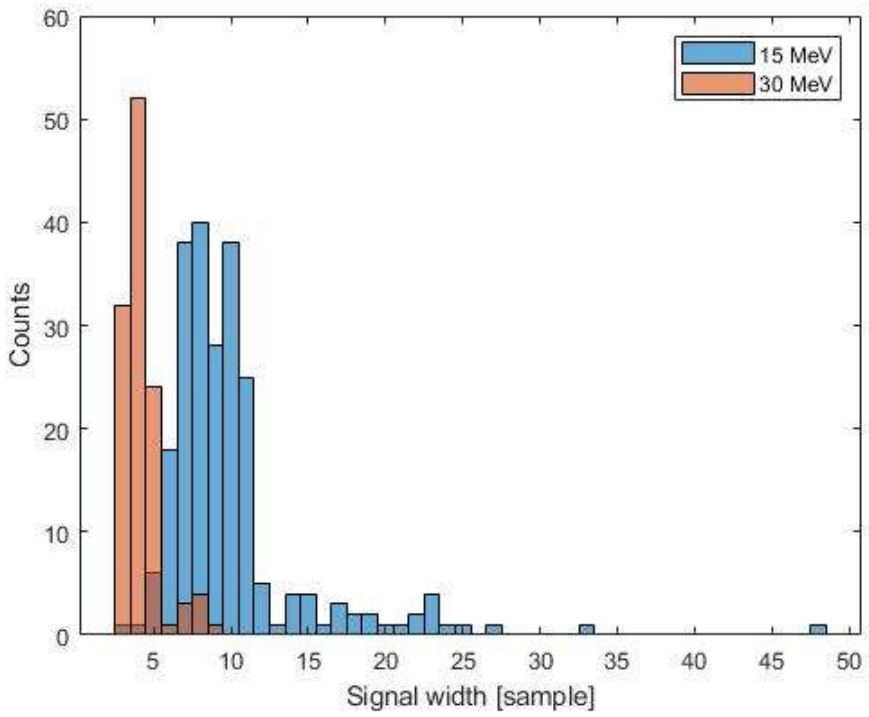


Figure 3.22 Histogram of signal width for the top DDA3 detector irradiated with 15 and 30 MeV protons at METU-DBL.

Table 3.7 Summary and comparison of the energy deposition values obtained via Geant4 and the measured signal width in METU-DBL

	15 MeV	30 MeV	Ratio
Mean Energy Deposition [MeV]	3.7±0.4	1.9±0.1	$1.95^{+0.33}_{-0.30}$
Mean Signal Width [Sample]	10.0±0.2	4.2±0.1	$2.38^{+0.11}_{-0.10}$

Another DDA3 and its readout electronics from the SB.002 box remained connected to the FPGA inside the SB enclosure and was positioned away from the main

irradiation area of the beam such that it is exposed to secondary particle irradiation. The upper Aluminum shielding of the SB enclosure was removed and replaced by 100μm aluminum foil to let as many secondaries through as possible without exposing the DDA3 detector to light. The results can be seen in Figure 3.23 in which the secondary flux changes depending on the beam position and its target material. This shows that this system has a wide dynamic range as a radiation monitor and can easily measure particle rates at 10^6 particles/s, which shows it can function in the SAA and the poles.

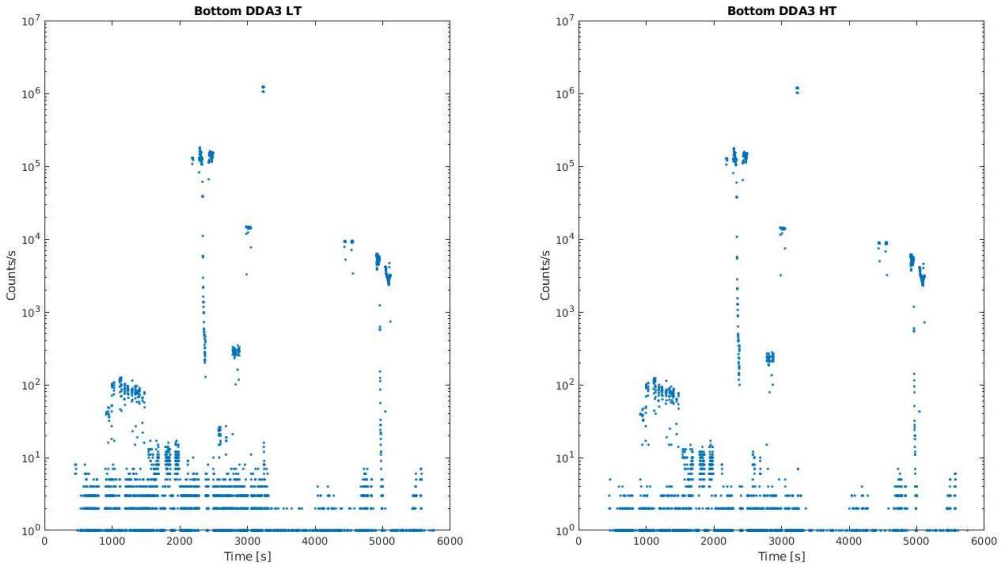


Figure 3.23 Background radiation monitoring using the bottom DDA3 from SB.002 box, during a 30MeV irradiation test in METU-DBL.

3.8 SB Flight and Data Analysis

SB.003 and SB.001 were flown on the SR 0.1 sounding rocket by ROKETSAN™ on 26th and 29th of October 2020 respectively. This rocket, which can reach an altitude of 136 km, consists of 2 stages and a fairing that opens up at an altitude of 80 km. A photograph of the rocket ready for lift-off on the launch pad is shown in Figure 3.24. SB is situated on top of the second stage of the rocket and is exposed to space directly when the fairing is opened.



Figure 3.24 Picture of the SR 0.1 rocket vertical on the launch pad in Sinop [80].

Results of SB.003 for the flight on October 26th are presented in for the Figure 3.26 ascent and Figure 3.27 for the descent. Both the dose rate from the Geiger counter and the count rate from the DDA3 is shown in 2.5 km wide bins. As discussed in Section 1.1.4, the Regener-Pfotzer maximum is observed when the rocket reaches ~20 km. The particle flux at ~80 km during the ascent shows a slight increase because the shielding conditions of the detectors changes at that altitude due to fairing separation as shown in Figure 3.25. These conditions persist throughout the descent as well.

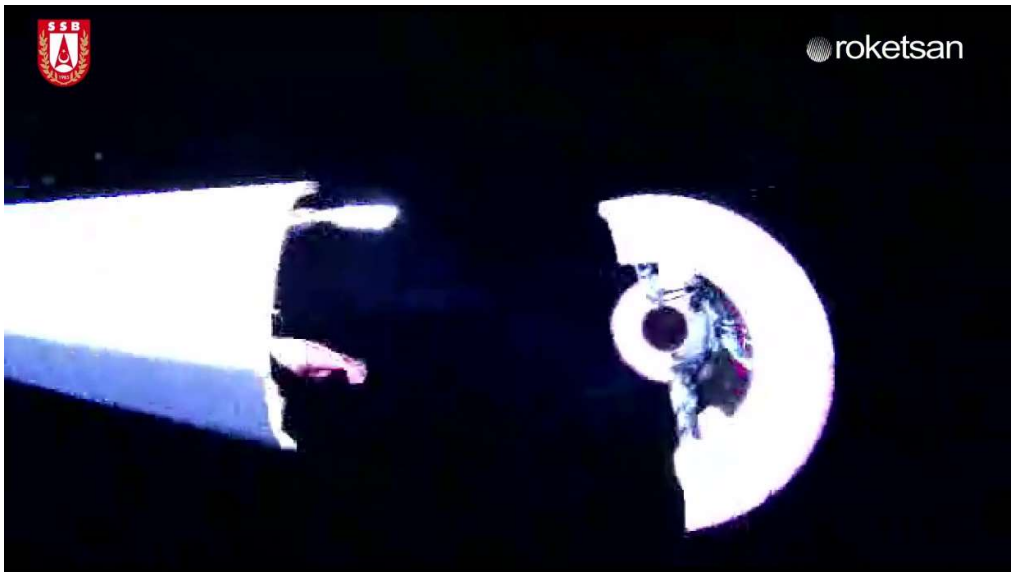


Figure 3.25 Picture of the fairing separation of the SR 0.1 rocket during flight [81].

After ~80 km, the top and bottom silicon detectors are sensitive to protons with energies E>13 MeV and E>21 MeV respectively. One pulse/s in the Geiger counter corresponds to 0.23 μGy/hour in dose rate. With this, the Regener-Pfotzer maximum dose rate was measured to be 2.07±0.02 μGy/hour and 2.24±0.03 μGy/hour for the first and second flights respectively, which is in agreement with the literature presented in Section 1.1.4.

During the flight, a HT-HT coincidence event was observed, at an altitude of ~120 km. This verifies the working principle of the proton telescope and that all flight equipment is capable of performing the measurement task in space. Due to the low statistics of the measurement, energy reconstruction algorithms could not be applied to the data for either flights. Data recorded at descent is smoother since the rocket is slower when free falling than when accelerating upwards, allowing for more data to be collected. In both flights, the Regener-Pfotzer maximum was observed at ~20 km.

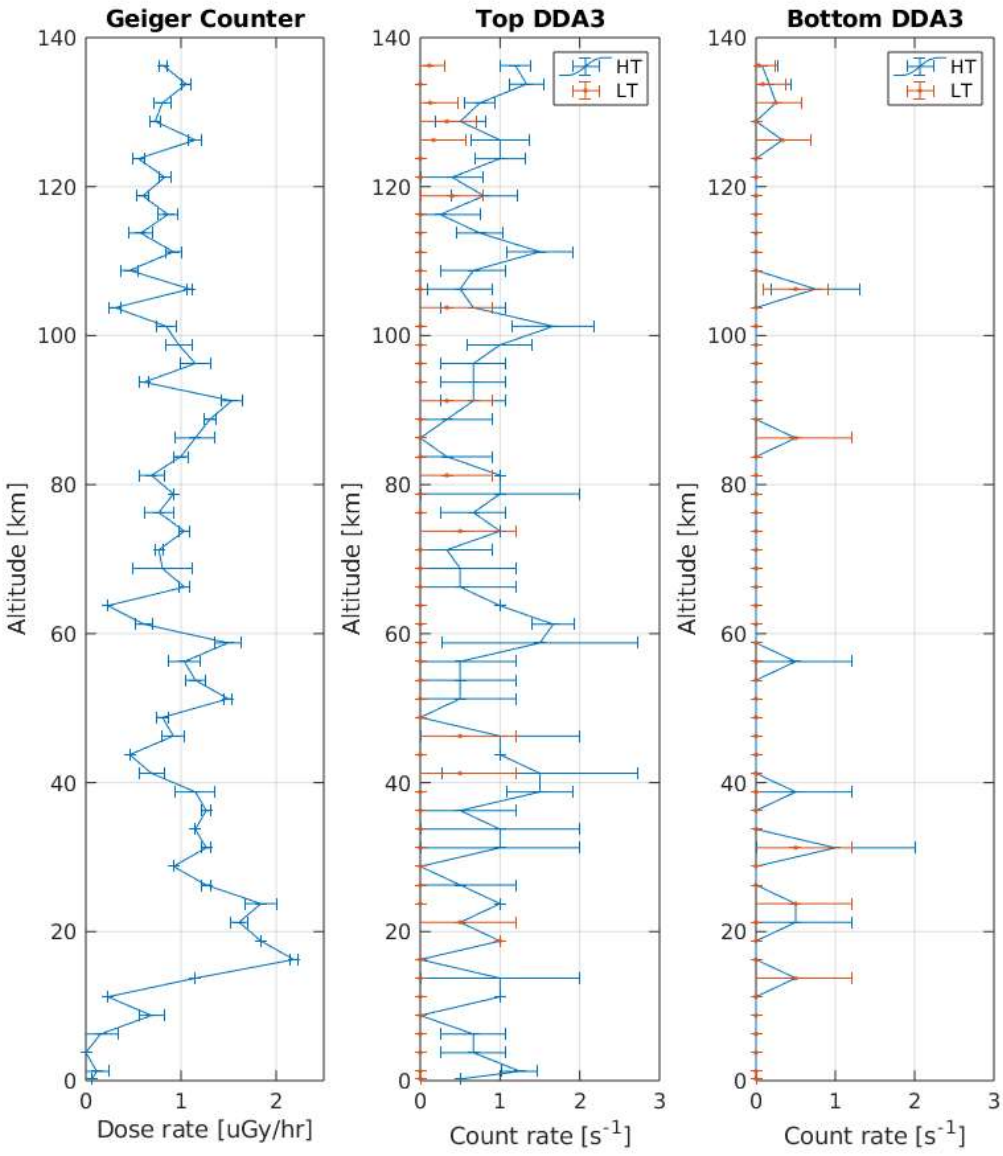


Figure 3.26 Data Collected from the first flight of SB.003 on the 26th during ascent.

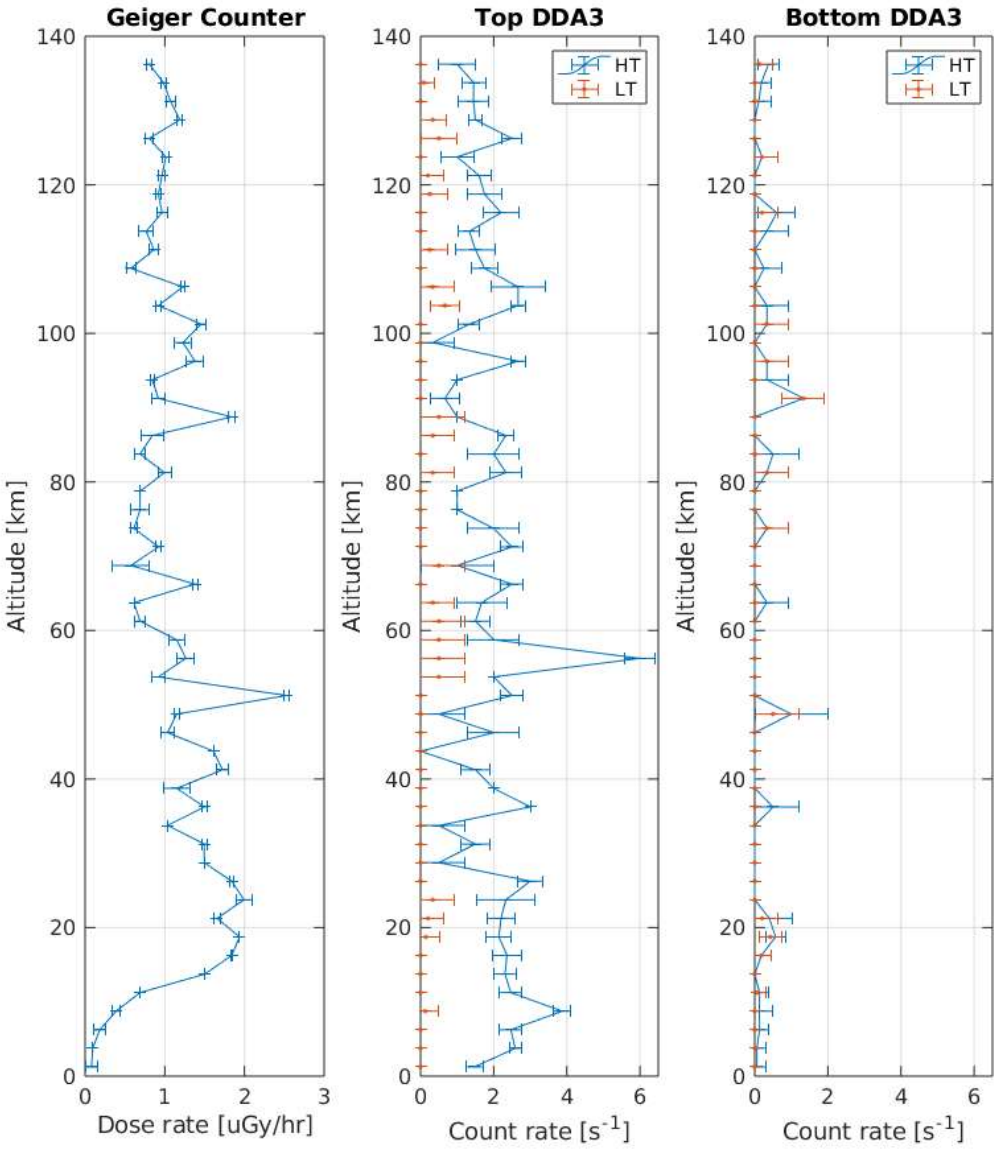


Figure 3.27 Data Collected from the first flight of SB.003 on the 26th during descent.

Because of partial data corruption due to EMI/EMC issues, the DDA3 data after fairing separation is corrupt for the 29th of October flight. Geiger dose rate data of the second flight is presented in Figure 3.28. The Regener-Pfotzer maximum dose rate was measured to be 2.24±0.03 μGy/hour which is 8.2% higher than the first flight. A total increase of 11.1% in the particle count distributed uniformly over the

flight altitude was also observed. This increase may be attributed to the coronal mass ejection that occurred at the 28th of October at ~20:00 UTC [82]. The count rate data obtained from the DDA3 detectors before fairing separation is presented in Figure 3.29. The Pfotzer-Regener maximum data from both flights are summarized in Table 3.8.

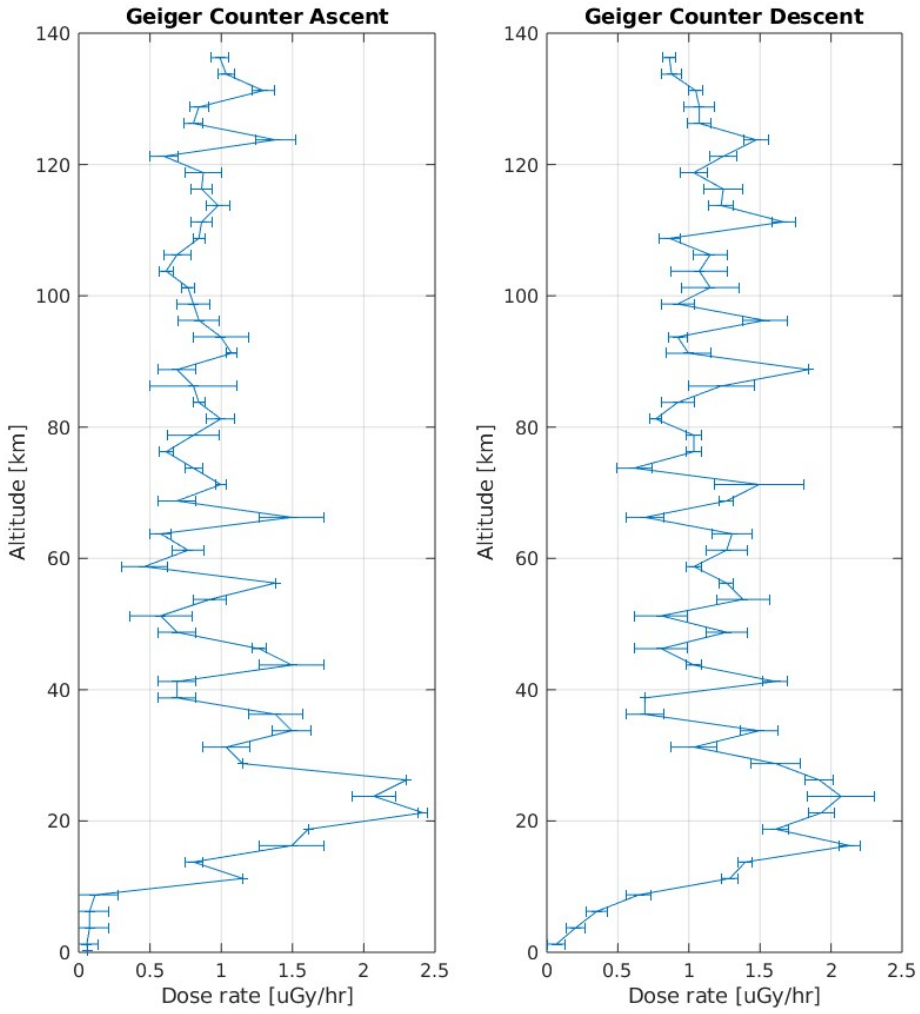


Figure 3.28 Geiger Counter measurement during the ascent and descent of the SR0.1 flight on the 29th of October.

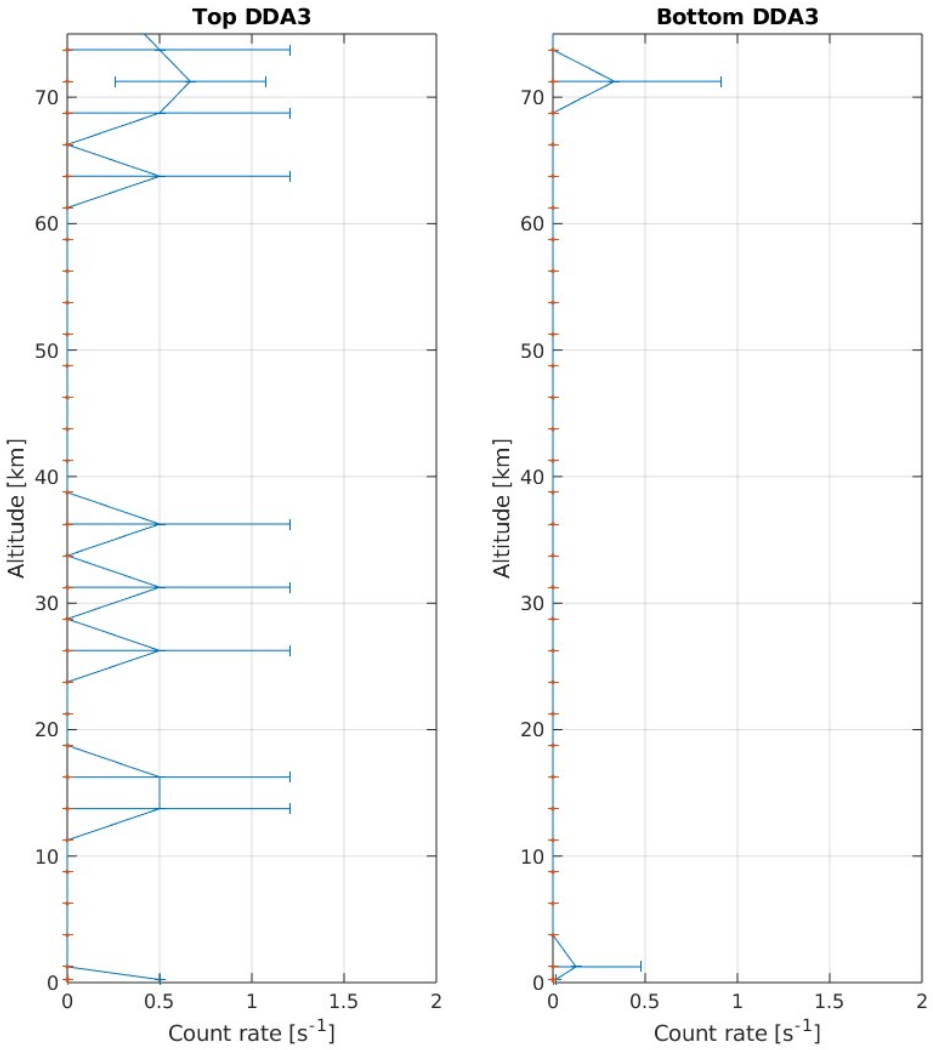


Figure 3.29 DDA3 measurement during the SR 0.1 flight on the 29th of October.

Table 3.8 Summary of flight data for first and second flights

	First Flight	Second Flight
Pfotzer-Regener maximum dose	2.07±0.02 μGy/hour	2.24±0.03 μGy/hour
Total flight particle count (Geiger)	1758 particles	1958 particles

The ~10% increase in the Geiger dose rate measurement can be attributed to a number of factors. The Total Electron Content (TEC) in the area of the rocket launch was analyzed and provided IONOLAB [83] using Receiver INdependent EXchange (RINEX) data provided by General Directorate of Mapping from the station near the launch location Sinop (**sinp**) and from four neighboring stations as shown in Figure 3.30. Comparison between the two launch dates show a similar increase of TEC as was observed by the Geiger counter.

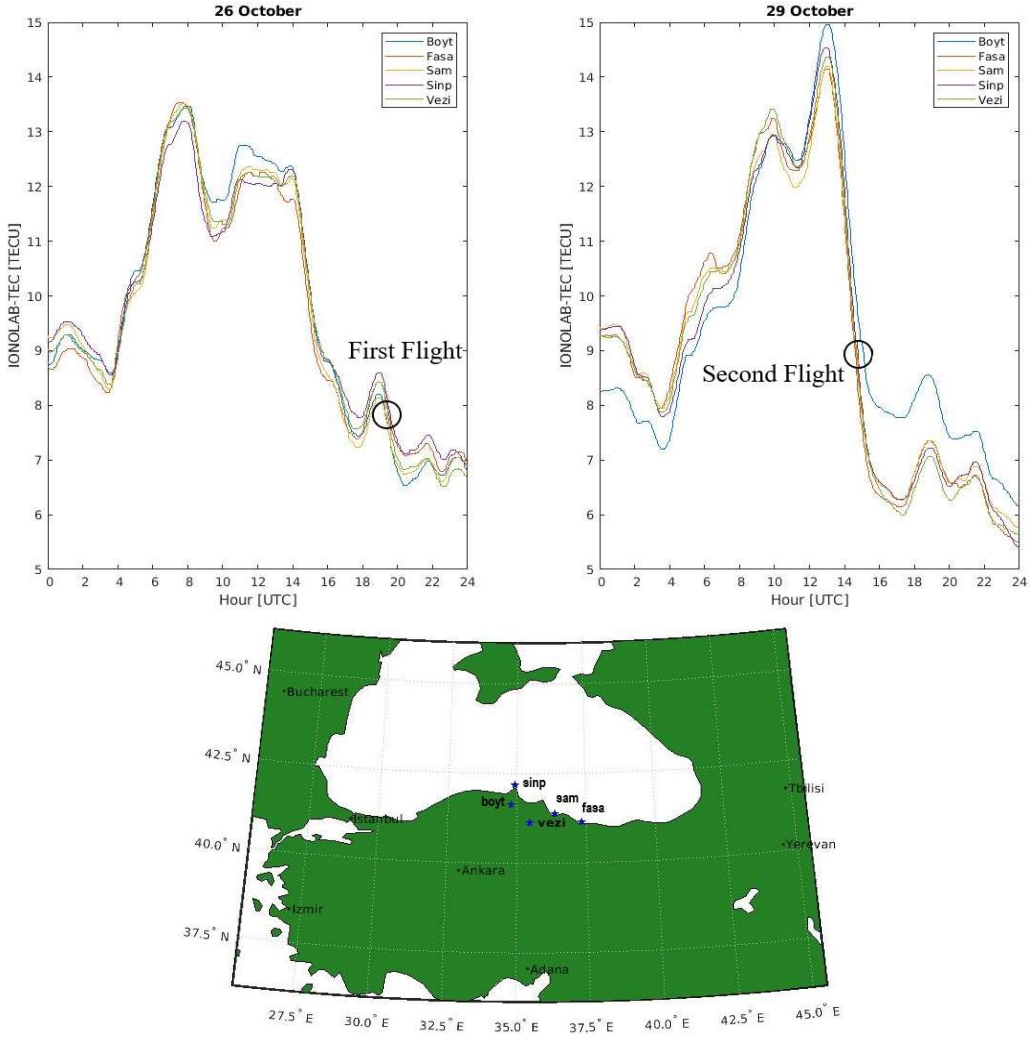


Figure 3.30 IONOLAB-TEC data provided by IONOLAB using the RINEX data provided by General Directorate of Mapping [83] from different TNPGN-Active stations on the launch dates. Locations of the stations are shown on the map.

In Figure 3.30, TEC estimated from dual-frequency GPS receivers are used as the data source. TEC values are obtained as IONOLAB-TEC. IONOLAB-TEC that is based on Regularized Estimation (Reg-Est) algorithm is one of the most robust, reliable and accurate algorithms in the literature for estimation of GPS-TEC over a single station in the local zenith directions detailed in [84, 85]. The phase-levelled TEC is estimated using a state-of-the-art signal processing technique as IONOLAB-STEC and IONOLAB-TEC for any high latitude, midlatitude or equatorial GPS station for both quiet and disturbed days of ionosphere [86]. The satellite positions (ephemeris) and IONospheric EXchange (IONEX) files that include the satellite Differential Code Biases (DCB), receiver DCBs for selected stations and Global Ionospheric Maps (GIM) are downloaded from [87]. The receiver DCBs that cannot be found in IONEX files are calculated using IONOLAB-BIAS algorithm given in [88]. IONOLAB-TEC is also available as an online space weather service at [89]. The current version of IONOLAB-TEC can be used online or can be downloaded from site as *.exe format [90]. In this study, IONOLAB-STEC values are estimated with 30 second resolution and IONOLAB-TEC values are obtained with 2.5 minute resolution [90, 91].

The IONOLAB-TEC estimates that are used in this study are computed from Turkish Permanent GPS Network (TNPGN-Active) which lies in midlatitude region of Northern Hemisphere between [E − E] and [N − N]. TNPGN-Active contains 146 stations and they provide continuous daily GPS measurements in Receiver INdependent EXchange (RINEX) format with 30 second resolution
The temporal resolution of TEC data that is used in this study is chosen to be 2.5 minutes.

This increase in the TEC values on the 29th of October can be attributed to a CME event that was observed by SOHO satellite as shown in Figure 3.31 [82]. This CME event was also detected by the 10.7cm radiometry at LASP [92] which also shows a ~10% increase between the first and the second launch dates as shown in Figure 3.32.

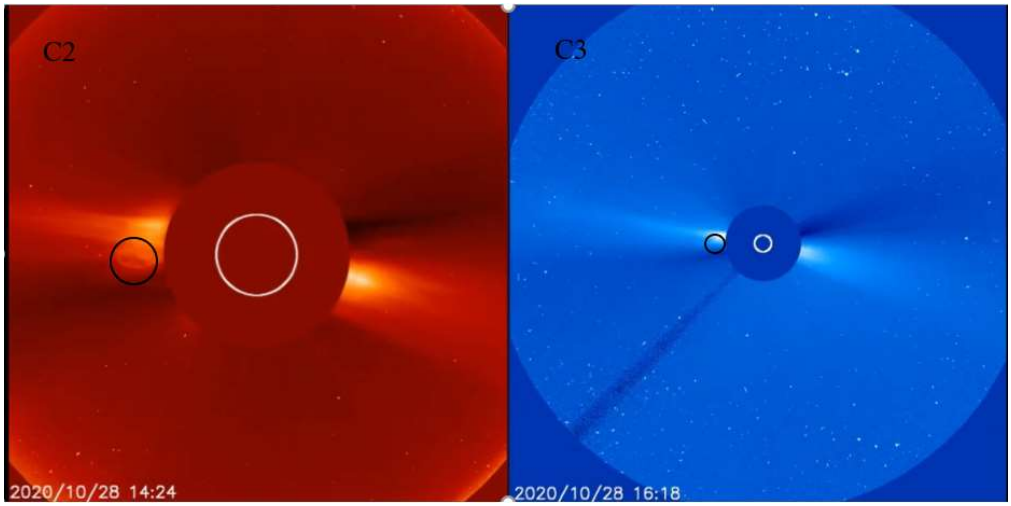


Figure 3.31 Picture from SOHO white light chronographs C2 (1.5 to 6 solar radii, Left) and C3 (3.7 to 30 solar radii, Right) [82].

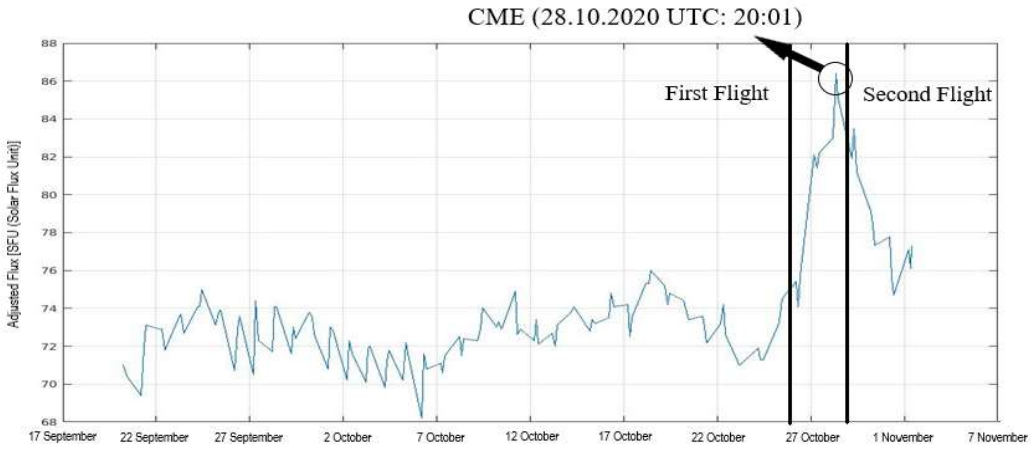


Figure 3.32 10.7cm radiometry data on the dates of the flights showing the CME on the 28th of October plotted with data obtained from [92].

The same increase cannot be discerned from neutron monitor data in Oulu [93], indicating that there was an increase in electron and gamma rays reaching the Earth without a significant increase in protons which in turn produces neutrons. This is consistent with the observation of low DDA3 counts in the second flight.

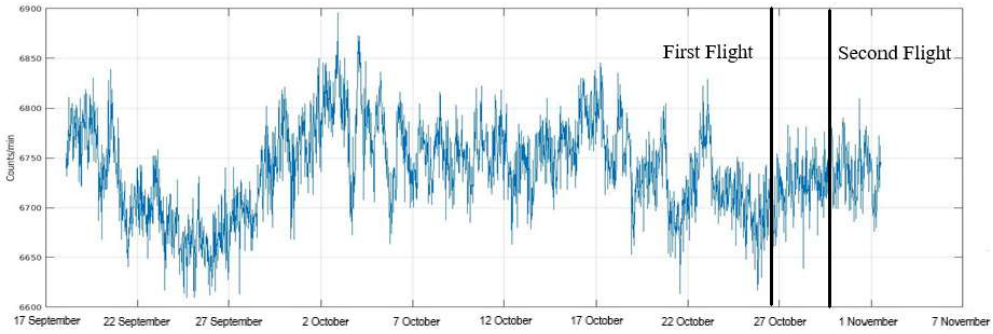


Figure 3.33 Neutron monitor data during the dates of the flight plotted using data from the Oulu neutron monitor [93].

3.9 Future Work

Efforts are underway to create a second prototype of YRM using the lessons learned from SB. Thermal performance and power usage of the readout electronics will be studied to be able to achieve the requirements for the final version of YRM. In parallel, work on the logic board of YRM and the manufacturing of the proton telescope is underway. Detector selection and circuit design for the electron telescope is also a work in progress with promising results. After the manufacturing of the telescopes is completed, they will be tested and calibrated in preparation for their eventual deployment.

CONCLUSION

In this thesis, the design of the proton telescope for YRM was presented. Different design alternatives were investigated through extensive simulations and the optimized designed was shown to achieve the design requirements for missions in LEO. In addition, the detectors that make up the proton telescope have been tested in space and shown to be suitable for the task by investigating their electronic properties and by designing a suitable readout circuit for them. The first prototype of YRM, called SB, was extensively tested against environmental factors and a lot of lessons were learned through that process. The quality of the readout and the logic design were tested through space flights and through irradiation tests in METU-DBL.

After completion of the upcoming tasks such as optimizing the electron telescope and its readout and testing the fully integrated YRM device and calibrating it, YRM is planned to be deployed on future space missions to LEO and beyond.

REFERENCES

[1] M. P. Petkov, "The Effects of Space Environments on Electronic Components," *NASA Technical Report,* p. 1–36, 2003.

[2] A.P.Trishchenkoa, L.D.Trichtchenkob and L.Garand, "Highly elliptical orbits for polar regions with reduced total ionizing dose," *Advances in Space Research,* pp. 3761-3767, 2019.

[3] J. W. Wilson, F. A. Cucinotta, J. L. Shinn, L. C. Simonsen, R. R. Dubey and W. R. Jordan, "Shielding from solar particle event exposures in deep space," *Radiation Measurements,* no. 361-382, 1999.

[4] R. Turner, "What We Must Know about Solar Particle Events to Reduce the Risk to Astronauts," *American Geophysical Union,* pp. 39-44, 2013.

[5] V. Fioretti, B. Andrea, G. Malaguti, V. Bianchin, M. Trifoglio and G. Fabiola., "The Low Earth Orbit radiation environment and its impact on the prompt background of hard X-ray focusing telescopes," *Proceedings of SPIE - The International Society for Optical Engineering,* p. 31, 2012.

[6] D. J. Hofmann and H. H. Sauer, "Magnetospheric Cosmic-Ray Cutoffs and their Variations," *Space Science Reviews,* pp. 750-803, 1968.

[7] Bento and E. R. Benton, "Space radiation dosimetry in low-earth orbit and beyon," *Nuclear Instruments and Methods in Physics Research Section B: Beam Interactions with Materials and Atoms,* pp. 255-294, 2001.

[8] G. Esposito, "Study of Cosmic Ray fluxes in Low Earth Orbit (LEO) observed with AMS experiment," *Thesis submitted to Universita Degli Di Perugia,* 2002.

[9] M. Walt, "Introduction to Geomagnetically Trapped Radiation," *Cambridge, UK: Cambridge,* 1994.

[10] N. Y. Ganushkina, I. Dandouras, Y. Y. Shprits and J. Cao, "Locations of boundaries of outer and inner radiation belts as observed by cluster and double star," *Journal o f Geophysical Research: Space Physics,* p. A09234, 2011.

[11] D. Heynderickx, J. Lemaire, E. J. Daly and H. D. R. Evans, "Calculating low-altitude trapped particle fluxes with the nasa models ap-8 and ae-8," *Radiation Measurements,* pp. 947-952, 1996.

[12] A. Gusev, G. Pugacheva, U. Jayanthi and S. N., "Modeling of Low-altitude Quasi-trapped Proton Fluxes at the Equatorial Inner Magnetosphere," *Brazilian Journal of Physics,* pp. 775-781, 2003.

[13] G. P. Ginet, T. P. O'Brien, S. L. Huston and et.al, "AE9 AP9 and spm: New models for specifying the trapped energetic particle and space plasma environment," *Space Science Reviews,* pp. 579-6015, 2013.

[14] C. E. Jordan, "Nasa radiation belt models AP-8 and AE-8," *DTIC Documen,* 1989.

[15] ESA, "Space environment information system," *[Online] Available: https://www.spenvis.oma.be,* 2015.

[16] P. Kristof, "Solar cycle prediction," *Living Reviews in Solar Physics,* 2010.

[17] L. I. Miroshnichenko and R. A. Nymmikb, "Extreme fluxes in solar energetic particle events: Methodological and physical limitations," *Radiation Measurements,* vol. 61, pp. 6-15, 2014.

[18] B. L. Peter, "Galactic cosmic rays," *Journal o f Physics: Conference Series,* p. 78, 2006.

[19] M. Aguilar and et.al, "Properties of Cosmic Helium Isotopes Measured by the Alpha Magnetic Spectrometer," *Phys. Rev. Lett. 123,* p. 181102, 2019.

[20] M. Aguilar and et.al, "Towards Understanding the Origin of Cosmic-Ray Electrons," *American Physical Society Phys. Rev. Lett. 122,* p. 101101, 2019.

[21] A. J. Tylka, J. H. Adams, P. R. Boberg, B. Brownstein, W. F. Dietrich, E. O. Flueckiger and et.al, "Creme96: A revision of the cosmic ray effects on micro-electronics code," *IEEE Transactions on Nuclear Science,* pp. 2150-2160, 1997.

[22] T. Sato, "Analytical Model for Estimating Terrestrial Cosmic Ray Fluxes Nearly Anytime and Anywhere in the World: Extension of PARMA/EXPACS," *PLOS,* 2015.

[23] R. Engel, "Air Showers and Hadronic Interactions," Karlsruhe Institute of Technology, 2012.

[24] T. Dachev, "Profile of the ionizing radiation exposure between the Earth surface and Free Space," *Journal of Atmospheric and Solar-Terrestrial Physics,* pp. 148-156, 2013.

[25] M. Barrantes and et.al, "Atmospheric corrections of the cosmic ray fluxes detected by the Solar Neutron Telescope at the Summit of the Sierra Negra Volcano in Mexico," *Geofísica internacional,* pp. 253-275, 2018.

[26] K. Copeland, "CARI-7A: Development and Validation," *Radiation Protection Dosimetry ,* pp. 1-13, 2017.

[27] Y. Stozhkov, N. Svirzhevsky and V. Makhmutov, "Cosmic Ray Measurements In The Atmosphere," *CERN,* 2001.

[28] R.G.Harrison, K.A.Nicol and K.L.Aplin, "Vertical profile measurements of lower troposphere ionisation," pp. 203-210, 2014.

[29] W. Mark and et.al, "PR3: A system For radio-interferometry and radiation measurement on sounding rockets," *Microprocessors and Microsystems,* vol. 77, 2020.

[30] A. M. Galper and et.al, "The PAMELA experiment: a decade of Cosmic RayPhysics in space," *Journal of Physics: Conference Series,* no. 798, 2017.

[31] W. B. Atwood, A.A.Abdo and et.al, "The Large Area Telescope on the Fermi Gamma-Ray Space Telescope Mission," *The Astrophysical Journal,* p. 1071–1102, 2009.

[32] J. F. Fennell, S. G. Claudepierre, J. B. Blake1, T. P. O'Brien, J. H. Clemmons and D. N. Baker:, "Van Allen Probes show that the inner radiation zone contains no MeV electrons," *Geophysical Research Letters,* pp. 1283-1289, 2015.

[33] R. H. Maurer, J. O. Goldsten, P. N. Peplowski, A. G. Holmes-Siedle and M. H. Butler, "Early Results From the Engineering Radiation Monitor (ERM) and Solar Cell Monitor on the Van Allen Probes Mission," *IEEE Transactions on Nuclear Science,* pp. 4053 - 4058, 2013.

[34] D. M. Hassler, W. D. Deininger, N. Nickles and B. Unruh, "Space Environment Monitoring Suite (SEMS) for Near-Earth Environment Characterization During SEP Ops," *2014 IEEE Aerospace Conference,* 2014.

[35] C. Mathias and et.al, "The Energetic Particle Telescope (EPT) on Board PROBA-V: Description of a New Science-Class Instrument for Particle Detection in Space," *IEEE Transactions on Nuclear Science,* pp. 3667-3681, 2014.

[36] C. Underwood, B. Taylor, A. Dyer, A. Hands, K. Ryden, W. Avison and D. Bambe, "Development of Miniaturised Radiation Environment Monitors for Commercial Spaceflight: Flight Results from the MuREM/RM Payloads," *IEEE,* 2016.

[37] S. Gohl, B. Bergmann and et.al, "Study of the radiation fields in LEO with the Space Application of Timepix Radiation Monitor (SATRAM)," *Advances in Space Research,* pp. 1646-1660, 2019.

[38] EFACEC, "EFACEC Space Radiation Monitors MFS & Berm," *Space Radiation and Plasma Environment Workshop,* 2014.

[39] J. Saunders, *J. Phys. C 2,* p. 2181, 1969.

[40] A. Affolder and et.al, "Silicon detectors for the sLHC," *Nuclear Instruments and Methods in Physics,* pp. 11-16, 2011.

[41] C. Kittel, Introduction to Solid State Physics, New York: John Wiley, 1986.

[42] T. Ceponis, A. Balcytis and A.Dzimidavicius, "Dependence of Silicon PIN Diode Electrical Charecteristics on Proton Fluence," *Lithuanian Journal of Physics,* pp. 215-223, 2010.

[43] D. Griffiths, Introduction to Elementary Particles, 1987.

[44] W. Leo, "Techniques for Nuclear and Particle Physics Experiments: A How-To Approach," *Springer Science & Business Media,* pp. 24-25, 2012.

[45] T. Tessonnier, A. Mairani, S. Brons, T. Haberer, J. Debus and K. Parodi, "Experimental dosimetric comparison of 1H, 4He, 12C and 16O scanned ion beams," *PhysMed BioT.,* pp. 62-72, 2017.

[46] "Detector Physics," [Online]. Available: https://indico.mitp.uni-mainz.de/event/65/attachments/1698/1781/Kuehn.pdf. [Accessed May 2020].

[47] Xapsos, S. Bourdarie and M., "The Near-earth Space Radiation Environment," *IEEE transactions on nuclear science,* pp. 1810-1832, 2008.

[48] B. Demirköz and et.al, "METU Defocusing BeamLine Project for the First SEE Tests in Turkey and the Test Results From the METU-DBL Preliminary Setup," *Nucl Instr. Meth. Phys. Res. A: Accelerators, Spectrometers, Detectors and As-sociated Equipment,* pp. 10-12, 2018.

[49] L. Maria Martinez, "Analysis of LEO Radiation Environment and Its Effects on Spacecraft's Critical Electronic Devices," *Thesis submitted to Embry Riddle Aeronautical University,* 2011.

[50] NOAA, "As Good As Gold: Are Satellites Covered in Gold Foil?," (Retrived from : "https://www.nesdis.noaa.gov/content/good-gold-are-satellites-covered-gold-foil"), 2016.

[51] S. Samwel and et.al, "Studying the Total Ionizing Dose and Displacement Dam-age Dose Effects for Various Orbital Trajectories," *First Middle East-Africa Re-gional IAU Meeting,* p. 12, 2008.

[52] M. Boscherini and et.al, "Radiation Damage of Electronic Components in Space Environment," *Nucl. Instr. Meth. Phys. Res. A: Accelerators, Spectrometers, Detectors and Associated Equipment,* pp. 112-116, 2003.

[53] J. M. Maclaren and T.Majni, "Hard/Soft Error Detection," *USPatent 6,711,703,* 2004.

[54] E. Petersen, "Single Event Effects in Aerospace," *IEEE Press,* 2011.

[55] R. Gaillard, "Single Event Effects: Mechanisms and Classification,"Soft Errorsin Modern Electronic Systems"," *Springer,* pp. 27-54, 2011.

[56] P. Uslu, "Radiation Damage Studies Of Bulk Metallic Glass Materials under Proton Irradiation And Radioprotection Studies For METU-DBL," *Thesis Submitted to METU,* 2019.

[57] J. Srour, C. Marshall and P. Marshall, "Review of Displacement Damage Effects in Silicon Devices," *IEEE Transactions on Nuclear Science,* pp. 653-670, 2003.

[58] CERN, "Geant4 User's Guide for Application Developers," 2016.

[59] "Analytical derivation of the geometric factor of a particle detector having circular or rectangular geometry," *J. Phys. E: Sci. Instrum. ,* pp. 260-263, 1972.

[60] S. Pak, Y. Shin, J. Woo and J. Seon, "A Numerical Method To Analyze Geometric Factors of A Space Particle Detector Relative To Omnidirectional Proton And Electron Fluxes," *Journal of the Korean Astronomical Society,* pp. 111-117, 2018.

[61] M. Novak, "Geant4 Advanced Course : Electromagnetic physics II," *Retreived from Presentation,* 2019.

[62] CERN, "GDML User's Guide".

[63] P. G. Marco Pinto, "GUIMesh: a tool to import STEP geometries into Geant4 via GDML," *arXiv:1807.04319,* 2018.

[64] M. Lawrence., "High-Performing Simulations of The Space Radiation Environment For The International Space Station and Apollo Missions," *Thesis submitted to The University of Utah,* 2016.

[65] S. Kuznetsov and I. Myagkova, "Energetic Trapped Proton and Electron Flux Variations at Low Altitudes Measured Onboard <<CORONAS-I>> Satellite, Their Connection With The Particle Flux Variations in Geotationary Orbit," *Adv. Space Res.,* pp. 2319-2323, 2002.

[66] S. Srivastava, R. Henry and A. T. R, "Characterization Of Pin Diode Silicon Radiation Detector," *Journal on Intelligent Electronic Systems,* pp. 47-51, 2007.

[67] D. K. Schroder, Semiconductor Material And Device Characterization, Tempe, AZ: WILEY, 2006.

[68] S. M. Sze, Semiconductor Devices: Physics and Technology, 1985.

[69] J.M. Park, K.S. Park and et.al, "Consideration of the Leakage-Current and the Radiation-Response Characteristics of Silicon PIN Detectors with Different N-Type Substrates and their Application to a Personal γ-ray Dosimeter," *Journal of the Korean Physical Society,* pp. 10-17, 2007.

[70] "(Personal Comunication , Dr. Aziz Ulvi Çalışkan)," 2020.

[71] ROKESTSAN, "Türk Roketi İlk Kez Sıvı Yakıtla Uzayda," *(Retrived from : "https:// www.roketsan.com.tr/turk-roketi-ilk-kez-sivi-yakitla-uzayda/"),* 2020.

[72] J. F. Ziegler, M. D. Ziegler and J. P. Biersack, "SRIM - The stopping and range of ions in matter," *Nuclear Instruments and Methods in Physics Research Section B,* pp. 1818-1823, 2010.

[73] Microsemi, "DS0128: IGLOO2 and SmartFusion2 Datasheet," *(Retrived From "https:/ /www.microsemi.com/product-directory/fpgas/1688-igloo2#documentation"),* 2018.

[74] B. Trump, "Taming the Oscillating Op Amp," *Texas Instruments Documentation (Retrieved from https://e2e.ti.com/blogs_/archives/b/thesignal/archive/2012/05/30/ taming-the-oscillating-op-amp),* 2012.

[75] B. Demirkoz, A. Avaroglu and et.al, "The First SEE Test Campaign in Turkey at the METU Defocusing Beamline Preliminary Setup," pp. 1-4, 2017.

[76] M. B. Demirkoz and et.al, "METU-Defocusing Beamline : A 15-30 Mev Proton Irradiation Facility and Beam Measurement System," *EPJ Web of Conferences,* vol. 225, 2020.

[77] Redpitaya, "Red Pitaya Documentation Release 0.97," *Retrived from "https:// redpitaya.readthedocs.io/_/downloads/en/latest/pdf/",* 2020.

[78] Z. Bielecki, "Readout electronics for optical detectors," *Opto-Electronics Review,* pp. 129-137, 2004.

[79] S. Meroli, "Matlab function to compute and display a Landau Distribution Fit," [Online]. Available: https://meroli.web.cern.ch/Lecture_landau_ionizing_particle. html. [Accessed 2021].

[80] ROKETSAN, "Sounding Rocket 0.1 Flight Tests," (Retrieved From : "https://www.youtube.com/watch?v=ejhdoTiEL5E&ab_channel=RoketsanA.%C5%9E.",t=1:42), 2020.

[81] Roketsan, "Sounding Rocket 0.1 Flight Tests," (Retrieved from : "https://www.youtube.com/watch?v=ejhdoTiEL5E&ab_channel=RoketsanA.%C5%9E." , t=0:42), 2020.

[82] NASA, "Solar and Heliosphereic Observatory," NASA, 2020. [Online]. Available: https://sohowww.nascom.nasa.gov/home.html. [Accessed 15 November 2020].

[83] "(Personal Communication,Prof. Dr. Feza Arıkan)," http://www.ionolab.org/, 2020.

[84] F. Arikan, C. Erol. and O. Arikan, "Regularized estimation of vertical total electron content from Global Positioning System data," *Journal of Geophysical Research-Space Physics,* pp. 1469-1480, 2003.

[85] F. Arikan, C. Erol and O. Arikan, "Regularized estimation of vertical total electron content from GPS data for a desired time period," *Radio Science,* pp. 1-10, 2004.

[86] H. Nayir, F. Arikan, O. Arikan, C. Erol. and et.al, "Total electron content estimation with Reg-Est," *Journal of Geophysical Research-Space Physics,* pp. 1-11, 2007.

[87] NASA, "Nasa's Archive of Spcace Geodesy Data," 2020. [Online]. Available: ftp://cddis.gsfc.nasa.gov/gps/products/ionex/.

[88] F. Arikan, H. Nayir, U. Sezen and O. Arikan., "Estimation of single station interfrequency receiver bias using GPS-TEC," *Radio Science,* pp. 1-13, 2008.

[89] U. Sezen, F. Arikan., O. Arikan. and et.al, "near-real time estimation of GPS-TEC: IONOLAB-TEC. Space Weather," *297-305,* pp. 297-305, 2013.

[90] F. Arikan, U. Sezen, C. Toker and et.al, "Space weather studies of IONOLAB group," *2016 URSI Asia-Pacific Radio Science Conference (URSI AP-RASC),* pp. 1136-1139, 2016.

[91] F. Arikan, C. Erol and O. Arikan, "Regularized estimation of TEC from GPS data for certain mid-latitude stations and comparison with the IRI model," *Advances in Space Research,* pp. 867-874, 2007.

[92] University of Colorado Laboratory for Atmospheric and Space Physics, "LISRID (LASP Interacrive Solar IRadiance Datacenter)," University of Colorado, 2020. [Online]. Available: https://lasp.colorado.edu/lisird/data/noaa_radio_flux/. [Accessed 15 November 2020].

[93] University of Oulu, "Oulu Neutron Monitor Data," 2020. [Online]. Available: https://cosmicrays.oulu.fi/. [Accessed 15 November 2020].